Majorana bound states in topological Josephson junctions

De Almeida Nascimento e Melo, A.A.

DOI
10.4233/uuid:6068f129-9d99-4b39-92f7-681455ae4ab4

Publication date
2023

Document Version
Final published version

Citation (APA)
De Almeida Nascimento e Melo, A. A. (2023). *Majorana bound states in topological Josephson junctions*. [Dissertation (TU Delft), Delft University of Technology]. https://doi.org/10.4233/uuid:6068f129-9d99-4b39-92f7-681455ae4ab4

MAJORANA BOUND STATES IN TOPOLOGICAL JOSEPHSON JUNCTIONS

MAJORANA BOUND STATES IN TOPOLOGICAL JOSEPHSON JUNCTIONS

Dissertation

for the purpose of obtaining the degree of doctor
at Delft University of Technology
by the authority of the Rector Magnificus prof. dr. ir. T.H.J.J. van der Hagen,
chair of the Board for Doctorates,
to be defended publicly on
Thursday, 12 January 2023 at 12:30 o'clock

by

André Alexandre DE ALMEIDA NASCIMENTO E MELO

Master of Science in Applied Physics, Delft University of Technology, the Netherlands
born in Castelo Branco, Portugal

This dissertation has been approved by the

promotor: Dr. A. R. Akhmerov
copromotor: Dr. M. T. Wimmer

Composition of the doctoral committee:

Rector Magnificus,	chairperson
Dr. A. R. Akhmerov	AS, promotor
Dr. M. T. Wimmer	AS, copromotor
Independent members:	
Dr. E. P. L. van Nieuwenburg	Leiden U., NL
Prof.dr. M. Leijnse	Lund U., Sweden
Prof.dr. V. Fatemi	Cornell U., USA
Prof.dr. A. F. Otte	AS
Prof.dr. Y. M. Blanter	AS, reserve member

This work was supported by the Netherlands Organization for Scientific Research (NWO/OCW) as part of an NWO VIDI grant 016.Vidi.189.180.

Printed by: Print&Bind

Front & Back: *Impression, Sunrise* by Claude Monet (1872)

Casimir PhD Series, Delft-Leiden 2023-01

ISBN 978-94-6366-641-1

An electronic version of this dissertation is available at
`http://repository.tudelft.nl/`.

To my parents.

CONTENTS

SUMMARY

Much of modern mesoscopic physics focuses on studying hybrid superconducting structures: systems that combine superconductors with other materials such as semiconductors, ferromagnets, and graphene. When properly engineered, these devices display emergent physical properties that are absent in their individual constituents. An early example of such a device is the two-terminal Josephson junction: two superconducting terminals connected by a region without superconductivity. Josephson junctions give rise to a plethora of interesting phenomena, including quantized voltage steps and macroscopic quantum coherence. Experimental and theoretical advances in Josephson devices have led to numerous technological applications, such as sensitive magnetic field detectors, rapid single flux quantum logic, metrological voltage standards, and superconducting qubits.

Semiconductors with strong spin-orbit coupling proximitized with a superconductor are another prominent example of hybrid devices. Although semiconductors and conventional superconductors have been well understood for decades, their combination is predicted to yield a new state of matter known as topological superconductivity. Topological superconductors host Majorana bound states: topologically protected quasiparticles with non-abelian statistics that are promising candidates to realize fault-tolerant qubits. Reliably creating and manipulating Majorana modes remains one of the outstanding challenges in modern condensed matter physics.

In the first two chapters of this thesis, we theoretically study Majorana bound states in Josephson junctions formed in a two-dimensional electron gas. The primary advantage of this setup is that it removes one of the major obstacles in nanowire-based platforms, namely the need to apply a large external magnetic field to break time-reversal symmetry and drive a topological phase transition. Specifically, applying a superconducting phase difference across the junction significantly lowers the magnetic field required to create Majoranas.

In Ch. 2 we introduce a modified Majorana junction setup that removes the need for an external magnetic field altogether. To achieve this, we propose breaking time-reversal symmetry by applying supercurrents parallel to the junction. We show that, combined with spin-orbit coupling, the supercurrents create an effective Zeeman field that lifts Kramers' degeneracy. However, without additional modifications, this system has a conservation law that prevents the opening of a topological gap. We present three schemes that break this conservation law and stabilize a topological phase: adding a third superconductor, introducing a periodic potential, or making the junction zigzag-shaped.

While Majorana junctions are a promising platform to realize topological superconductivity, they are often plagued by small topological gaps. Semiclassically, this occurs due to states with high momentum parallel to the junction that have long flight times and thus result in a small induced gap. Earlier work showed that removing long quasiparticle trajectories by making the junction zigzag-shaped results in an order of magnitude increase in the topological gap. A natural follow-up question is how to find the geometry that maximizes the topological gap. In Ch. 3, we tackle this problem by developing an optimization algorithm that explores the space of junction geometries greedily. We show that the algorithm is capable of finding high-gap geometries in a variety of physical settings. Additionally, we provide evidence that the algorithm likely converges to global maxima in geometry space.

In Ch. 4, we turn our attention to (non)local transport experiments in hybrid superconducting devices, a commonly-used method to measure the density of states in Majorana devices. Linear response theory predicts that the conductance matrix of such devices obeys various symmetry relations. As an example, the two-terminal conductance is predicted to be symmetric in voltage, a manifestation of particle-hole symmetry. However, experimental conductance maps of Majorana devices often show significant deviations from these symmetries. One possible explanation is the presence of quasiparticle poisoning, which hinders Majorana qubits. We show that a bias-dependent tunnel barrier also leads to the breakdown of symmetries of the conductance matrix. Crucially, this mechanism preserves superconducting parity and therefore is benign for Majorana qubits. We conclude by identifying several physical behaviors that distinguish symmetry breaking originating from a voltage-dependent tunnel barrier and dissipation.

Finally, in Ch. 5 we explore a different topic in mesoscopic physics: multiplet supercurrent in multiterminal Josephson junctions. Previously proposed mechanisms to observe multiplets rely on delicate nonlocal Andreev processes that are obscured by dissipation. We show that this effect also arises in commonplace Josephson tunneling circuits with only local Cooper pair transfers. Remarkably, the multiplet supercurrent persists even when the circuit is in the deep charging regime where only single Cooper pairs are allowed to tunnel in and out of the central island.

SAMENVATTING

Een groot deel van de moderne mesoscopische fysica richt zich op de studie van hybride supergeleidende structuren: systemen die supergeleiders combineren met andere materialen zoals halfgeleiders, ferromagneten en grafeen. Wanneer deze systemen op de juiste manier zijn ontworpen, vertonen ze nieuwe fysische eigenschappen die in hun afzonderlijke onderdelen ontbreken. Een vroeg voorbeeld van zo'n apparaat is de Josephson-junctie met twee terminals: twee supergeleidende terminals verbonden door een gebied zonder supergeleiding. In Josephson-juncties komen een groot aantal interessante verschijnselen voor, waaronder gekwantificeerde spanningsstappen en macroscopische kwantumcoherentie. Experimentele en theoretische vooruitgang in Josephson-apparaten heeft geleid tot talrijke technologische toepassingen, zoals gevoelige detectoren van magnetische velden, snelle kwantumlogica met een flux, metrologische spanningsstandaarden en supergeleidende qubits.

Halfgeleiders met een sterke spin-baankoppeling nabij een supergeleider zijn een ander prominent voorbeeld van hybride apparaten. Hoewel halfgeleiders en conventionele supergeleiders al tientallen jaren goed worden begrepen, wordt voorspeld dat hun combinatie een nieuwe toestand van materie zal opleveren die bekend staat als topologische supergeleiding. Topologische supergeleiders herbergen Majorana-gebonden toestanden: topologisch beschermde quasideeltjes met niet-abeliaanse statistieken die veelbelovende kandidaten zijn om fouttolerante qubits te realiseren. Het betrouwbaar creëren en manipuleren van Majorana toestanden blijft een van de uitdagingen in de moderne gecondenseerde materie fysica.

In de eerste twee hoofdstukken van dit proefschrift bestuderen we theoretisch Majorana gebonden toestanden in Josephson juncties gevormd in een tweedimensionaal elektronengas. Het belangrijkste voordeel van deze opstelling is dat zij een van de belangrijkste obstakels van op nanodraad-gebaseerde platforms wegneemt, namelijk de noodzaak om een groot extern magnetisch veld toe te passen om tijdspariteit te doorbreken en een topologische faseovergang aan te sturen. Met name het toepassen van een supergeleidend faseverschil over de junctie verlaagt het magneetveld dat nodig is om Majorana's te creëren aanzienlijk.

In hoofdstuk 2 introduceren we een aangepaste Majorana-junctie die de noodzaak van een extern magnetisch veld volledig wegneemt. Om dit te bereiken stellen wij voor de tijdspariteit te doorbreken door superstromen parallel aan de junctie aan te leggen. Wij laten zien dat, in combinatie met spin-baankoppeling, de supergeleidende stromen een effectief Zeemanveld creëren dat de ontaarding van Kramers opheft. Zonder extra aanpassingen heeft dit systeem echter een behoudswet die het openen van een topologische kloof verhindert. Wij presenteren drie regelingen die deze behoudswet doorbreken en een topologische fase stabiliseren: toevoeging van een derde supergeleider, invoering van een periodieke potentiaal, of het zigzagvormig maken van de junctie.

Hoewel Majorana juncties een veelbelovend platform zijn om topologische supergeleiding te realiseren, worden ze vaak geplaagd door kleine topologische bandkloven. Semiklassiek ontstaat dit door toestanden met een hoog momentum parallel aan de junctie die lange reistijden hebben en dus resulteren in een kleine geïnduceerde kloof. Eerder werk toonde aan dat het verwijderen van lange trajecten van quasideeltjes door de verbinding zigzagvormig te maken, resulteert in een orde van grootte toename van de topologische kloof. Een natuurlijke vervolgvraag is hoe de geometrie te vinden die de topologische kloof maximaliseert. In hoofdstuk 3 pakken we dit probleem aan door een optimalisatie-algoritme te ontwikkelen dat gretig de ruimte van knooppuntgeometrieën verkent. Wij laten zien dat het algoritme in staat is hoge kloof-geometrieën te vinden in verschillende fysische omstandigheden. Bovendien tonen wij aan dat het algoritme waarschijnlijk convergeert naar globale maxima in de geometrische ruimte.

In hoofdstuk 4 richten we onze aandacht op (niet)lokale transportexperimenten in hybride supergeleiders, een veelgebruikte methode om de toestandsdichtheid in Majorana-apparaten te meten. De lineaire responsietheorie voorspelt dat de geleidingsmatrix van dergelijke apparaten aan verschillende symmetrieverhoudingen voldoet. Als voorbeeld, de twee-terminal geleiding wordt voorspeld symmetrisch te zijn in spanning, een manifestatie van deeltje-gat symmetrie. Experimentele geleidingsfiguren van Majorana-apparaten vertonen echter vaak aanzienlijke afwijkingen van deze symmetrieën. Een mogelijke verklaring is de aanwezigheid van quasideeltjesvergiftiging, die Majorana qubits belemmert. Wij laten zien dat een bias-afhankelijke tunnelbarrière ook leidt tot de afbraak van de symmetrieën van de geleidingsmatrix. Cruciaal is dat dit mechanisme de supergeleidende pariteit behoudt en daarom gunstig is voor Majorana qubits. We besluiten met het identificeren van verschillende fysische gedragingen die een onderscheid maken tussen symmetriebreking door een spanningsafhankelijke tunnelbarrière en dissipatie.

Tenslotte onderzoeken we in Hoofdstuk 5 een ander onderwerp in de mesoscopische fysica: multiplet superstroom in multiterminale Josephsonverbindingen. Eerder voorgestelde mechanismen om multiplets waar te nemen berusten op delicate niet-lokale Andreev-processen die door dissipatie worden verduisterd. Wij laten zien dat dit effect ook optreedt in gewone Josephson-tunnelingcircuits met alleen lokale Cooperpaaroverdrachten. Opmerkelijk is dat de multiplet superstroom blijft bestaan, zelfs wanneer de kring zich ver het oplaadregime bevindt waar alleen enkele Cooperparen in en uit het centrale eiland mogen tunnelen.

1

INTRODUCTION

1.1. PRELIMINARIES: SUPERCONDUCTIVITY AND BCS THEORY

In 1911, H. Kamerlingh Onnes made a remarkable discovery: when various metals are cooled down to temperatures close to absolute zero, their resistivity drops sharply to zero. This transition signals the appearance of a state of matter known as *superconductivity*. Although superconductivity rapidly became an intense area of experimental research, it was only in the ninety-fifties that its microscopic origin was explained theoretically. In 1956, Leon Cooper showed that at low temperatures a non-interacting Fermi sea is unstable with respect to the formation of correlated pairs [1]. A year later, Bardeen, Cooper and Schrieffer (BCS) used this insight to formulate the first microscopic theory of superconductivity [2]. BCS theory postulates that superconductivity arises as a result of a phonon-mediated attraction between electrons. This effective interaction causes electrons near the Fermi level to condense into *Cooper pairs* that mediate supercurrent. Energetically exciting a superconductor requires providing enough energy to break a Cooper pair. As a result, the single-particle excitation spectrum acquires a *superconducting gap* Δ.

Mathematically, the BCS mechanism is captured by the mean-field Hamiltonian [3]

$$\mathcal{H}_{\text{BCS}} = \sum_{\mathbf{k}\sigma} \varepsilon_{\mathbf{k}} c^{\dagger}_{\mathbf{k}\sigma} c_{\mathbf{k}\sigma} + \frac{\Delta}{2} e^{i\phi/2} \sum_{\mathbf{k}} c^{\dagger}_{\mathbf{k}\uparrow} c^{\dagger}_{-\mathbf{k}\downarrow} + \text{h.c.}, \tag{1.1}$$

where $c^{\dagger}_{\mathbf{k}\sigma}$ are electron creation operators for electrons with momentum $\mathbf{k}$ and spin projection σ, $\varepsilon_{\mathbf{k}}$ is the energy of an electron with momentum $\mathbf{k}$, and ϕ is the superconducting phase. By introducing the Nambu spinor

$$\Psi_k = \begin{pmatrix} c_{\mathbf{k},\uparrow} & c_{\mathbf{k},\downarrow} & c^{\dagger}_{-\mathbf{k},\downarrow} & -c^{\dagger}_{-\mathbf{k},\uparrow} \end{pmatrix}^T, \tag{1.2}$$

we rewrite Eq. (1.1) in a more convenient form using the Bogoliubov-De Gennes (BdG) transformation

$$\mathcal{H}_{\text{BCS}} = \frac{1}{2} \sum_{\mathbf{k}} \Psi^{\dagger}_{k} H_{\text{BdG}}(\mathbf{k}) \Psi_k \tag{1.3}$$

where

$$H_{\text{BdG}}(\mathbf{k}) = \begin{pmatrix} \varepsilon_{\mathbf{k}} & 0 & \Delta & 0 \\ 0 & \varepsilon_{\mathbf{k}} & 0 & \Delta \\ \Delta & 0 & -\varepsilon_{\mathbf{k}} & 0 \\ 0 & \Delta & 0 & -\varepsilon_{\mathbf{k}} \end{pmatrix} = \varepsilon_{\mathbf{k}} \tau_z \sigma_0 + \Delta \tau_x \sigma_0. \tag{1.4}$$

Here σ_i and τ_i are the Pauli matrices acting on spin and electron-hole space. The eigenstates of $H_{\text{BdG}}(\mathbf{k})$

$$\psi_{\mathbf{k}i} = \begin{pmatrix} u_{\mathbf{k}i\uparrow} & u_{\mathbf{k}i\downarrow} & v_{\mathbf{k}i\uparrow} & v_{\mathbf{k}i\downarrow} \end{pmatrix} \tag{1.5}$$

allow us to define Bogoliubov quasiparticle operators $\gamma_{\mathbf{k}i}$ that bring (1.1) to a diagonal form

$$\mathcal{H}_{\text{BCS}} = \frac{1}{2} \sum_{\mathbf{k}i} \varepsilon_{\mathbf{k}i} \gamma^{\dagger}_{\mathbf{k}i} \gamma_{\mathbf{k}i}. \tag{1.6}$$

The factor of 1/2 in equation (1.6) betrays an important artifact of the BdG transformation, namely that it artificially doubles the degrees of freedom of Hamiltonian. This redudancy is embodied by the anti-unitary *particle-hole* symmetry (PHS) $\mathscr{P} = \tau_y \sigma_y K$:

$$\mathscr{P} H_{\mathrm{BdG}}(\mathbf{k}) \mathscr{P}^{-1} = -H_{\mathrm{BdG}}(-\mathbf{k}), \tag{1.7}$$

which implies that a solution $\psi_{\mathbf{k}i}$ with energy $\varepsilon_{\mathbf{k}i}$ has a particle-hole symmetric partner $\psi_{\mathbf{k}i}$ with energy $-\varepsilon_{\mathbf{k}i}$. In second quantization terms, for any creation operator of a Bogoliubov excitation at energy E we may write

$$\gamma(E) = \gamma^{\dagger}(-E). \tag{1.8}$$

Hence populating the state $\gamma(E)$ is the same as removing a particle from $\gamma(-E)$.

1.2. ANDREEV PHYSICS IN SUPERCONDUCTOR-NORMAL INTERFACES

Throughout the course of this thesis, we will study devices that combine properties of semiconductors with superconductivity. Experimentally, this is achieved by exploiting the *proximity effect*, in which a normal region in the vicinity of a superconductor acquires a part of its superconducting properties. Intuitively, this effect occurs because Cooper pairs from the superconductor penetrate into the normal region as long as the normal-superconductor (NS) interface is sufficiently transparent. The charge transfer process that underpins this phenomenon is *Andreev reflection* (AR), which we explore in this section.

1.2.1. ANDREEV REFLECTION

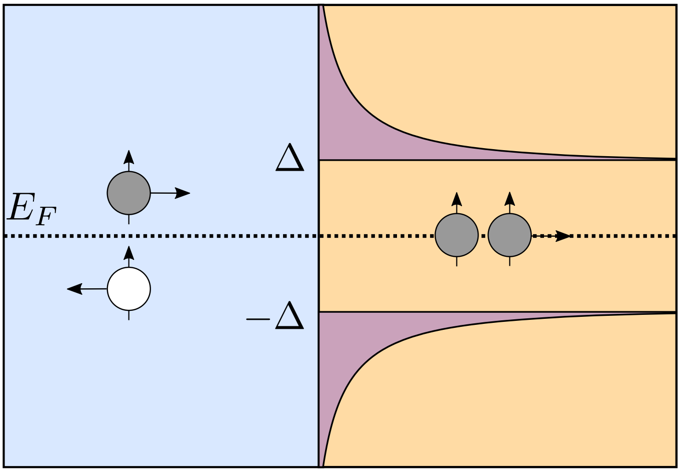

Figure 1.1: Andreev reflection in a normal-superconductor interface. An electron traveling in the metal with energy $\varepsilon - E_F < \Delta$ is not allowed to propagate in the superconductor because there are no available states. Instead, it can Andreev reflect as a hole with energy $-\varepsilon$. Physically this corresponds to injecting a Cooper pair in the superconducting condensate.

We consider the simplest system in which Andreev reflection can take place: a one-dimensional normal metal-superconductor junction. Consider an electron traveling in the metal towards the superconductor with subgap energy $\varepsilon - E_F < \Delta$ (where E_F is the Fermi energy). When the electron reaches the NS boundary, it cannot propagate into the superconductor because there are no single-particle states available below the superconducting gap Δ. It must be reflected to the normal metal. Naturally, it can reflect as an electron with opposite velocity. However, superconductors allow another process: Andreev reflection as a hole with opposite spin and energy $-\varepsilon$. Physically, this corresponds to an electron "dragging" a partner electron to form a Cooper pair in the superconductor. The opposite process is also allowed: a hole can be retroflected as an electron, which corresponds to a Cooper pair tunneling to the normal region. We visually summarize Andreev reflection in Fig. 1.1.

1.2.2. ANDREEV BOUND STATES

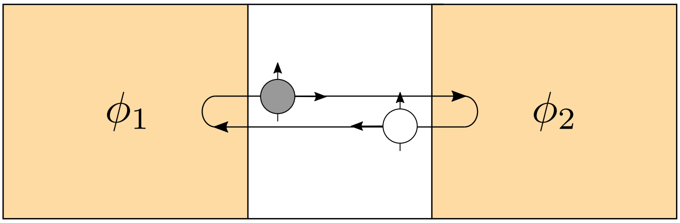

Figure 1.2: Andreev bound states in Josephson junctions form as a result of successive Andreev reflections that interfere constructively.

Let us now consider what happens when a normal region is sandwiched between two superconductors, that is, an SNS Josephson junction. From the previous subsection, we know that an electron traveling towards a superconducting contact will undergo Andreev reflection. The resulting hole will travel to the opposite superconducting contact and Andreev reflect as an electron, restarting the cycle. We conclude that the superconducting contacts act as potential barriers that confine the motion of quasiparticles in the normal region through successive Andreev reflections (Fig 1.2). If these reflections interfere constructively, they give rise to an *Andreev bound state* (ABS). Unlike bound states in non-superconducting systems, ABS mediate a Josephson supercurrent because each Andreev reflection results in a charge transfer of $2e$.

To derive the spectrum of ABS, we consider two clean superconducting contacts with phase difference $\phi = \phi_2 - \phi_1$ connected by a disordered normal region. We consider the short junction limit, in which the quasiparticle dwell time W/v_F (with v_F the Fermi velocity, W the width of the normal region) is much larger than the Andreev reflection time $\hbar/\Delta$, as follows from the uncertainty relation. We formalize this treatment of the problem through the *scattering formalism*, which analyzes how electron waves entering a superconductor reflect from it, and from the junction. Scattering states at energy ε in the left and normal regions are superpositions of incoming and outgoing states:

$$\Psi_L = \sum_{c=e,h} a_{c,L}|c_{L,\mathrm{in}}\rangle + b_{c,L}|c_{L,\mathrm{out}}\rangle \Psi_R = \sum_{c=e,h} a_{c,R}|c_{L,\mathrm{in}}\rangle + b_{c,R}|c_{R,\mathrm{out}}\rangle \tag{1.9}$$

Incoming waves that interact with the disordered region are normal-reflected according to the scattering matrix S_N:

$$\begin{pmatrix} b_{e,R} \\ b_{e,L} \\ b_{h,R} \\ b_{h,L} \end{pmatrix} = S_N \begin{pmatrix} a_{e,R} \\ a_{e,L} \\ a_{h,R} \\ a_{h,L} \end{pmatrix} \tag{1.10}$$

Because the normal region does not mix electrons and holes, S_N is block-diagonal in electron-hole space:

$$S_N = \begin{pmatrix} s_N & 0 \\ 0 & s_N \end{pmatrix}, s_N = \begin{pmatrix} r & t \\ t & r \end{pmatrix}. \tag{1.11}$$

Here we have used the short-junction approximation to neglect the energy dependence of s_N. At energies below the bulk superconducting gap ($\varepsilon < \Delta$), there are no propagating states in the superconductors. Therefore, outgoing particles that come into contact with a superconducting terminal will be Andreev reflected:

$$\begin{pmatrix} a_{e,R} \\ a_{e,L} \\ a_{h,R} \\ a_{h,L} \end{pmatrix} = S_A(\varepsilon) \begin{pmatrix} b_{e,R} \\ b_{e,L} \\ b_{h,R} \\ b_{h,L} \end{pmatrix} \tag{1.12}$$

where

$$S_A = \begin{pmatrix} 0 & s_A(\varepsilon) \\ s_A(\varepsilon)^* & 0 \end{pmatrix}, s_A = e^{-i \arccos \varepsilon/\Delta} \begin{pmatrix} e^{i\varphi/2} & 0 \\ 0 & e^{-i\varphi/2} \end{pmatrix} \tag{1.13}$$

has a block off-diagonal structure because the superconductors only mix electron and hole degrees of freedom. Plugging (1.10) into (1.12) we obtain

$$(\mathbb{1} - S_A(\varepsilon) S_N) \begin{pmatrix} a_{e,R} \\ a_{e,L} \\ a_{h,R} \\ a_{h,L} \end{pmatrix} = 0 \tag{1.14}$$

Equation (1.14) implies that $\det(\mathbb{1} - s_A(\varepsilon) s_N(\varepsilon)) = 0$. Solving this equation yields the short junction spectrum [4]

$$E = \pm\Delta\sqrt{1 - t \sin^2 \frac{\varphi}{2}}, \tag{1.15}$$

which is two-fold degenerate due to spin rotation symmetry. Because the ABS disperse with ϕ, they mediate a supercurrent given by

$$I = -\frac{2e}{h}\frac{\partial E}{\partial \varphi} \tag{1.16}$$

1.3. MAJORANA BOUND STATES

1.3.1. INTRODUCTION TO MAJORANA BOUND STATES

A Majorana fermion is a hypothetical particle that is its own antiparticle. Mathematically, this implies that Majorana operators are hermitian:

$$\gamma^\dagger = \gamma. \tag{1.17}$$

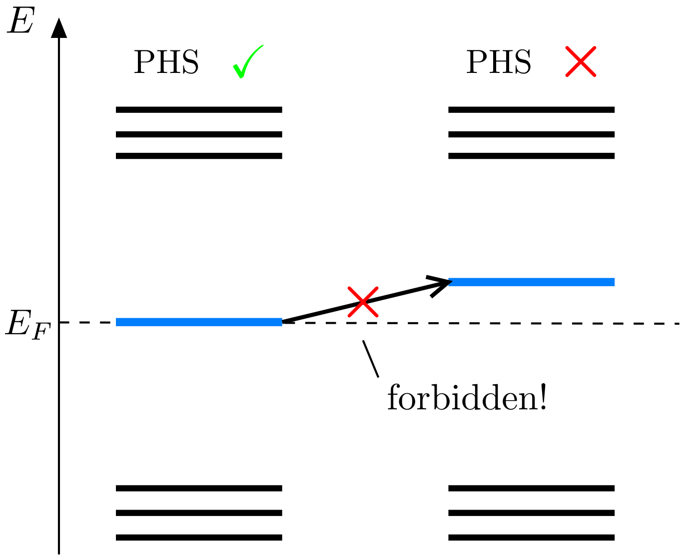

Figure 1.3: Schematic spectrum of a superconductor hosting Majorana bound states separated from other levels by an energy gap. Particle-hole symmetry pins Majorana bound states at zero energy and thus protects the ground state degeneracy. Removing the Majoranas from zero energy requires closing the bulk gap or bringing the Majorana modes sufficiently close so that they hybridize. Figure adapted from the *Online course on topology in condensed matter* (https://topocondmat.org), used under CC-BY-SA 4.0.

While they were initially studied in the context of high-energy physics, Majoranas are also conjectured to appear as localized quasiparticles in condensed matter systems. In this thesis, we focus on schemes based on one-dimensional superconductors. Superconductors are a natural place to search for Majoranas because PHS dictates that zero-energy excitations automatically fulfill the condition (1.17). However, as we will see in a moment, these excitations do not behave like fermions and therefore it is more appropriate to call them *Majorana bound states* (MBS).

MBS display two remarkable properties that distinguish them from conventional fermionic excitations. First, a collection of N spatially separated MBS spans a $2^{N/2}$-dimensional ground state manifold that is immune to local perturbations smaller than the energy gap. To see this, consider a superconductor hosting zero energy MBS energetically separated from the remaining states by a spectral gap, as shown schematically in Fig. 1.3. Simply moving these levels away from zero energy is forbidden because it would break PHS. Indeed, the only way to lift this degeneracy without violating PHS is to close the superconducting gap or to bring the MBS close to each other so that they hybridize. In other words, MBS are *topologically protected* by PHS. The second property is related to exchange statistics. Exchanging regular fermions multiplies the system's wavefunction by a factor -1. In contrast, MBS have so-called *non-Abelian statistics*: exchanging a pair of MBS (also known as *braiding*) induces a non-trivial unitary transformation in the ground state manifold. Crucially, this unitary operation is determined strictly by the topology of the exchange (that is, which Majoranas are exchanged), and not by the specific geometry or dynamics of the process.

Reliably observing topological protection and non-Abelian statistics would be of fundamental scientific interest, but also have practical implications for quantum computing. Qubits are inevitably subject to errors caused by coupling to a dissipative environment and imperfect control. Avoiding these errors is the main obstacle to building a useful quantum computer. A well-known approach to this problem is to use quantum error correction protocols that encode information in a redundant fashion. However, these schemes often have a large overhead and require high gate fidelities to begin with. Using MBS as qubits is an alternative, hardware-native path towards fault-tolerance: quantum information stored in MBS is naturally protected from their environment and, because most quantum gates can be implemented through braiding, unitary errors are suppressed.

1.3.2. RELATION TO TOPOLOGY

In the previous subsection, we saw that MBS are insensitive to perturbations in the system Hamiltonian. This suggests that it should be possible to formulate a higher-level description of these systems that is independent of microscopic details. Such a description is indeed possible by means of *topological classification* of bulk Hamiltonians [5, 6].

Two gapped Hamiltonians H_1 and H_2 are considered topologically equivalent if H_1 can be continuously deformed to H_2 while i) maintaining a finite bulk energy gap and ii) preserving a given set of symmmetries. Conversely, if such a transformation does not exist, $H_{1/2}$ are said to be in different *topological phases*. In practice, it is unnecessary to explicitly construct these transformations to verify topological equivalence. One can instead compute a *topological invariant* for each Hamiltonian. Informally speaking, a topological invariant is an integer that labels different topological phases. Two Hamiltonians are topologically equivalent if their invariant is the same.

The symmetries and dimensionality of the system determine the appropriate topological invariant to use. In this thesis, we will concern ourselves with one-dimensional superconductors that only possess PHS. The topological invariant of these systems is the sign of the Pfaffian of the Hamiltonian:

$$Q = \operatorname{sgn} \operatorname{Pf}(i\mathscr{H}). \tag{1.18}$$

Because Q can only take on two values ± 1, it is said to be a $\mathbb{Z}_2$ invariant. Systems with $Q = -1$ host MBS and are dubbed as *topological* or *nontrivial*, whereas systems with $Q = +1$ are labeled *trivial* and do not contain MBS. Physically, the Pfaffian measures the fermion parity of the ground state and thus its value can only change when an odd number of levels cross zero energy. Such a crossing – known as a *fermion parity switch* – implies that it becomes energetically favorable to add or remove a Bogoliubov quasiparticle.

When $\mathscr{H}$ is translationally invariant and admits a Bloch decomposition $\mathscr{H} = \bigoplus_k H_{\mathrm{BdG}}(k)$, the invariant can be rewritten in a different form. In general, zero-energy crossings at finite momentum k_x are accompanied by another crossing of a particle-hole partner at $-k_x$. Therefore they leave the Pfaffian unchanged. There are, however, two special points in the Brillouin zone for which this reasoning does not apply: $k_x = 0$ and $k = \pi$, which are mapped to themselves by PHS. This implies that fermion parity switches must occur at $k_x = 0, \pi$. We may then write

$$Q = \operatorname{sgn}\left[\operatorname{Pf}(iH_{\mathrm{BdG}}(k_x = 0))\operatorname{Pf}(iH_{\mathrm{BdG}}(\pi))\right]. \tag{1.19}$$

1.3.3. REALIZING MAJORANAS IN SUPERCONDUCTORS: GENERAL CONSIDERATIONS

Previously we saw that the ground state degeneracy of a system with Majoranas is protected from local perturbations. This implies that the Majoranas states must have zero expectation value for any local observable. If that were not the case, the degeneracy would be lifted by arbitrarily weak perturbations that couple to the observable with finite expectation value. This immediately allows us to conclude that metals cannot support MBS because metallic excitations have definite charge and thus couple to electric fields. To realize Majoranas in condensed matter systems we must break charge conservation.

Superconductors remove charge conservation by coupling electrons and holes. Indeed, a generic excitation of the BdG Hamiltonian (1.4) schematically reads

$$\gamma^\dagger = u c_\uparrow^\dagger + v c_\downarrow. \tag{1.20}$$

However, Eq. (1.20) reveals another problem: Bogoliubov quasiparticles have definite spin! Put another way, the spin structure in Eq. (1.20) forces $\gamma^\dagger \neq \gamma$, which violates the Majorana condition (1.17).

In order to realize Majoranas, we need to somehow engineer a *spinless superconductor*. Generating an effective spinless material is relatively easy. Consider a metal with a spin-degenerate parabolic dispersion $\sim k^2$. Applying a Zeeman field $E_Z\sigma_z$ splits the spectrum into an aligned band with lower energy and an anti-aligned band with higher energy. By placing the chemical potential between the two bands, we populate the system with a single spin species – effectively a spinless system. We could then try to make the system superconduct by leveraging the proximity effect and placing it in the vicinity of a superconductor. However, conventional superconductors pair electrons in singlets and thus it is impossible to induce superconductivity in such a system! The problem is that, although we have broken spin rotation symmetry, the system still conserves spin in the z direction. To circumvent this limitation we introduce new ingredient: Rasbha spin-orbit coupling (SOC) $\alpha k_x \sigma_y \tau_z$. SOC introduces a spin canting angle at opposite $\mathbf{k}$, which makes it possible to induce superconductivity.

To summarize, there are three essential ingredients to realize topological superconductivity: a Zeeman field (or, more generally, a TRS-breaking term), Rashba spin-orbit coupling, and conventional superconductivity. Traditionally, experimental works have largely focused on combining these ingredients in proximitized semiconducting nanowires. However, this approach is hard to scale and requires large magnetic fields that compromise superconductivity in the parent superconductor. These issues are alleviated by a recently proposed platform based on Josephson junctions in two-dimensional electron gases (2DEG). We review this approach in the next subsection.

1.4. MAJORANA BOUND STATES IN A PLANAR SEMICONDUCTOR-SUPERCONDUCTOR HETEROSTRUCTURES

Josephson junctions formed by proximitizing a 2DEG with superconductors are fruitful searching grounds for interesting mesoscopic phenomena. On the one hand, the low density of states and gate-tunability of the semiconducting region make it possible to

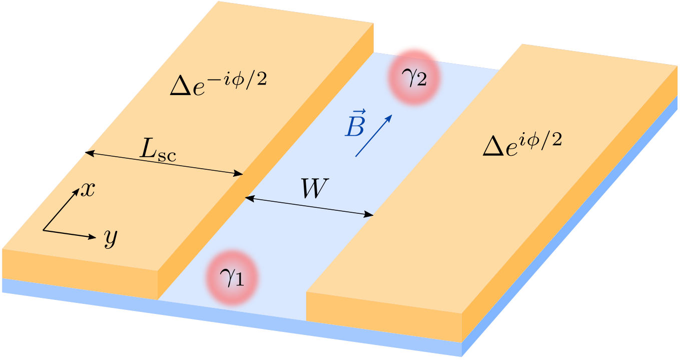

Figure 1.4: A Josephson junction made by proximitizing a 2DEG with Rashba spin-orbit coupling (blue) with two superconducting contacts (orange). At sufficiently strong in-plane magnetic fields the system enters a topological phase with MBS at the sample edges.

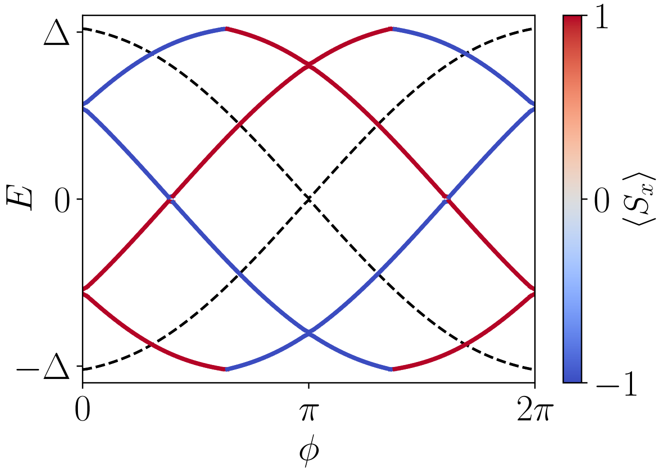

Figure 1.5: ABS spectrum of a narrow topological Josephson junction at $k_x = 0$ as a function of the superconducting phase difference. The dashed lines show the ABS energies when the magnetic field threading the junction is zero. The spectrum is doubly degenerate at any phase due to spin conservation, which prevents a topological phase transition. A finite Zeeman field splits the two spin species, allowing a switch of the ground state parity close to $\phi = \pi$.

resolve and manipulate individual ABS. On the other hand, the presence of strong spin-orbit coupling gives control over the spin of Andreev quasiparticles [7] and enables new phenomena such as the anomalous Josephson effect [8] and, most relevant for this thesis, topological superconductivity. Initial experimental works were met with difficulties in observing Josephson physics due to material quality. Gradual progress in nanofabrication techniques eventually circumvented these issues and, between 2015 and 2016, a series of experiments demonstrated high-quality semiconductor-superconductor contacts in epitaxial Al-InAs 2DEG heterostructures [9–11]. Shortly thereafter, two independent

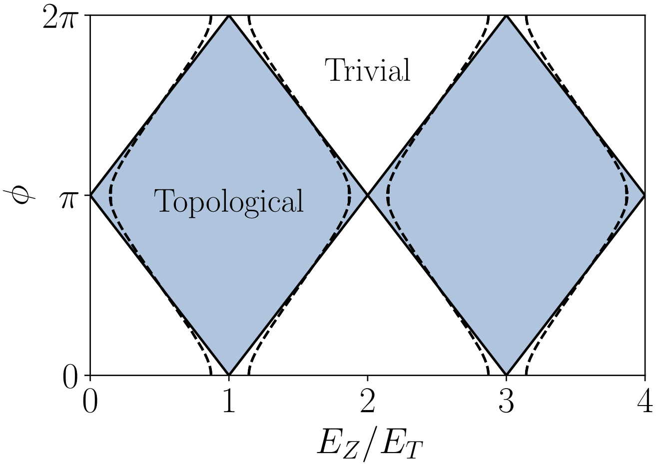

Figure 1.6: Phase diagram of a topological Josephson junction as a function of Zeeman field and superconducting phase difference. When normal reflection is absent in the system, the spectrum is doubly degenerate at $\phi = 0, \pi$. As a result, the $\mathbb{Z}_2$ index cannot change at those phases and the system is always topological at $\phi = \pi$ and trivial at $\phi = 0$. When normal reflection occurs the shape of the diamonds becomes distorted and allows topological phase transitions to occur at all values of ϕ.

works theoretically studied how 2DEG junctions can be used to create MBS [12, 13]. In comparison with the more established nanowire proposals, this approach has two main advantages. First, because it is based on a planar design, it is more flexible and in principle easier to scale to multiple qubits. Second, the superconducting phase difference across the junction significantly lowers the Zeeman fields required to drive the system into a topological regime.

TOPOLOGICAL JOSEPHSON JUNCTIONS

We consider a two-dimensional strip of semiconductor in proximity with two superconducting terminals and subject to an in-plane magnetic field (Fig.1.4). The contacts have width L_{SC} and the unproximitized region has width W. We model the 2DEG with a single band electron model with Rashba spin-orbit coupling. The BdG Hamiltonian of the system then reads

$$H_{\mathrm{N}} = \left(\frac{p_x^2 + p_y^2}{2m}\right)\tau_z + \alpha(k_x\sigma_y - ik_y\sigma_x)\tau_z + E_Z(y)\sigma_x, \tag{1.21}$$

where α is the Rashba spin-orbit strength and the Zeeman field has the form

$$E_Z(y) = \begin{cases} E_Z & -W/2 < y < W/2 \\ 0 & \text{elsewhere} \end{cases}. \tag{1.22}$$

In addition, the regions covered by superconductors experience a pairing interaction of the form

$$H_{\mathrm{S}} = \Delta\cos\left(\pm\frac{\phi}{2}\right)\tau_x + \Delta\sin\left(\pm\frac{\phi}{2}\right)\tau_y, \tag{1.23}$$

where ϕ is the superconducting phase difference across the junction. Because the Zeeman field breaks time-reversal symmetry (TRS) $\mathcal{T} = i\sigma_y K$ (with K denoting complex conjugation), we would naively expect this system to be in class D [5, 6]. However, the system has an effective TRS $\tilde{\mathcal{T}} = M_y\mathcal{T}$, where M_y is a mirror operator with respect to the y axis. As a result, the system is in class BDI and supports arbitrary numbers of Majorana modes. Breaking this symmetry, by e.g. allowing the superconducting contacts to have different superconducting gaps, restores the system to class D and stabilizes a topological phase with a single pair of Majorana modes.

To compute the topological properties of the system, we consider a translationally-invariant junction along x. From Eq. 1.19 we know fermion parity switches can only occur at particle-hole inviarant momenta $k_x = 0, \infty$. However, at $k_x \to \infty$ the Hamiltonian 1.21 asymptotically approaches that of free electrons, and thus $\mathrm{Pf}(iH_{\mathrm{BdG}}(k_x = \infty)) = 1$ [12]. It is therefore sufficient to compute the bound state spectrum at $k_x = 0$. By performing a gauge transformation $\Psi(x, y) \to e^{if(y)\sigma_x}\Psi(x, y)$ we remove the spin-orbit term and arrive at the Hamiltonian

$$H(k_x = 0) = \frac{p_y^2}{2m}\tau_z + E_Z(y)\sigma_x + H_{\mathrm{S}} \tag{1.24}$$

For simplicity, we limit our analysis to narrow junctions in the Andreev limit $\mu \gg \Delta$, such that normal reflection is negligible. In the absence of a magnetic field, we recover the short junction spectrum (1.15) (dashed lines in Fig. 1.5). Spin conservation forces the ABS to be doubly degenerate, thereby preventing a topological phase transition. Applying a Zeeman field splits the two spin species and, as a result, two non-degenerate zero-energy crossings appear in the vicinity of $\phi = \pi$. When the superconducting phase lies between these two crossing points, the system is in a topological phase and hosts MBS at the sample edges.

In Fig. 1.6 we show the resulting $\phi - E_Z$ topological phase diagram, which consists of a periodic diamond structure with alternating topological and trivial regions. Notably, the system is always topological at $\phi = \pi$ and trivial at $\phi = 0$. As a result, if the system is phase-biased at $\phi = \pi$, Majoranas appear at arbitrarily low magnetic fields. This occurs because mirror symmetry forces the ABS to be degenerate at $\phi = 0, \pi$ (Fig 1.5), which prevents a topological phase transition. However, this degeneracy is only present because we have assumed perfect Andreev reflection at the NS boundary. Several factors can cause Andreev quasiparticles to undergo normal reflection, such as low chemical potential, a chemical potential mismatch between normal and superconducting regions, or an imperfect interface. Finite normal reflection couples the left and right moving states and lifts the degeneracy at $\phi = 0, \pi$, causing the diamond structure to become distorted (dashed lines Fig. 1.6).

1.4.1. OPEN QUESTIONS AND STATE OF THE ART

In this subsection, we briefly summarize recent theoretical and experimental advances in the field of topological Josephson junctions. We review four main directions of research: enhancement of the topological gap, topological superconductivity induced through superconducting phases, material engineering, and experimental signatures of ABS and MBS.

ENHANCING THE TOPOLOGICAL GAP

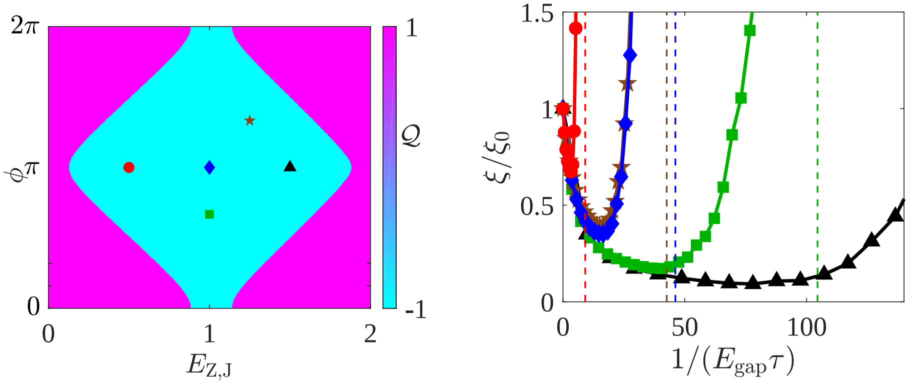

(a)

(b)

Figure 1.7: Effect of disorder on the Majorana localization length. (a) Numerical topological phase diagram of a Majorana junction. (b) The Majorana localization length as a function of the disorder-induced inverse mean free time for different points in the topological region marked in (a). Figure reproduced from Haim and Stern [14].

The primary advantages of Majorana junctions are that they require small magnetic fields and are relatively insensitive to variations in the chemical potential. However, this comes at the cost of small topological gaps, which weakens the topological protection in the system. Indeed, a straight Majorana junction with realistic material parameters only achieves gaps of the order of a few percent of the parent gap. The mechanism underlying the small energy gaps was explained in 1963 by de Gennes [16]. His analytical calculations showed that a soft gap arises in NS devices due to quasiparticles with large longitudinal momentum $k_x \approx k_F$ directed along the junction. Because these quasiparticles run almost parallel to the junction, they rarely come into contact with the superconductor and thus the proximity effect is reduced. In semiclassical terms, these trajectories have a long flight time τ_f (or equivalently a small Thouless energy $\hbar/\tau_f$) and therefore a small gap. To increase the topological gap, it is necessary to eliminate long-flight trajectories. A simple solution would be to use low fillings [17]; however, tuning to this regime requires precise microscopic knowledge of the junction and increases the sensitivity to disorder.

Another way to limit long trajectories was pointed out by Haim and Stern [14]. They analytically showed that weak non-magnetic disorder decreases the localization length of Majoranas. At a microscopic level, this enhancement occurs because in the presence of disorder the effective s-wave order parameter becomes

$$|\Delta_s^{\text{eff}}| = |\Delta_s| + \frac{1}{2\tau_s}, \tag{1.25}$$

while p-wave pairing behaves as

$$|\Delta_p^{\text{eff}}| = |\Delta_p| - \frac{1}{2\tau_p}. \tag{1.26}$$

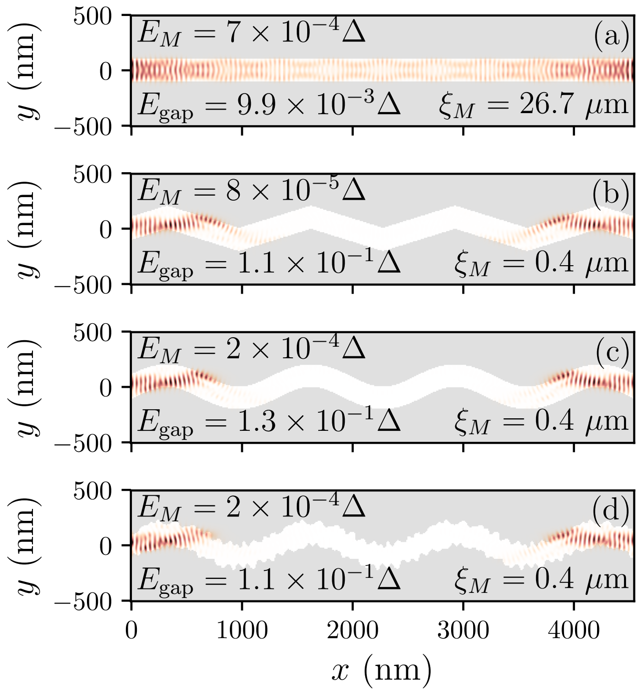

Figure 1.8: Majorana wavefunctions for different Josephson junction geometries. (a) a straight junction, (b) a zigzag system, (c) a sinusoidal system, (d) a sinusoidal with disordered edges Each figure also shows the topological gap of the system along with the Majorana localization length. We observe that the zigzag-like systems improve the gap by an order of magnitude and the localization length by two orders of magnitude. Figure adapted from Laeven et al. [15]

Here τ_i are the mean free times that arise from the disorder potential. We observe that the effective s-wave gap increases with disorder, whilst the p-wave gap decreases. In Majorana junctions, the gap is limited by high momentum states, where spin-orbit coupling forces electrons at opposite k to have almost parallel spins. The pairing at high momentum is therefore largely s-wave. In this case, introducing disorder does not cause intra-channel backscattering and therefore increases the effective pairing gap. In contrast, states close to $k_x = 0$ are largely p-wave paired, and thus the low momentum gap decreases with increasing disorder. As Fig 1.7(b) shows, the competition between these two energy scales causes the localization length to evolve nonmonotonically with increasing disorder. The localization length initially decreases due to the increase in s-wave pairing of high momentum states. At the same time, the low momentum p-wave pairing begins to increase. When it becomes equal to the s-wave gap, the localization length begins to increase.

In realistic experimental settings, disorder is uncontrollable. It is therefore desirable to find deterministic ways to increase the topological gap. Laeven et al. [15] studied an alternative approach based on geometry modulation. Their primary finding is that modulating the shape of the junction to remove long trajectories (by, e.g. making it zigzag-shaped) dramatically improves the topological gap and localization length. Importantly, the gap enhancement is independent of the precise shape of the junction, provided that it cuts off long trajectories. In Fig.1.8 we show the Majorana wavefunctions along with the topological gap for straight and modulated geometries with identical Hamiltonian parameters. We observe that in zigzag-like junctions the gap is an order of magnitude larger, while the localization length is two orders of magnitude smaller. A follow-up work by Paudel et al. [18] also found a gap enhancement in periodically modulated junctions, which the authors attribute to renormalized spin-orbit coupling originating from band-structure folding [19].

Although zigzag junctions have been fabricated and measured, evidence of a robust gap enhancement remains elusive [20, 21]. One potential issue with zigzag-like junctions is that a magnetic field directed along x generates screening supercurrents that suppress the amplitude of Andreev reflection and the induced gap [22]. It remains unclear whether the gap enhancement would persist in these circumstances.

PHASE-INDUCED TOPOLOGICAL SUPERCONDUCTIVITY

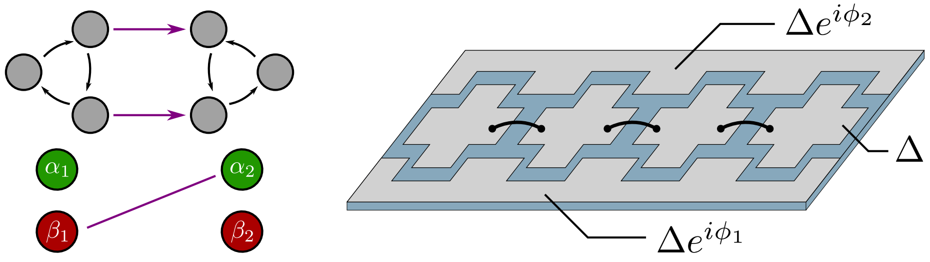

(a) (b)

Figure 1.9: Scheme for phase-induced topological superconductivity in planar semiconductor-superconductor heterostructures. (a) A toy tight-binding model that supports perfectly localized MBS without a Zeeman field. The unit cell is a ring with $N \geq 3$ superconducting sites coupled through spin-orbit terms. A single ring supports a pair of MBS when the superconducting phases form a vortex. When the coupling of two topological rings is tuned to the "sweet spot", one pair of MBS hybridize, while the remaining MBS remain uncoupled and perfectly localized. (b) An implementation of the previous toy model in a planar architecture. The blue regions represent a 2DEG in the normal state, while the gray regions are proximitized with phase-biased superconductors. Figures reproduced from [23].

As we have seen, phase difference across a Josephson junction lowers the magnetic field required to induce topological superconductivity. A natural follow-up question is whether it is possible to go a step further and remove the need for a Zeeman field altogether. Earlier work by van Heck et al. provides an important clue [25]: using the scattering formalism they proved that, in the absence of a magnetic field, Josephson junctions can only support zero energy solution if i) they contain at least three superconducting terminals and ii) the superconducting phases θ_i form a discrete vortex, i.e. $\sum_i \theta_i = 2\pi$. In this section, we briefly review two proposals for phase-induced topological superconductivity in planar geometries that directly exploit this concept. For a more thorough review of the subject, we refer the reader to [23].

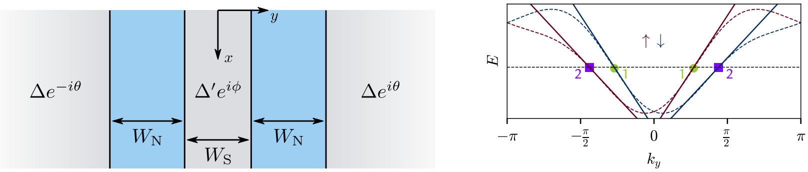

(a) (b)

Figure 1.10: (a) A phase-biased SNSNS junction. This device supports Majorana bound states provided that the two spin branches have different Fermi velocities in the transverse direction. (b) Transverse dispersion relation of the junction in a model with next-nearest neighbor hoppings, which results in different Fermi velocities for the two spin branches. Figures reproduced from [24].

In the first of these proposals [23], the authors begin by studying a toy tight-binding model that supports perfectly localized MBS and where the only source of TRS-breaking is superconducting phases. The building block of the model is a ring with $N \geq 3$ sites (Fig.1.9 (a)), where each site is proximitized by a phase-biased s-wave superconductor, and electrons are allowed to hop through a spin-orbit term. A single ring is shown to support a pair of MBS provided that the superconducting phases wind in a vortex, in agreement with the findings of van Heck et al. Remarkably, when two rings are connected, it is possible to tune the system into a "sweet spot" where two MBS remain uncoupled and perfectly localized, whilst the remaining pair gaps out (bottom of Fig. 1.9 (a)). Having established the basic properties of the toy model, the authors turn to investigate a practical implementation in a planar semiconductor-superconductor architecture which we illustrate in Fig. 1.9 (b). The platform is similar to Majorana Josephson junctions, but contains additional phase-biased superconductors in the middle of the junction; the resulting periodic arrangement that resembles the previously considered ring model. Numerical tight-binding simulations show that the device supports MBS when the phases form a vortex. The authors then discuss the experimental viability of the proposal and conclude that it is within reach of current fabrication methods. Nevertheless, simulations indicate that the topological gaps at experimentally realistic semiconductor densities are modest (2-3% of the parent gap).

Another approach put forward recently by Lesser et al [24] relies on Fermi velocity engineering along the transverse direction to drive a topological phase transition. In Fig. 1.10 (a) we show the proposed setup, which consists of an SNSNS junction where the outermost superconductors are semi-infinite and have order parameters $\Delta e^{\pm i\theta}$, and the central superconductor has a finite width W_S with order parameter $\Delta' e^{i\phi}$). The motion of electrons along y is described by the linear dispersion $H^{\pm}_{0,j} = \pm v_j \partial y$, where v_j is the Fermi velocity of the j-th spin branch (Fig. 1.10 (b)). At $k_x = 0$ the j-th branch crosses the Fermi level when the following condition holds:

$$\cos\theta + \tanh\left(\frac{W_S \Delta'}{v_j}\right)\cos\phi = 0. \tag{1.27}$$

If the velocities of the two branches are unequal the two spin branches cross the Fermi level at different points, signaling a topological phase transition. The authors then discuss several schemes to induce unequal v_j, namely, i) replacing the 2DEG with a monolayer of transition metal dichalcogenides, ii) applying a periodic electrostatic potential along the junction, and iii) tuning the system to have more than one occupied subband in the z direction of the 2DEG.

EXPERIMENTAL PROGRESS: MATERIAL ENGINEERING

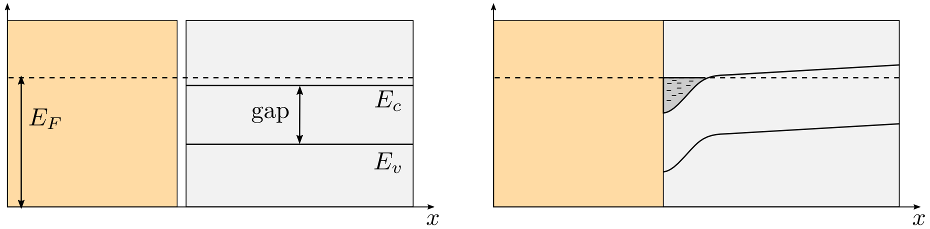

(a) (b)

Figure 1.11: Schematic band diagrams of a metal-semiconductor interface. (a) Band diagram before the materials are in contact. The metal is filled up to the Fermi level, while the semiconductor has a filled valence band and a partially filled conduction band. (b) After contact the semiconductor's bands bend downward and form a charge accumulation region near the interface.

Although research on proximitized 2DEGs goes back several decades [26], progress in the field was hampered by the presence of soft superconducting gaps – that is, a residual density of states at energies below the induced superconducting gap. These difficulties can be traced back to material synthesis challenges that arise when combining properties of superconductivity and semiconducting 2DEGs. First, in order to induce a hard superconducting gap in the proximitized regions, it is necessary to create a transparent superconductor-semiconductor interface through proper band alignment. In particular, the semiconductor's electron affinity must be larger than the superconductor's work function so that the semiconducting bands bend downwards at the interface [27, 28] (Fig. 1.11(a)). The charges confined in the resulting accumulation region interact strongly with the superconductor and thus contribute to a large induced gap (Fig. 1.11(b)). Another challenge is related to the Hamiltonian parameters of the material stack in the heterostructure. In order to preserve superconductivity when magnetic fields are applied, the parent superconductor must have a large critical field. At the same time, the 2DEG should have large mobility (indicative of low disorder), spin-orbit coupling (which results in a large topological gap), and g-factor (so that the applied magnetic fields can remain small). Narrow bandgap semiconductors such as InAs and InSb fulfill these conditions, but growing high-quality quantum wells in these systems is challenging [29]. Recent progress in fabrication techniques have made great strides in solving these issues and kickstarted the search for topological superconductivity in 2DEG Josephson junctions. We briefly review some of these developments below.

Between 2015 and 2016, a series of experiments characterized InAs 2DEGs proximitized with epitaxially-grown Al[29]. Tunneling spectroscopy experiments with quantum point contacts in NS junctions revealed a hard superconducting gap in the tunneling regime and conductance plateaus at $4e^2/h$ in the open regime [30]. Subsequent experiments studied SNS junctions and observed multiple Andreev reflections, indicating high transparency between the semiconductor and superconductor [31]. High quality semiconductor-superconductor interfaces were also reported in inverted NbN-GaAs heterojunctions [32], NbTi contacted through a thin layer of epitaxial aluminum [33] and Nb-$In_{0.75}Ga_{0.25}As$ [34].

In 2019, induced superconductivity was observed in InSb 2DEGs proximitized by ex-situ NbTiN[35]. In comparison with InAs, InSb has a larger g-factor and spin-orbit coupling. However, it is difficult to proximitize with in-situ Al, presumably due to band offset issues [36]. This issue was overcome by replacing InSb with the ternary compound $InSb_{1-x}As_x$, which was successfully proximitized with in-situ grown Al while retaining high spin-orbit and g-factor. Another approach is to proximitize free-standing InSb nanoflags [37, 38].

EXPERIMENTAL PROGRESS: SIGNATURES OF MBS AND MANIPULATING ANDREEV STATES

In 2018 two works appeared that claimed to observe evidence of topological superconductivity. In [39] the authors studied a phase-biased Al-InAs Josephson junction. The authors measure the local density of states through tunneling spectroscopy and observe non-quantized zero-bias peaks. Furthermore, they find that the peaks develop at lower fields when $\phi = \pi$. Another work published almost simultaneously studied a phase-biased Al-HgTe junction through tunneling spectroscopy [40]. Their findings are qualitatively similar to those of Ref. [39]. In addition, the authors mapped out regions in $\phi - B_x$ space that showed a zero-bias anomaly and found a diamond-like shape that resembles the phase diagram we introduced in Sec. 1.4. When interpreting these results, the usual caveats related to local tunneling conductance apply. First, a large body of theoretical work shows that trivial ABS can also manifest as zero-bias peak [41–44]. Additionally, the conductance in both studies clearly shows a soft gap, which precludes a topological phase by definition. A few months later, Dartiailh et al. [45] published a study on Al-InAs junctions in which the phase is left as a free parameter. At sufficiently high in-plane magnetic fields, critical current maps show a closing and reopening of the gap concomitantly with a π phase jump in the current phase relation. The combination of spin-orbit coupling and Zeeman splitting can result in a topologically trivial π phase jump [35, 46, 47]. However, the authors claim this mechanism is inaccessible in the range of magnetic fields considered, and instead interpret these observations as a topological phase transition.

A more recent generation of experiments focused on topological superconductivity studies devices with additional leads. In [48] the authors report measurements of a phase-biased Al-InAs junction connected to quantum point contacts on both ends of the sample. In some regions of parameter space, local conductance at both ends shows states coming down to zero energy followed by a zero-bias peak. A follow-up work investigates a similar device using nonlocal conductance experiments [49]. Nonlocal conductance is in principle a more reliable way of detecting topological phase transitions because it probes bulk properties of the system [50]. The experiments observe an apparent closing of the bulk in nonlocal conductance followed by correlated zero-bias peaks on both ends. However, both nonlocal and local conductances clearly show a soft gap. Moreover, Ref. [51] showed that regions where the order parameter vanishes can host ABS that mimic nonlocal signatures.

A separate direction of research focuses on characterizing and manipulating the subgap Andreev spectrum. In [52], the authors measure the critical current of a DC

SQUID with Al-InAs junctions as a function of the flux threading the loop. A local tunnel probe allows simultaneous measurement of the energies of the ABS which they fit using the short junction spectrum(1.15). Having obtained a model of the ABS spectrum, the authors compute the critical current $I_c = \max_\phi I(\phi)$ and find very good agreement with the measured critical current values. Finally, building on a recent theoretical proposal by Stern and Berg [53], two experimental works showed that applying a perpendicular magnetic field induces a superconducting texture that allows controlling the spatial position of ABS [54, 55].

1.5. STRUCTURE OF THIS THESIS

Here we give a brief overview of the topics explored in the following chapters.

1.5.1. SUPERCURRENT-INDUCED MAJORANA BOUND STATES IN A PLANAR GEOMETRY

We propose a new setup for creating Majorana bound states in a two-dimensional electron gas Josephson junction. Our proposal relies exclusively on a supercurrent parallel to the junction as a mechanism for breaking time-reversal symmetry. We show that combined with spin-orbit coupling, supercurrents induce a Zeeman-like spin splitting. Further, we identify a new conserved quantity—charge-momentum parity—that prevents the opening of the topological gap by the supercurrent in a straight Josephson junction. We propose breaking this conservation law by adding a third superconductor, introducing a periodic potential, or making the junction zigzag-shaped. By comparing the topological phase diagrams and practical limitations of these systems we identify the zigzag-shaped junction as the most promising option.

1.5.2. GREEDY OPTIMIZATION OF THE GEOMETRY OF MAJORANA JOSEPHSON JUNCTIONS

Josephson junctions in a two-dimensional electron gas with spin-orbit coupling are a promising candidate to realize topological superconductivity. While it is known that the geometry of the junction strongly influences the size of the topological gap, the question of how to construct optimal geometries remains unexplored. We introduce a greedy numerical algorithm to optimize the shape of Majorana junctions. The core of the algorithm relies on perturbation theory and is embarrassingly parallel, which allows it to explore the design space efficiently. By introducing stochastic variations in the junction Hamiltonian, we avoid overfitting geometries to specific system parameters. Furthermore, we constrain the optimizer to produce smooth geometries by applying image filtering and fabrication resolution constraints. We run the algorithm in various setups and find that it reliably produces geometries with increased topological gaps over large parameter ranges. The results are robust to variations in the optimization starting point and the presence of disorder, which suggests the optimizer is capable of finding global maxima.

1.5.3. CONDUCTANCE ASYMMETRIES IN MESOSCOPIC SUPERCONDUCTING DEVICES DUE TO FINITE BIAS

Tunneling conductance spectroscopy in normal metal-superconductor junctions is an important tool for probing Andreev bound states in mesoscopic superconducting devices, such as Majorana nanowires. In an ideal superconducting device, the subgap conductance obeys specific symmetry relations, due to particle-hole symmetry and unitarity of the scattering matrix. However, experimental data often exhibits deviations from these symmetries or even their explicit breakdown. In this work, we identify a mechanism that leads to conductance asymmetries without quasiparticle poisoning. In particular, we investigate the effects of finite bias and include the voltage dependence in the tunnel barrier transparency, finding significant conductance asymmetries for realistic device parameters. It is important to identify the physical origin of conductance asymmetries: in contrast to other possible mechanisms such as quasiparticle poisoning, finite-bias effects are not detrimental to the performance of a topological qubit. To that end, we identify features that can be used to experimentally determine whether finite-bias effects are the source of conductance asymmetries.

1.5.4. MULTIPLET SUPERCURRENT IN JOSEPHSON TUNNELING CIRCUITS

The multi-terminal Josephson effect allows DC supercurrent to flow at finite commensurate voltages. Existing proposals to realize this effect rely on nonlocal Andreev processes in superconductor-normal-superconductor junctions. However, this approach requires precise control over microscopic states and is obscured by dissipative current. We show that standard tunnel Josephson circuits also support multiplet supercurrent mediated only by local tunneling processes. Furthermore, we observe that the supercurrents persist even in the high charging energy regime in which only sequential Cooper transfers are allowed. Finally, we demonstrate that the multiplet supercurrent in these circuits has a quantum geometric component that is distinguishable from the well-known adiabatic contribution.

REFERENCES

[1] L. N. Cooper, *Bound electron pairs in a degenerate fermi gas,* Phys. Rev. **104**, 1189 (1956).

[2] J. Bardeen, L. N. Cooper, and J. R. Schrieffer, *Theory of superconductivity,* Phys. Rev. **108**, 1175 (1957).

[3] M. Tinkham, *Introduction to superconductivity* (Courier Corporation, 2004).

[4] C. W. J. Beenakker, *Universal limit of critical-current fluctuations in mesoscopic Josephson junctions,* Phys. Rev. Lett. **67**, 3836 (1991).

[5] A. Kitaev, *Periodic table for topological insulators and superconductors,* in *AIP conference proceedings*, Vol. 1134 (American Institute of Physics, 2009) pp. 22–30.

[6] S. Ryu, A. P. Schnyder, A. Furusaki, and A. W. Ludwig, *Topological insulators and superconductors: tenfold way and dimensional hierarchy,* New Journal of Physics **12**, 065010 (2010).

[7] N. M. Chtchelkatchev and Y. V. Nazarov, *Andreev quantum dots for spin manipulation,* Phys. Rev. Lett. **90**, 226806 (2003).

[8] T. Yokoyama, M. Eto, and Y. V. Nazarov, *Anomalous josephson effect induced by spin-orbit interaction and zeeman effect in semiconductor nanowires,* Physical Review B **89**, 195407 (2014).

[9] J. Shabani, M. Kjaergaard, H. J. Suominen, Y. Kim, F. Nichele, K. Pakrouski, T. Stankevic, R. M. Lutchyn, P. Krogstrup, R. Feidenhans'l, S. Kraemer, C. Nayak, M. Troyer, C. M. Marcus, and C. J. Palmstrøm, *Two-dimensional epitaxial superconductor-semiconductor heterostructures: A platform for topological superconducting networks,* Physical Review B **93** (2016), 10.1103/physrevb.93.155402.

[10] M. Kjaergaard, H. Suominen, M. Nowak, A. Akhmerov, J. Shabani, C. Palmstrøm, F. Nichele, and C. Marcus, *Transparent semiconductor-superconductor interface and induced gap in an epitaxial heterostructure josephson junction,* Physical Review Applied **7** (2017), 10.1103/physrevapplied.7.034029.

[11] H. J. Suominen, J. Danon, M. Kjaergaard, K. Flensberg, J. Shabani, C. J. Palmstrøm, F. Nichele, and C. M. Marcus, *Anomalous fraunhofer interference in epitaxial superconductor-semiconductor josephson junctions,* Physical Review B **95** (2017), 10.1103/physrevb.95.035307.

[12] M. Hell, M. Leijnse, and K. Flensberg, *Two-dimensional platform for networks of majorana bound states,* Physical Review Letters **118** (2017), 10.1103/physrevlett.118.107701.

[13] F. Pientka, A. Keselman, E. Berg, A. Yacoby, A. Stern, and B. I. Halperin, *Topological superconductivity in a planar josephson junction,* Physical Review X **7** (2017), 10.1103/physrevx.7.021032.

[14] A. Haim and A. Stern, *Benefits of weak disorder in one-dimensional topological superconductors,* Physical Review Letters **122** (2019), 10.1103/physrevlett.122.126801.

[15] T. Laeven, B. Nijholt, M. Wimmer, and A. R. Akhmerov, *Enhanced proximity effect in zigzag-shaped majorana josephson junctions,* Physical Review Letters **125** (2020), 10.1103/physrevlett.125.086802.

[16] P. de Gennes and D. Saint-James, *Elementary excitations in the vicinity of a normal metal-superconducting metal contact,* Physics Letters **4**, 151 (1963).

[17] B. Nijholt and A. R. Akhmerov, *Orbital effect of magnetic field on the majorana phase diagram,* Physical Review B **93** (2016), 10.1103/physrevb.93.235434.

[18] P. P. Paudel, T. Cole, B. D. Woods, and T. D. Stanescu, *Enhanced topological superconductivity in spatially modulated planar josephson junctions,* Physical Review B **104** (2021), 10.1103/physrevb.104.155428.

[19] B. D. Woods and T. D. Stanescu, *Enhanced topological protection in planar quasi-one-dimensional channels with periodically modulated width,* Physical Review B **101** (2020), 10.1103/physrevb.101.195435.

[20] A. Saydjari, A. Pierce, H. Ren, M. Kosowsky, C. Ames, M. Stenho, L. Molenkamp, and A. Yacoby, *Josephson interferometry of zig-zag junctions demonstrating enhanced localization,* Bulletin of the American Physical Society **65** (2020).

[21] F. K. de Vries, Q. Wang, and S. Goswami, Private communications.

[22] F. Rohlfing, G. Tkachov, F. Otto, K. Richter, D. Weiss, G. Borghs, and C. Strunk, *Doppler shift in Andreev reflection from a moving superconducting condensate in Nb/InAs Josephson junctions,* Phys. Rev. B **80**, 220507 (2009).

[23] O. Lesser and Y. Oreg, *Majorana zero modes induced by superconducting phase bias,* Journal of Physics D: Applied Physics **55**, 164001 (2022).

[24] O. Lesser, Y. Oreg, and A. Stern, *One-dimensional topological superconductivity based entirely on phase control,* arXiv preprint arXiv:2206.13537 (2022).

[25] B. van Heck, S. Mi, and A. R. Akhmerov, *Single fermion manipulation via superconducting phase differences in multiterminal josephson junctions,* Phys. Rev. B **90**, 155450 (2014).

[26] T. Schapers and T. Schäpers, *Superconductor/semiconductor junctions,* Vol. 174 (Springer Science & Business Media, 2001).

[27] A. E. G. Mikkelsen, P. Kotetes, P. Krogstrup, and K. Flensberg, *Hybridization at Superconductor-Semiconductor Interfaces,* Phys. Rev. X **8**, 031040 (2018).

[28] S. Schuwalow, N. Schroeter, J. Gukelberger, C. Thomas, V. Strocov, J. Gamble, A. Chikina, M. Caputo, J. Krieger, G. C. Gardner, *et al.*, *Band bending profile and band offset extraction at semiconductor-metal interfaces,* arXiv preprint arXiv:1910.02735 (2019).

[29] J. Shabani, M. Kjærgaard, H. J. Suominen, Y. Kim, F. Nichele, K. Pakrouski, T. Stankevic, R. M. Lutchyn, P. Krogstrup, R. Feidenhans, *et al.*, *Two-dimensional epitaxial superconductor-semiconductor heterostructures: A platform for topological superconducting networks,* Physical Review B **93**, 155402 (2016).

[30] M. Kjærgaard, F. Nichele, H. Suominen, M. Nowak, M. Wimmer, A. Akhmerov, J. Folk, K. Flensberg, J. Shabani, w. C. Palmstrøm, *et al.*, *Quantized conductance doubling and hard gap in a two-dimensional semiconductor–superconductor heterostructure,* Nature communications **7**, 1 (2016).

[31] M. Kjærgaard, H. J. Suominen, M. Nowak, A. Akhmerov, J. Shabani, C. Palmstrøm, F. Nichele, and C. M. Marcus, *Transparent semiconductor-superconductor interface and induced gap in an epitaxial heterostructure josephson junction,* Physical Review Applied **7**, 034029 (2017).

[32] Z. Wan, A. Kazakov, M. J. Manfra, L. N. Pfeiffer, K. W. West, and L. P. Rokhinson, *Induced superconductivity in high-mobility two-dimensional electron gas in gallium arsenide heterostructures,* Nature communications **6**, 1 (2015).

[33] A. Drachmann, H. Suominen, M. Kjaergaard, B. Shojaei, C. Palmstrøm, C. Marcus, and F. Nichele, *Proximity effect transfer from nbti into a semiconductor heterostructure via epitaxial aluminum,* Nano letters **17**, 1200 (2017).

[34] K. Delfanazari, R. K. Puddy, P. Ma, T. Yi, M. Cao, Y. Gul, I. Farrer, D. A. Ritchie, H. J. Joyce, M. J. Kelly, *et al., On-chip andreev devices: Hard superconducting gap and quantum transport in ballistic nb–in0. 75ga0. 25as-quantum-well–nb josephson junctions,* Advanced Materials **29**, 1701836 (2017).

[35] C. T. Ke, C. M. Moehle, F. K. de Vries, C. Thomas, S. Metti, C. R. Guinn, R. Kallaher, M. Lodari, G. Scappucci, T. Wang, R. E. Diaz, G. C. Gardner, M. J. Manfra, and S. Goswami, *Ballistic superconductivity and tunable* π*–junctions in InSb quantum wells,* Nat. Commun. **10**, 1 (2019).

[36] C. M. Moehle, C. T. Ke, Q. Wang, C. Thomas, D. Xiao, S. Karwal, M. Lodari, V. van de Kerkhof, R. Termaat, G. C. Gardner, *et al.*, *Insbas two-dimensional electron gases as a platform for topological superconductivity,* Nano Letters **21**, 9990 (2021).

[37] S. Salimian, M. Carrega, I. Verma, V. Zannier, M. P. Nowak, F. Beltram, L. Sorba, and S. Heun, *Gate-controlled supercurrent in ballistic insb nanoflag josephson junctions,* Applied Physics Letters **119**, 214004 (2021).

[38] J. Zhi, N. Kang, S. Li, D. Fan, F. Su, D. Pan, S. Zhao, J. Zhao, and H. Xu, *Supercurrent and multiple andreev reflections in insb nanosheet sns junctions,* physica status solidi (b) **256**, 1800538 (2019).

[39] A. Fornieri, A. M. Whiticar, F. Setiawan, E. Portolés, A. C. C. Drachmann, A. Keselman, S. Gronin, C. Thomas, T. Wang, R. Kallaher, G. C. Gardner, E. Berg, M. J. Manfra, A. Stern, C. M. Marcus, and F. Nichele, *Evidence of topological superconductivity in planar Josephson junctions,* Nature **569**, 89 (2019).

[40] H. Ren, F. Pientka, S. Hart, A. T. Pierce, M. Kosowsky, L. Lunczer, R. Schlereth, B. Scharf, E. M. Hankiewicz, L. W. Molenkamp, B. I. Halperin, and A. Yacoby, *Topological superconductivity in a phase-controlled Josephson junction,* Nature **569**, 93 (2019).

[41] G. Kells, D. Meidan, and P. Brouwer, *Near-zero-energy end states in topologically trivial spin-orbit coupled superconducting nanowires with a smooth confinement,* Physical Review B **86**, 100503 (2012).

[42] C.-X. Liu, J. D. Sau, T. D. Stanescu, and S. D. Sarma, *Andreev bound states versus majorana bound states in quantum dot-nanowire-superconductor hybrid structures: Trivial versus topological zero-bias conductance peaks,* Physical Review B **96**, 075161 (2017).

[43] C. Moore, C. Zeng, T. D. Stanescu, and S. Tewari, *Quantized zero-bias conductance plateau in semiconductor-superconductor heterostructures without topological majorana zero modes,* Physical Review B **98**, 155314 (2018).

[44] A. Vuik, B. Nijholt, A. Akhmerov, and M. Wimmer, *Reproducing topological properties with quasi-majorana states,* SciPost Physics **7**, 061 (2019).

[45] M. C. Dartiailh, W. Mayer, J. Yuan, K. S. Wickramasinghe, A. Matos-Abiague, I. Žutić, and J. Shabani, *Phase signature of topological transition in josephson junctions,* Physical Review Letters **126**, 036802 (2021).

[46] A. I. Buzdin, *Proximity effects in superconductor-ferromagnet heterostructures,* Rev. Mod. Phys. **77**, 935 (2005).

[47] S. Hart, H. Ren, M. Kosowsky, G. Ben-Shach, P. Leubner, C. Brüne, H. Buhmann, L. W. Molenkamp, B. I. Halperin, and A. Yacoby, *Controlled finite momentum pairing and spatially varying order parameter in proximitized hgte quantum wells,* Nature Physics **13**, 87 (2017).

[48] A. Banerjee, O. Lesser, M. Rahman, H.-R. Wang, M.-R. Li, A. Kringhøj, A. Whiticar, A. Drachmann, C. Thomas, T. Wang, *et al.*, *Signatures of a topological phase transition in a planar josephson junction,* arXiv preprint arXiv:2201.03453 (2022).

[49] A. Banerjee, O. Lesser, M. Rahman, C. Thomas, T. Wang, M. Manfra, E. Berg, Y. Oreg, A. Stern, and C. Marcus, *Local and nonlocal transport spectroscopy in planar josephson junctions,* arXiv preprint arXiv:2205.09419 (2022).

[50] T. Rosdahl, A. Vuik, M. Kjaergaard, and A. Akhmerov, *Andreev rectifier: A nonlocal conductance signature of topological phase transitions,* Physical Review B **97**, 045421 (2018).

[51] R. Hess, H. F. Legg, D. Loss, and J. Klinovaja, *Local and nonlocal quantum transport due to andreev bound states in finite rashba nanowires with superconducting and normal sections,* Phys. Rev. B **104**, 075405 (2021).

[52] F. Nichele, E. Portolés, A. Fornieri, A. M. Whiticar, A. C. Drachmann, S. Gronin, T. Wang, G. Gardner, C. Thomas, A. Hatke, *et al.*, *Relating andreev bound states and supercurrents in hybrid josephson junctions,* Physical Review Letters **124**, 226801 (2020).

[53] A. Stern and E. Berg, *Fractional josephson vortices and braiding of majorana zero modes in planar superconductor-semiconductor heterostructures,* Physical review letters **122**, 107701 (2019).

[54] A. Banerjee, M. Geier, M. A. Rahman, D. S. Sanchez, C. Thomas, T. Wang, M. J. Manfra, K. Flensberg, and C. M. Marcus, *Control of andreev bound states using superconducting phase texture,* arXiv preprint arXiv:2205.15690 (2022).

[55] C. M. Moehle, P. K. Rout, N. A. Jainandunsing, D. Kuiri, C. T. Ke, D. Xiao, C. Thomas, M. J. Manfra, M. P. Nowak, and S. Goswami, *Controlling andreev bound states with the magnetic vector potential,* arXiv preprint arXiv:2207.06933 (2022).

2

SUPERCURRENT-INDUCED MAJORANA BOUND STATES IN A PLANAR GEOMETRY

This chapter has been previously published as André Melo, Sebastian Rubbert, Anton R. Akhmerov, *Supercurrent-induced Majorana bound states in a planar geometry*, SciPost Phys. 7, 039 (2019).

2.1. INTRODUCTION

Majorana bound states (MBS) are a promising avenue for fault tolerant quantum computation due to their topological protection [1–4]. While it is possible to realize MBS in spin liquids [5] or in fractional quantum Hall systems [6, 7], much of the current experimental effort focuses on systems with induced superconductivity and broken time-reversal symmetry [8–10].

One way of breaking time-reversal symmetry is through an exchange interaction with a ferromagnet [11, 12]. However, in such a setup the interaction is not easily tunable. This creates difficulties in distinguishing MBS from trivial low energy states [13], and makes it necessary to carefully optimize the constituent materials. The most commonly used scheme relies on the Zeeman effect created by an external magnetic field in a proximitized semiconducting nanowire [14–21]. This approach requires strong magnetic fields because the electron spin splitting must exceed the induced superconducting gap in the topological phase. An alternative method relies on the orbital effect of the magnetic field in a three-dimensional geometry, however it also requires strong magnetic fields because of the need to thread a flux comparable to a flux quantum through the device cross-section [22–25]. Magnetic fields suppress the superconducting gap and can create Abrikosov vortices, both detrimental to MBS properties.

Supercurrents also break time-reversal symmetry, and can thus be used to lower the minimal magnetic field required for creating MBS [26, 27], or even remove it altogether in hybrid devices combining topological insulators and superconductors [28, 29]. Recent proposals have focused on Josephson junctions formed by a two-dimensional electron gas (2DEGs) proximity-coupled to two superconducting terminals [30, 31]. In these devices the critical magnetic field reduces significantly when the superconducting electrodes have a phase difference. Such Josephson junctions were realized experimentally [32, 33] but a significant critical field reduction is yet to be observed.

Here we propose a setup using a conventional 2DEG and superconducting phase differences to create MBS without an external magnetic field. In order to achieve this, we utilize the idea of Ref. [34], demonstrating that more than two distinct values of superconducting phase are necessary to create a topological phase transition. In particular, we show that applying supercurrents parallel to junction creates a spin splitting that is sufficiently strong to drive a topological phase transition.

2.2. SETUP

We consider a 2DEG with spin-orbit interaction covered by two superconductors forming a Josephson junction. The coupling between the superconductor and the semiconductor is strong and therefore the g-factor and the spin-orbit coupling are suppressed in the covered regions [35]. The superconductors carry supercurrents in opposite directions along the junction (Fig. 3.1). We model this system using an effective 2-dimensional Hamiltonian combining parabolic dispersion and Rashba spin-orbit interaction:

$$H = \left(\frac{p_x^2 + p_y^2}{2m} - \mu\right)\sigma_0\tau_z + \xi(y)\alpha(p_x\sigma_y - p_y\sigma_x)\tau_z + \mathrm{Re}\Delta(x, y)\sigma_0\tau_x + \mathrm{Im}\Delta(x, y)\sigma_0\tau_y, \quad (2.1)$$

where $p_{x,y} = -i\hbar\partial_{x,y}$, m is the effective electron mass, μ the chemical potential, α the Rashba spin-orbit interaction strength and $\Delta(x, y)$ the superconducting gap. The indicator function $\xi(y) = 0$ under the superconductor and $\xi(y) = 1$ otherwise. Finally, σ_i and τ_i are the Pauli matrices in the spin and the electron-hole space. This Hamiltonian has a particle-hole symmetry $\mathscr{P} = \tau_y\sigma_y K$, with K complex conjugation. Because the superconductors carry a supercurrent, their phase depends linearly on x:

$$\Delta(x,y) = \begin{cases} \Delta_0 \exp(2\pi i x/\lambda_T) & W/2 < y < W/2 + L_{\mathrm{sc}}, \\ 0 & |y| < W/2, \\ \Delta_0 \exp(-2\pi i x/\lambda_B) & -W/2 - L_{\mathrm{sc}} < y < -W/2, \end{cases} \tag{2.2}$$

with W the width of the Josephson junction, λ_T and λ_B the winding lengths of the superconducting phase in the two superconductors, and Δ_0 the magnitude of the induced superconducting gap. Making the superconducting phase depend only y coordinate coordinate is insufficient, because at $k_x = 0$ the spin-orbit coupling may be removed by a transformation $\psi(y) \to \exp[i\sigma_x f(y)]\psi(y)$, and therefore all states are doubly degenerate. This degeneracy was overlooked in Ref. [22] when analyzing the effective two-dimensional Hamiltonian of the semiconducting slab.

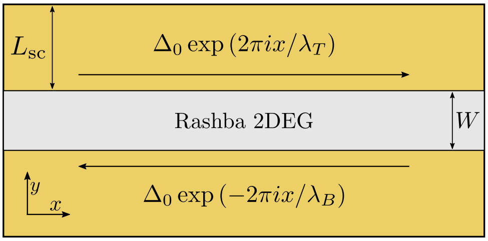

Figure 2.1: A 2DEG with Rasba spin-orbit coupling covered by two conventional superconductors. The superconductors carry longitudinal supercurrents in opposite directions, indicated by the horizontal arrows.

To characterize the topological properties of the setup we apply the finite difference approximation to the continuum Hamiltonian Eq. (5.3) with a lattice constant $a = 10\,\mathrm{nm}$, and numerically study the resulting tight-binding Hamiltonian using the Kwant software package [36]. We use the implementation of Ref. [37] as a starting point. Whenever necessary we use Adaptive [38] to efficiently sample the parameter space. The source code and data used to produce the figures in this work are available in Ref. [39].

2.3. CREATING A TOPOLOGICAL PHASE

We illustrate the appearance of the topological phase by introducing the necessary ingredients one by one. The resulting band structures are computed through sparse diagonalization of the Hamiltonian for several values of the Bloch wave vector κ corresponding to the supercell of the device. We choose the following parameter values, unless specified otherwise. The effective electron mass is $m = 0.04 m_e$, with m_e the free electron mass, $\lambda_T = \lambda_B = \lambda = 370\,\mathrm{nm}$, $\Delta_0 = 1\,\mathrm{meV}$, $\alpha = 10\,\mathrm{meV\,nm}$, as well as the geometrical parameters $L_{\mathrm{sc}} = 200\,\mathrm{nm}$, $W = 150\,\mathrm{nm}$.

2.3.1. PHASE WINDING AND INVERSION SYMMETRY

We observe that the band structure in presence of phase winding has a spin splitting at $\kappa = 0$, as shown in Fig. 2.2. The level crossing at $\kappa = 0$ may be protected only by the Kramers degeneracy appearing when H commutes with an antiunitary operator squaring to -1. In absence of winding, this condition is fulfilled by the time-reversal symmetry $\mathscr{T} = \sigma_y K$. We identify that even in presence of winding, the Hamiltonian commutes with the operator $\delta(y + y')\mathscr{T}$, except for the transverse spin-orbit coupling $\alpha p_y \sigma_x$. Therefore the avoided crossing is produced by a combination of the winding and of the transverse spin-orbit coupling breaking all the remaining time-reversal-like symmetries of the system. In Fig. 2.2 we also demonstrate that removing the transverse spin-orbit coupling restores the degeneracy of levels at $\kappa = 0$. We conclude that the width W of the normal region must be comparable to the spin-orbit length $l_{\text{so}} = \hbar / m\alpha$ in order for the transverse spin-orbit to have a sufficient impact and to cause a spin splitting. The level crossings at $\kappa = \pi$ stay protected by a nonsymmorphic antiunitary symmetry with an operator $\tau_z \delta(y + y')\delta(x - x' + \lambda/2)K$.

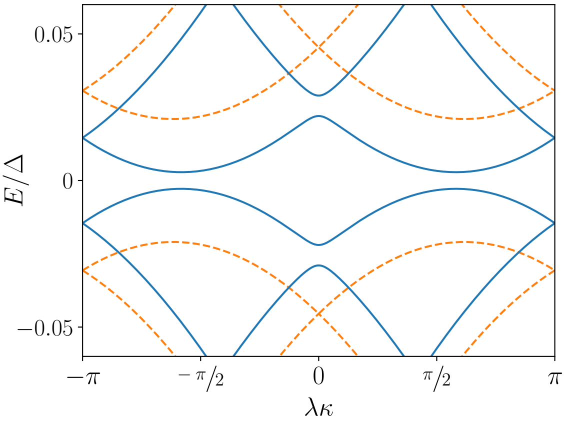

Figure 2.2: Band structures of systems with spin-orbit interaction at $\mu = 0.17\,\text{meV}$. The avoided level crossings at $\kappa = 0$ are a consequence of an effective Zeeman interaction originating from the combination of the spin-orbit coupling and the supercurrents carried by the superconductors. Removing transverse spin-orbit coupling restores Kramer's degeneracy at $\kappa = 0$ and results in the band structure plotted with dashed lines.

Furthermore, we see that the spectrum is reflection symmetric about $\kappa = 0$. This is a consequence of the inversion symmetry of the Hamiltonian $[H, I] = 0$, with the inversion symmetry operator $I = \delta(x + x')\delta(y + y')\sigma_z$. Since choosing $\lambda_T \neq \lambda_B$ breaks the inversion symmetry, it may close the band gap at finite momentum, as illustrated in Fig. 2.3, where we chose $\lambda_T = 2\lambda_B = 700\,\text{nm}$ and $\mu = 0.42\,\text{meV}$. Preserving inversion symmetry therefore maximizes the parameter range supporting gapped spectra.

2.3.2. BREAKING THE CHARGE-MOMENTUM CONSERVATION LAW

The band structure in Fig. 2.2 resembles that of a proximitized nanowire with spin-orbit interaction and Zeeman field [14, 15]. By analogy it is then natural to expect that tuning the chemical potential such that the two spin states at $\kappa = 0$ have opposite energies should

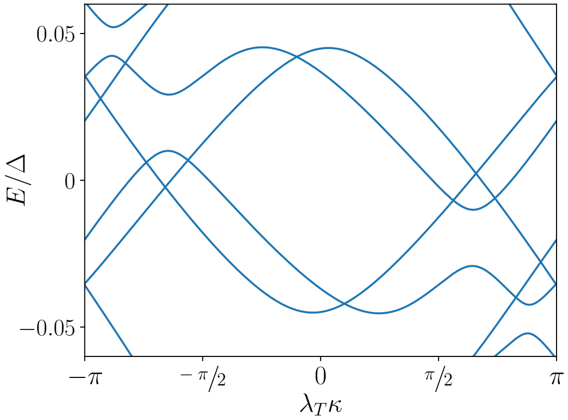

Figure 2.3: Gapless band structure due to broken inversion symmetry resulting from different supercurrent densities ($\lambda_T = 2\lambda_B$).

result in a topologically nontrivial band structure. Instead we observe a gapless band structure with band gap closings at finite κ, as shown in Fig. 2.4(a).

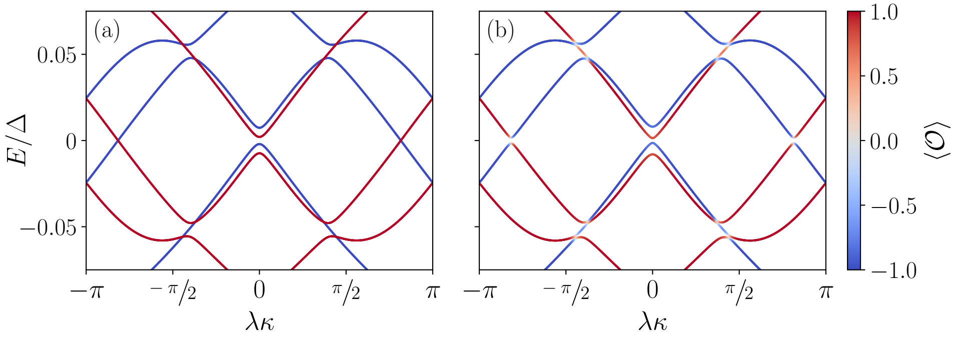

Figure 2.4: Band structures of the system with the Fermi level tuned inside the avoided crossing at $\kappa = 0$ with (a) a zero band gap due to charge-momentum parity conservation, and (b) finite band gap due to a periodic potential. The bands are colored according to the expectation value of $\mathcal{O}$.

The crossings in the spectrum are protected because every Andreev reflection in this setup is accompanied by a wave vector change of $\pm 2\pi/\lambda$. Therefore the Hamiltonian conserves the charge-momentum parity

$$\mathcal{O} = (-1)^n \tau_z, \quad [H, \mathcal{O}] = 0. \tag{2.3}$$

Here $n \equiv \lambda(k_x - \kappa)/2\pi$ is the number of the unit cell in reciprocal space. We visualize this conservation law in Fig. 2.5. Because $\{\mathcal{P}, \mathcal{O}\} = 0$, each eigenstate $|\Psi\rangle$ of the Hamiltonian with energy E, Bloch wave vector κ, and charge-momentum parity $\mathcal{O}$ has a partner $\mathcal{P}|\Psi\rangle$ with $-E$, $-\kappa$, and $-\mathcal{O}$. Topological phase transitions occur whenever such a pair of states crosses zero energy at $\kappa = 0$ or $\kappa = \pi$. As a consequence, in the topological regime the difference of the number of states with positive E and $\mathcal{O}$ at $\kappa = 0$ and those at $\kappa = \pi$ is odd. Therefore the topological phase requires at least one band with positive $\mathcal{O}$ (and its particle-hole symmetric partner with negative $\mathcal{O}$) to cross zero energy between $\kappa = 0$ and $\kappa = \pi$. This prohibits a gapped topological phase as long as $\mathcal{O}$ is conserved.

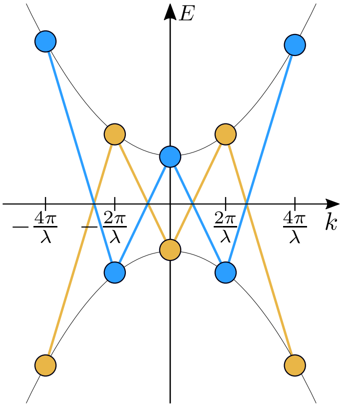

Figure 2.5: Schematic normal state band structure of the Hamiltonian of Eq. (5.3). For illustration purposes we neglect the spin-orbit coupling. The dots represent momentum eigenstates with Bloch momentum $\kappa = 0$ and the lines denote couplings introduced by the superconductors. The colors correspond to different eigenvalues of the charge-momentum parity.

Since a gap is necessary for topologically protected MBS, we consider the following strategies for breaking the charge-momentum parity conservation:

- adding a periodic potential

  $$\delta V = V \cos(2\pi x/\lambda_V)\sigma_0\tau_z, \tag{2.4}$$

  with V the amplitude of the potential and λ_V its periodicity;

- adding an extra superconductor in the middle, as sketched in Fig. 2.6 (a), so that $\Delta(x,y)$ becomes:

  $$\Delta(x,y) = \begin{cases} \Delta_0 \exp(-2\pi i x/\lambda) & y > W/2, \\ \Delta' & w/2 > |y|, \\ 0 & w/2 < |y| < W/2, \\ \Delta_0 \exp(2\pi i x/\lambda) & y < -W/2, \end{cases} \tag{2.5}$$

  where w is the width of the middle superconductor and Δ' its superconducting gap;

- adding a zigzag modulation to the junction shape [40] with period z_x and amplitude z_y, as depicted in Fig. 2.6(b).

These modifications couple the eigensubpaces of $\mathcal{O}$ as shown in Fig. 2.7 and open a gap in the topological regime. We verify that this is the case by adding a periodic potential with $V = 0.005\,\mathrm{meV}$ and $\lambda_V = \lambda$, which results in a gapped topologically-nontrivial band structure shown in Fig. 2.4(b).

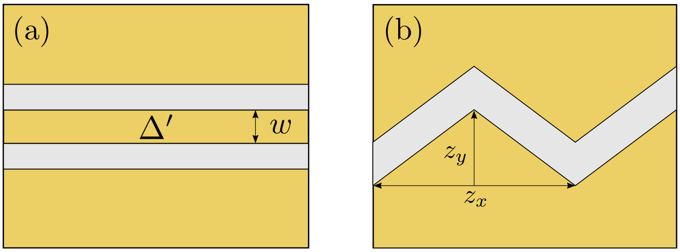

Figure 2.6: Schematics of systems with broken charge-momentum parity symmetry due to (a) a third superconductor carrying no supercurrent, and (b) a zigzag-shaped junction.

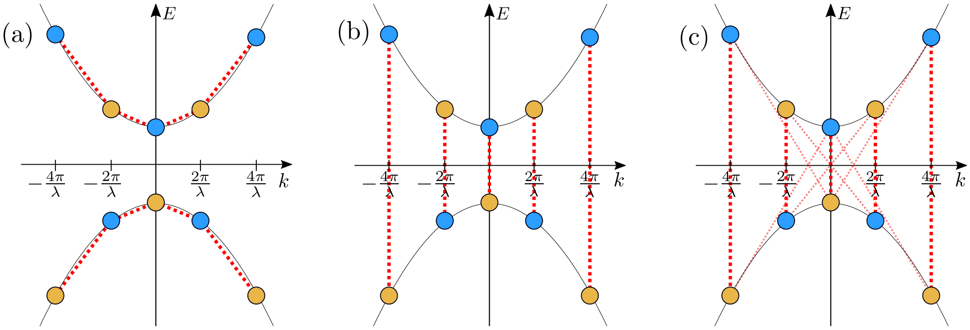

Figure 2.7: Schematic band structure of the Hamiltonian of Eq. (5.3) with charge-momentum parity breaking terms. The red dashed lines denote the symmetry breaking couplings introduced by (a) a periodic potential, and (b) a third superconductor, and (c) zigzag-shaped junction. By projecting the zigzag junction Hamiltonian onto a plane wave basis we have verified that it introduces couplings to higher harmonics [39] which we denote with narrower transparent lines.

2.4. PHASE DIAGRAMS

In order to check how robust the resulting topological superconductivity is, we study the topological phase diagrams of the three candidate systems as a function of λ and μ, focusing especially on the effect of winding of the superconducting phase becoming incommensurate with the other periods appearing in the Hamiltonian: λ_V and z_x. For illustration purposes we choose the parameters $\alpha = 20\,\mathrm{meV\,nm}$, $z_x = 515\,\mathrm{nm}$, $z_y = 37.5\,\mathrm{nm}$, $V = 0.15\,\mathrm{meV}$, $\lambda_V = 515\,\mathrm{nm}$, $\Delta' = \Delta_0 = 1\,\mathrm{meV}$ and $w = 10\,\mathrm{nm}$. Because our goal is a qualitative exploration of the topological phase diagram we neglect the impact of the zigzag shape on the phase winding pattern. This is also a good approximation because the zigzag modulation is small ($z_x \sim 10 \times z_y$). We utilize the scattering formalism to construct the topological phase diagram when the winding length λ of the superconducting phase is incommensurate with the periodicity of the potential λ_V or the period of the zigzag modulation z_x. Specifically, we construct a finite but large system with length $L_x = 10.3\,\mu\mathrm{m} = 20 z_x$ with two normal leads attached, shown in Fig. 2.8(a). We then compute the scattering matrix as a function of energy and compute the topological invariant $\mathcal{Q} = \operatorname{sign}\det r$, where r is the reflection block of the scattering matrix [41]. We estimate the gap as the lowest energy at which the total transmission between two leads $T_{12} = 1/2$,

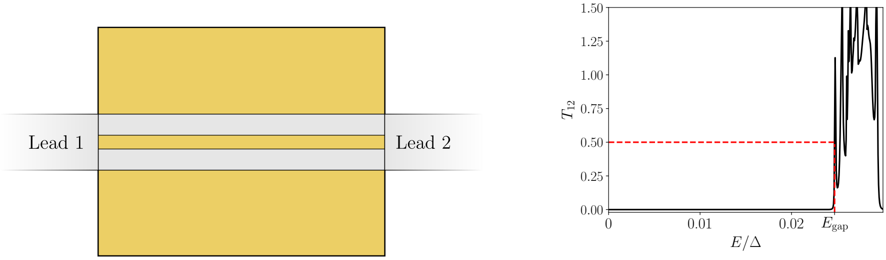

(a) (b)

Figure 2.8: To compute the band gap we (a) attach two two normal leads to the system and (b) compute the transmission between the leads; we then approximate the gap to be the energy at which transmission exceeds 0.5.

as illustrated in Fig. 2.8(b).

Because adding a third superconductor preserves inversion symmetry regardless of λ, the phase diagram of the system with 3 superconductors is gapped except for phase transitions. In contrast, the periodic potential and zigzag systems are only inversion symmetric when the periods of different Hamiltonian terms are equal, that is when $\lambda = \lambda_V$ and $\lambda = z_x$. Once parameters become incommensurate the gap closes quickly and the diagrams have large gapless regions. However, the topological phase of the system zigzag geometry is significantly more robust to incommensurate parameters than that of the periodic potential and tolerates variations of λ of approximately 10%. We also observe that the zigzag geometry is sufficiently robust to support a gapped topological phase with only one superconductor, see App. 2.A.

The shape of the topological regions has a complex dependence on μ and λ that does not seem amenable to analytical treatment. Additionally, the topological gap is smaller than the full superconducting gap by approximately a factor of 50, likely due to a suboptimal choice of parameters, rather than a fundamental limitation of the setups.

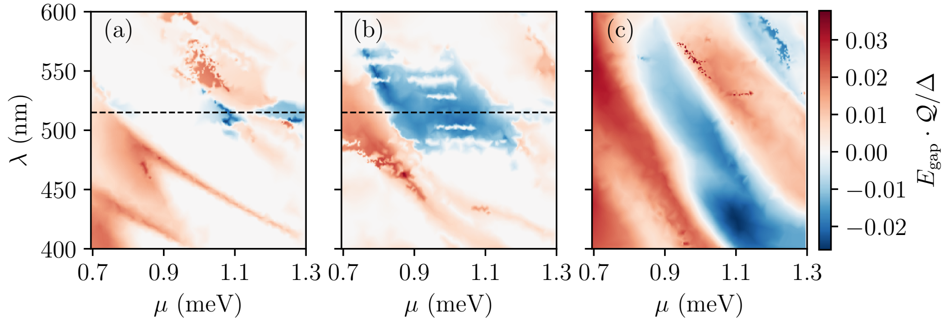

Figure 2.9: Phase diagrams for systems with (a) a periodic potential, (b) a zigzag-shaped junction, and (c) a third superconductor carrying no supercurrent. The dashed line indicate the region where the systems have commensurate parameters, that is $\lambda = \lambda_V$, and $\lambda = z_x$. Negative values correspond to topologically non-trivial systems.

2.5. SUMMARY

In summary, we have shown that the winding of a superconducting phase is a sufficient source of time-reversal symmetry breaking to create MBS in Josephson junctions. By performing symmetry analysis we have identified the breaking of the charge-momentum parity conservation law as the key ingredient for tuning the system into a gapped topological regime. Furthermore, we showed that preserving inversion symmetry maximizes the size of the parameter regions supporting gapped spectra.

The only magnetic field in the system is caused by the supercurrents in the electrodes. To estimate the magnitude of the magnetic field we approximate the supercurrents and the resulting magnetic field through the relations $I = hdW/(\lambda_L^2\mu_0 2e\lambda)$ and $B = \frac{\mu_0 I}{2\pi W}$, where d is the thickness of the superconductor, λ_L the London penetration depth, and μ_0 the vacuum permeability. Using experimentally realistic values of $d = 10\,\mathrm{nm}$, $\lambda_L = 200\,\mathrm{nm}$ (niobium) and $\lambda = 250\,\mathrm{nm}$ yields $\sim 0.3\,\mathrm{mA}$ and $B \sim 0.2\,\mathrm{mT}$, which is negligible in a mesoscopic superconductor.

The periodic potential scheme is the most challenging to implement experimentally, since it requires patterning a large number of gates. Additionally this scheme requires almost exactly commensurate λ and λ_V. Adding a third superconductor has the advantage of preserving inversion symmetry regardless of the phase winding length λ. On the other hand it is sensitive to the geometry: the width of the middle strip w must be large enough to allow Andreev reflections, but shorter than the superconducting coherence length in order to allow transmission between the top and bottom superconductors. The zigzag-shaped junction has a larger tolerance to incommensurate parameters compared to the periodic potential and is less sensitive to the details of the geometry than the third superconductor. Furthermore, it can be be fabricated with current techniques [42], making it the most promising scheme.

We have excluded the effects of disorder and aperiodic variations in the geometry or the electrostatic environment of the device. Such perturbations destroy translation symmetry and couple states with different Bloch momenta, thus also breaking the charge-momentum parity, and potentially offering a simpler approach to creating a topological phase. Another direction of further research would is to identify the system geometry and parameters maximizing the topological gap of the systems.

2.A. SYSTEM WITH A SINGLE ZIGZAG-SHAPED SUPERCONDUCTOR

A system with a single zigzag-shaped superconducting contact, as shown in Fig. 2.10, may still support a topological phase despite having strongly broken inversion symmetry. In Fig. 2.11 we show a phase diagram for such a system with $z_x = 360\,\mathrm{nm}$, $z_y = 75\,\mathrm{nm}$, and $L_x = 7.2\,\mu\mathrm{m} = 20z_x$.

REFERENCES

[1] A. Y. Kitaev, *6. Quantum computing: Unpaired Majorana fermions in quantum wires,* Physics Uspekhi **44**, 131 (2001).

[2] A. Stern, *Non-Abelian states of matter,* Nature **464**, 187 (2010).

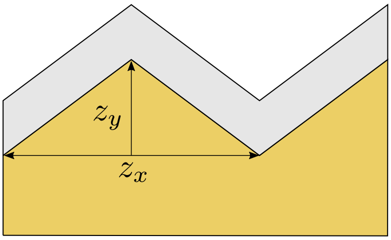

Figure 2.10: Schematic of a system with a single zigzag-shaped superconductor.

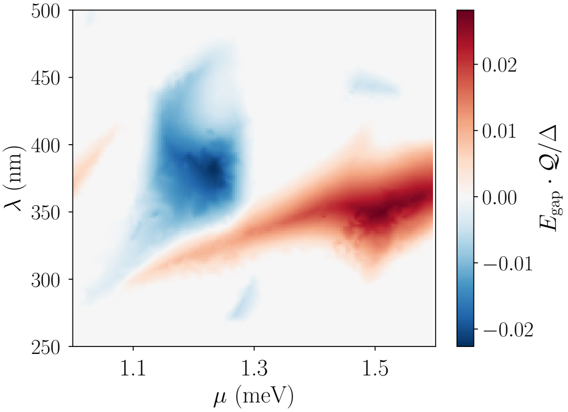

Figure 2.11: Phase diagram of a system with a single superconductor in a zigzag shape.

[3] R. F. Service, *Search for Majorana fermions nearing success at last?* Science **332**, 193 (2011).

[4] F. Wilczek, *Majorana returns,* Nat. Phys. **5**, 614 (2009).

[5] H. Bombin, *Topological order with a twist: Ising anyons from an Abelian model,* Phys. Rev. Lett. **105**, 030403 (2010).

[6] N. Read and G. Moore, *Fractional quantum Hall effect and nonabelian statistics,* Progr. Theor. Phys. Supp. **107**, 157 (1992).

[7] C. Nayak, S. H. Simon, A. Stern, M. Freedman, and S. Das Sarma, *Non-Abelian anyons and topological quantum computation,* Rev. Mod. Phys. **80**, 1083 (2008).

[8] J. Alicea, *New directions in the pursuit of Majorana fermions in solid state systems,* Rep. Prog. Phys. **75**, 076501 (2012).

[9] M. Leijnse and K. Flensberg, *Introduction to topological superconductivity and Majorana fermions,* Semiconductor Science and Technology **27**, 124003 (2012).

[10] C. W. J. Beenakker, *Search for Majorana fermions in superconductors,* Annual Review of Condensed Matter Physics **4**, 113 (2013).

[11] T.-P. Choy, J. M. Edge, A. R. Akhmerov, and C. W. J. Beenakker, *Majorana fermions emerging from magnetic nanoparticles on a superconductor without spin-orbit coupling,* Phys. Rev. B **84**, 195442 (2011).

[12] J. Li, T. Neupert, B. A. Bernevig, and A. Yazdani, *Manipulating Majorana zero modes on atomic rings with an external magnetic field,* Nature Communications **7**, 10395 (2016).

[13] M. Ruby, B. W. Heinrich, Y. Peng, F. von Oppen, and K. J. Franke, *Exploring a proximity-coupled Co chain on Pb(110) as a possible Majorana platform,* Nano Lett. **17**, 4473 (2017).

[14] R. M. Lutchyn, J. D. Sau, and S. Das Sarma, *Majorana fermions and a topological phase transition in semiconductor-superconductor heterostructures,* Phys. Rev. Lett. **105**, 077001 (2010).

[15] Y. Oreg, G. Refael, and F. von Oppen, *Helical liquids and Majorana bound states in quantum wires,* Phys. Rev. Lett. **105**, 177002 (2010).

[16] V. Mourik, K. Zuo, S. M. Frolov, S. R. Plissard, E. P. A. M. Bakkers, and L. P. Kouwenhoven, *Signatures of Majorana fermions in hybrid superconductor-semiconductor nanowire devices,* Science **336**, 1003 (2012).

[17] A. Das, Y. Ronen, Y. Most, Y. Oreg, M. Heiblum, and H. Shtrikman, *Zero-bias peaks and splitting in an Al-InAs nanowire topological superconductor as a signature of Majorana fermions,* Nat. Phys. **8**, 887 (2012).

[18] M. T. Deng, C. L. Yu, G. Y. Huang, M. Larsson, P. Caroff, and H. Q. Xu, *Anomalous zero-bias conductance peak in a Nb–InSb nanowire–Nb hybrid device,* Nano Lett. **12**, 6414 (2012).

[19] A. D. K. Finck, D. J. Van Harlingen, P. K. Mohseni, K. Jung, and X. Li, *Anomalous modulation of a zero-bias peak in a hybrid nanowire-superconductor device,* Phys. Rev. Lett. **110**, 126406 (2013).

[20] S. M. Albrecht, A. P. Higginbotham, M. Madsen, F. Kuemmeth, T. S. Jespersen, J. Nygård, P. Krogstrup, and C. M. Marcus, *Exponential protection of zero modes in Majorana islands,* Nature (London) **531**, 206 (2016).

[21] O. Gül, H. Zhang, J. D. S. Bommer, M. W. A. de Moor, D. Car, S. R. Plissard, E. P. A. M. Bakkers, A. Geresdi, K. Watanabe, T. Taniguchi, and et al., *Ballistic Majorana nanowire devices,* Nature Nanotechnology **13**, 192–197 (2018).

[22] P. Kotetes, *Topological superconductivity in Rashba semiconductors without a Zeeman field,* Physical Review B **92** (2015), 10.1103/physrevb.92.014514.

[23] S. Vaitiekėnas, M.-T. Deng, P. Krogstrup, and C. Marcus, *Flux-induced Majorana modes in full-shell nanowires,* arXiv preprint arXiv:1809.05513 (2018), arXiv:1809.05513.

[24] R. M. Lutchyn, G. W. Winkler, B. Van Heck, T. Karzig, K. Flensberg, L. I. Glazman, and C. Nayak, *Topological superconductivity in full shell proximitized nanowires,* arXiv preprint arXiv:1809.05512 (2018), arXiv:1809.05512.

[25] B. D. Woods, S. Das Sarma, and T. D. Stanescu, *Electronic structure of full-shell InAs/Al hybrid semiconductor-superconductor nanowires: Spin-orbit coupling and topological phase space,* Physical Review B **99** (2019), 10.1103/physrevb.99.161118.

[26] A. Romito, J. Alicea, G. Refael, and F. von Oppen, *Manipulating Majorana fermions using supercurrents,* Phys. Rev. B **85**, 020502 (2012).

[27] O. Dmytruk, M. Thakurathi, D. Loss, and J. Klinovaja, *Majorana Bound States in Double Nanowires with Reduced Zeeman Thresholds due to Supercurrents,* arXiv preprint arXiv:1902.11232 (2019), arXiv:1902.11232.

[28] L. Fu and C. L. Kane, *Superconducting proximity effect and Majorana fermions at the surface of a topological insulator,* Phys. Rev. Lett. **100**, 096407 (2008).

[29] A. Cook and M. Franz, *Majorana fermions in a topological-insulator nanowire proximity-coupled to an s-wave superconductor,* Phys. Rev. B **84**, 201105 (2011).

[30] F. Pientka, A. Keselman, E. Berg, A. Yacoby, A. Stern, and B. I. Halperin, *Topological superconductivity in a planar Josephson junction,* Phys. Rev. X **7**, 021032 (2017).

[31] M. Hell, M. Leijnse, and K. Flensberg, *Two-dimensional platform for networks of Majorana bound states,* Phys. Rev. Lett. **118**, 107701 (2017).

[32] A. Fornieri, A. M. Whiticar, F. Setiawan, E. Portolés, A. C. C. Drachmann, A. Keselman, S. Gronin, C. Thomas, T. Wang, R. Kallaher, and et al., *Evidence of topological superconductivity in planar Josephson junctions,* Nature (2019), 10.1038/s41586-019-1068-8.

[33] H. Ren, F. Pientka, S. Hart, A. T. Pierce, M. Kosowsky, L. Lunczer, R. Schlereth, B. Scharf, E. M. Hankiewicz, L. W. Molenkamp, and et al., *Topological superconductivity in a phase-controlled Josephson junction,* Nature (2019), 10.1038/s41586-019-1148-9.

[34] B. van Heck, S. Mi, and A. R. Akhmerov, *Single fermion manipulation via superconducting phase differences in multiterminal Josephson junctions,* Phys. Rev. B **90**, 155450 (2014).

[35] W. S. Cole, S. D. Sarma, and T. D. Stanescu, *Effects of large induced superconducting gap on semiconductor Majorana nanowires,* **92** (2015), 10.1103/physrevb.92.174511.

[36] C. W. Groth, M. Wimmer, A. R. Akhmerov, and X. Waintal, *Kwant: a software package for quantum transport,* New J. Phys. **16**, 063065 (2014).

[37] T. Laeven, B. Nijholt, A. R. Akhmerov, and M. Wimmer, *Enhanced proximity effect in zigzag-shaped Majorana Josephson junctions,* (2019).

[38] B. Nijholt, J. Weston, J. Hoofwijk, and A. Akhmerov, *python-adaptive/adaptive: version 0.7.3,* Software on Zenodo (2019), tools for the adaptive and parallel sampling of mathematical functions, available at `http://dx.doi.org/10.5281/zenodo.1182437`.

[39] A. Melo, S. Rubbert, and A. R. Akhmerov, *Supercurrent-induced Majorana bound states in a planar geometry,* Dataset on Zenodo (2019).

[40] T. Laeven, B. Nijholt, M. Wimmer, and A. R. Akhmerov, *Enhanced proximity effect in zigzag-shaped Majorana Josephson junctions,* (2019), arXiv:1903.06168.

[41] A. R. Akhmerov, J. P. Dahlhaus, F. Hassler, M. Wimmer, and C. W. J. Beenakker, *Quantized Conductance at the Majorana Phase Transition in a Disordered Superconducting Wire,* Phys. Rev. Lett. **106** (2011), 10.1103/physrevlett.106.057001.

[42] F. K. de Vries, Q. Wang, and S. Goswami, Private communications.

3

GREEDY OPTIMIZATION OF MAJORANA JOSEPHSON JUNCTION

This chapter has been previously published as André Melo, Tanko Tanev, Anton R. Akhmerov, *Greedy optimization of the geometry of Majorana Josephson junctions* , arXiv:2205.05689.

3.1. INTRODUCTION

Majorana bound states (MBS) are topologically protected edge states with non-abelian statistics that can serve as a building block for fault tolerant quantum computers [1–4]. While much of the experimental search for topological superconductivity has focused on proximitized semiconducting nanowires [5–8], this system requires applying a sufficiently strong magnetic field to drive a topological phase transition. Because magnetic fields suppress superconductivity, the field compatibility of Majorana devices is an open problem. An alternative proposal—Josephson junctions in a two-dimensional electron gas (2DEG) with spin-orbit coupling [9–13]—uses the phase difference across the junction to lower the critical magnetic field.

The topological protection of MBS requires a spectral gap. Therefore, designing devices with sufficiently large gaps is a necessary component of engineering Majorana states. In Majorana Josephson junctions, the gap is limited by long trajectories in the normal region that do not come into contact with the superconducting terminals [14, 15]. Eliminating these long-flight trajectories by making the junction zigzag-shaped leads to an order of magnitude increase in the topological gap [15]. The topological gap is also enhanced in other periodically modulated geometries [16, 17].

Optimizing a band gap is similarly relevant to photonic and acoustic crystals to design devices such as filters, beam splitters, and waveguides [18]. A large body of research shows that numerical optimization methods such as genetic algorithms [19, 20], semidefinite programming [21, 22], and gradient-based strategies [23, 24] find geometries with large band gaps despite performing a search in an exponentially large design space. More recent work demonstrated that deep learning accelerates optimization by predicting effective tight-binding models corresponding to microscopic geometries [25]. In the context of one-dimensional Majorana nanowires, Boutine et al. [26] and Turcotte et al [27] used an algorithm based on GRAPE [28] to minimize the Majorana localization length through spatially varying electrostatic potentials and magnetic field textures.

While geometry was demonstrated to have a sizeable effect on the topological gap of Majorana junctions, the question of how to find optimal geometries remains open. Inspired by the previous works in numerical geometry optimization, we develop the following greedy algorithm to find optimal Majorana junction geometries. At each optimization step, we compute a set of possible deformations to the shape of the superconducting regions. Using perturbation theory we estimate how the gap changes with these deformations and select the one that yields the largest improvement. We avoid overfitting geometries to specific parameters by randomly varying the operating point throughout the optimization, similarly to stochastic gradient descent. To ensure that the resulting geometries are within reach of fabrication techniques, we incorporate smoothness and minimum feature size constraints. We benchmark our algorithm on a variety of physical scenarios and find that it reliably produces geometries with increased topological gaps over large system parameter ranges. Finally, we check the robustness of the algorithm and discuss its potential generalizations.

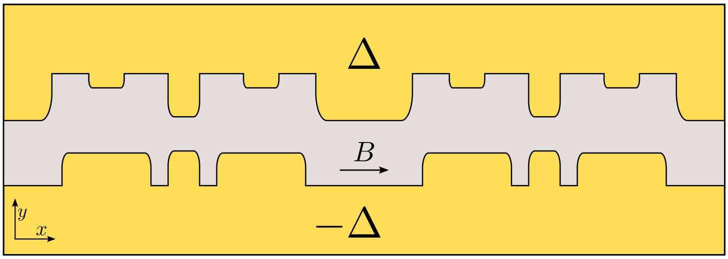

Figure 3.1: Schematic representation of two unit cells of a topological Josephson junction formed by covering a Rashba 2DEG with s-wave superconductors. An applied magnetic field penetrates the normal region (grey) and breaks time-reversal symmetry. The proximitized regions (yellow) experience an additional proximity-induced pairing term and a superconducting phase difference of π.

3.2. MODEL AND ALGORITHM DESCRIPTION

We consider a Josephson junction formed by proximitizing a Rashba 2DEG with two s-wave superconductors (Fig. 3.1). We model the central normal region with a two-dimensional Bogoliubov-de Gennes Hamiltonian

$$H_\mathrm{N} = \left(\frac{\hbar^2}{2m}(k_x^2 + k_y^2) - \mu + \alpha(k_y\sigma_x - k_x\sigma_y)\right)\tau_z + E_Z\sigma_x,$$

where α and E_Z parameterize the strength of the Rashba spin-orbit and Zeeman fields respectively, μ is the chemical potential, and σ_i and τ_i are the Pauli matrices acting in spin and electron-hole space. Following previous works [9, 10] we fix the superconducting phase difference to its optimal value $\phi = \pi$. This choice also simplifies the geometry optimization problem because it guarantees that the system never leaves the topological regime. The Hamiltonian of the proximitized regions then has an additional coupling term

$$H_\mathrm{SC} = \Delta(x, y)\tau_x$$

where $\Delta(x, y) = \Delta_0$—the induced superconducting gap—in the top superconductor and $-\Delta_0$ in the bottom superconductor. Because we are interested in determining bulk properties, we consider a translationally invariant system with a supercell Hamiltonian $H = H_\mathrm{N} + H_\mathrm{S}$, which we discretize using the Kwant software package [29]. Unless stated otherwise, we consider a unit cell of length $L_x = 1300\,\mathrm{nm}$, lattice constant of $a = 20\,\mathrm{nm}$, and Hamiltonian parameters $m = 0.02m_e$ (with m_e the free electron mass), $\alpha = 20\,\mathrm{meV\,nm}$ and $\Delta_0 = 1\,\mathrm{meV}$.

Our core iterative algorithm starts by computing the band structure of the initial geometry on a sufficiently fine grid of the supercell momenta κ_x using sparse diagonalization. Since we are interested in low-energy behavior, we compute only a small set of the $2n_b = 8$ bands closest to the Fermi level. We then compute a set of candidate perturbations to the geometry of the junction. Using conventional image processing we determine the normal-superconductor boundary and then consider two types of modifications: removing superconductivity from boundary sites, and introducing superconductivity in normal sites immediately next to the boundary (Fig. 3.2(b)). Limiting the geometry perturbations

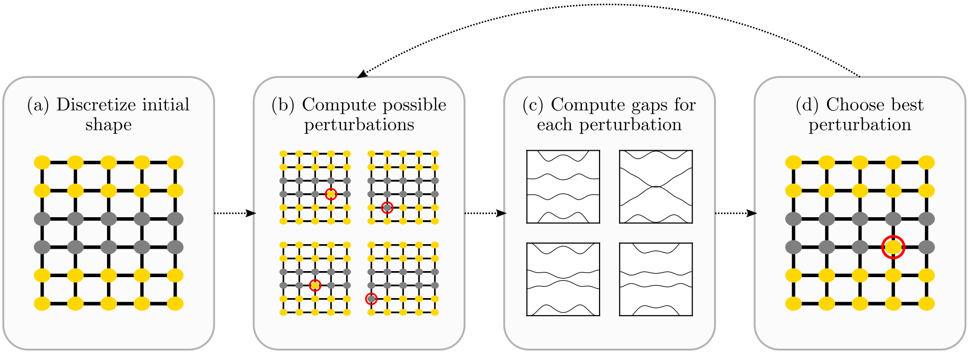

Figure 3.2: Summary of the core optimization algorithm. (a) We start from a discretized model of the junction. (b) At the start of an iteration we determine the boundaries of each superconductor. We then consider perturbations that introduce or remove superconductivity in sites at the boundary (circled in red). (c) Using perturbation theory, we compute how the gap changes with each geometry modification. (d) Finally, we update the shape using the modification that yields the largest improvement in the gap.

to the boundaries of the superconductors with the normal regions promotes the continuity of the shape evolution. In order to implement fabrication constraints, we reject perturbations where the minimum distance between superconductors is lower than a specified tolerance $w = 100\,\mathrm{nm}$. Once we have collected a set of perturbations, we use first order degenerate perturbation theory to estimate how they change the dispersion relation (Fig. 3.2(c)). Finally, we modify the superconductors' shape with the perturbation that yields the largest improvement in the gap and proceed to another iteration (Fig. 3.2(d)). Because calculations of Bloch eigenstates at different κ_x as well as computing the effect of different perturbations are independent, the algorithm is embarrassingly parallel. We leverage this by using the dask software package [30] to parallelize our implementation.

Although the core algorithm is already capable of finding improved geometries, it has the following limitations:

- It is inefficient to fully recompute the dispersion relation after each iteration.
- Due to being greedy, the algorithm gets stuck in any local maximum.
- The resulting shapes tend to be irregular and contain features that vary on the scale of the lattice constant.

We solve these problems by introducing epochs consisting of a handful of iterations each. Instead of exactly recomputing the dispersion relation at each iteration, we do it only at the beginning of an epoch. Furthermore, at every epoch we select random values of $E_{Z1} < E_Z < E_{Z2}$ and $\mu_1 < \mu < \mu_2$. This procedure is analogous to performing stochastic gradient descent to optimize the average gap over a region in parameter space, and it ensures that the optimized geometries are tolerant to variations in the junction Hamiltonian. Finally, we apply a median filter to the superconductor shapes every few epochs, which constrains the optimizer to explore shapes that vary smoothly in space.

3.3. RESULTS

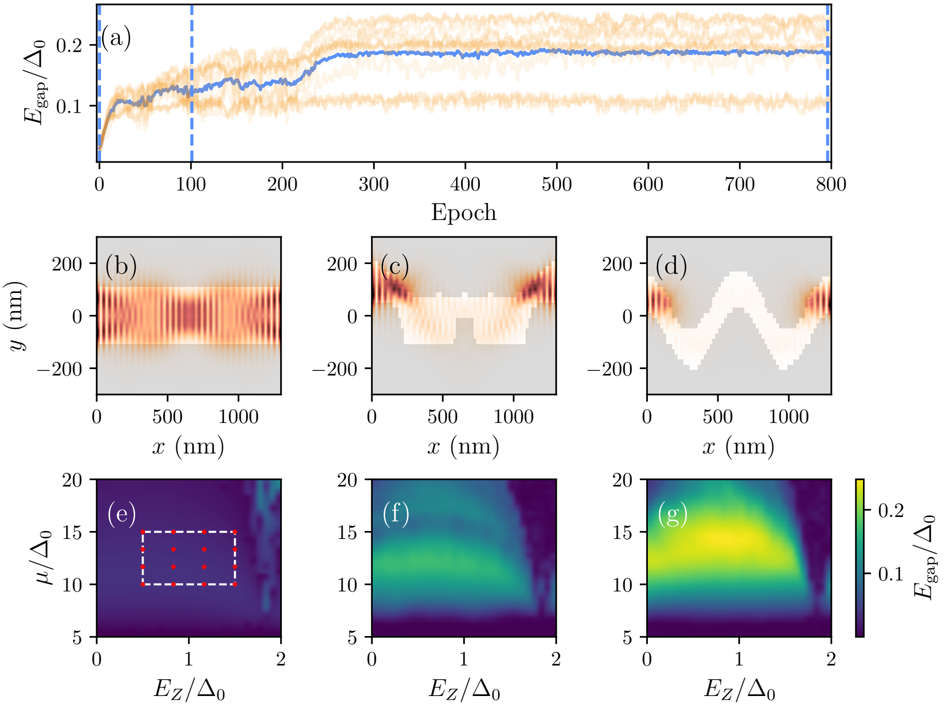

Figure 3.3: Optimization run starting from a straight geometry with homogeneous chemical potential and with parameter shifting and median filtering. (a) The blue curve corresponds to the average gap evaluated at 16 different points in parameter space, whose individual values we plot in orange. In panel (e) we mark these points with red dots. (b-d) Geometries found at the epochs marked with vertical dashed lines in panel (a). (e-f) Topological phase diagrams of the geometries in (b-d).

Having introduced the algorithm, we turn to investigate its performance, robustness, and the relevance of its components. Unless noted otherwise we perform epochs with 5 iterations per epoch and apply a median filter with a window size of $3a = 60$nm. Reflection symmetry $x \to L_x - x$ protects the gap from closing at finite momentum [31]. Therefore we consider only mirror-symmetric geometries $\Delta(x, y) = \Delta(L_x - x, y)$ and change the shape in pairs of reflection-symmetric sites simultaneously.

Figure 3.5 demonstrates our algorithm in action. We initialize the system with a straight geometry where the normal and superconducting regions have initial widths $W = 200\,\text{nm}$ and $L_{\text{SC}} = 500\,\text{nm}$ respectively. Further, we consider a parameter space of $\mu_1 = 10\,\text{meV}$, $\mu_2 = 15\,\text{meV}$, $E_{Z1} = 0.5\,\text{meV}$, $E_{Z2} = 1.5\,\text{meV}$, and apply the median filter every 5 epochs. In Fig. 3.3(a) we show how the gap of 16 uniformly spaced points in the parameter space evolves with epoch number. Although the gaps at fixed parameters fluctuate, the average increases smoothly as the optimization proceeds, eventually converging to a value approximately 10 times larger than the initial one. In Fig. 3.3(b-d) we show geometries and corresponding Majorana wavefunctions at the beginning of the optimization, its middle,

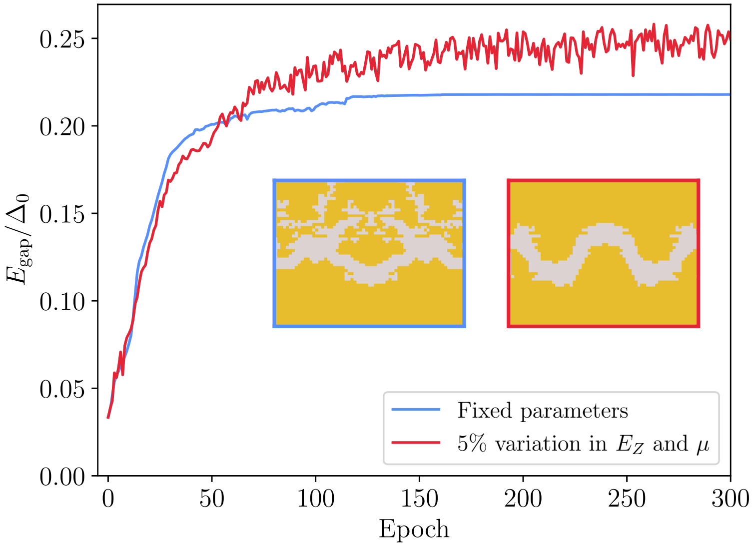

Figure 3.4: A comparison of the behavior of the optimizer with fixed Hamiltonian parameters and with random fluctuations in the chemical potential and Zeeman field. The blue curve shows the topological gap computed at each epoch for the optimizer with fixed parameters. At approximately 130 epochs it gets stuck in a local maximum. In contrast, the optimization with parameter shifting (red curve) avoids this local maximum and converges to higher gap values. Although the geometry has converged, the observed gaps oscillate about their average value due to the parameter shifting. The two inset plots show the converged geometries obtained at each run.

and at convergence. Similar to the zigzag geometries explored in [15], the final shape has a strong spatial modulation that eliminates long quasiparticle trajectories. Despite the algorithm imposing no such constraints, the converged geometry has a periodicity of half of the supercell. The increase in average gap leads to more localized Majorana wavefunctions, as is expected from the well-known relation for the localization length $\xi_M = \frac{\hbar v_F}{E_{\text{gap}}}$. Indeed, in the last iteration, the overlap of the Majoranas is already negligible within a single supercell. In Fig. 3.3(e-g) we plot topological phase diagrams as a function of μ and E_Z and find that the algorithm significantly increases the average gap both within the search window and in its vicinity.

We study the importance of individual aspects of the algorithm by examining their impact on the algorithm performance. To confirm the importance of the median filter, we check that excluding it generates discontinuous shapes shown in Fig. 3.5(a) and (c). Turning to the random sampling of parameters, we repeat the previous run with fixed parameters $\mu = 10\,\text{meV}$ and $E_Z = 1\,\text{meV}$, along with a parameter-shifting run with $\mu_1 = 9.5\,\text{meV}, \mu_2 = 10.5\,\text{meV}, E_{Z1} = 0.95\,\text{meV}, E_{Z2} = 1.05\,\text{meV}$.[1] We plot the observed gaps

---

[1] We choose a parameter window smaller than in Fig. 3.3 to reduce the fluctuations of the gap across epochs. In our simulations we found that the performance of the algorithms depends weakly on the window size, as long as it is neither too big nor too small.

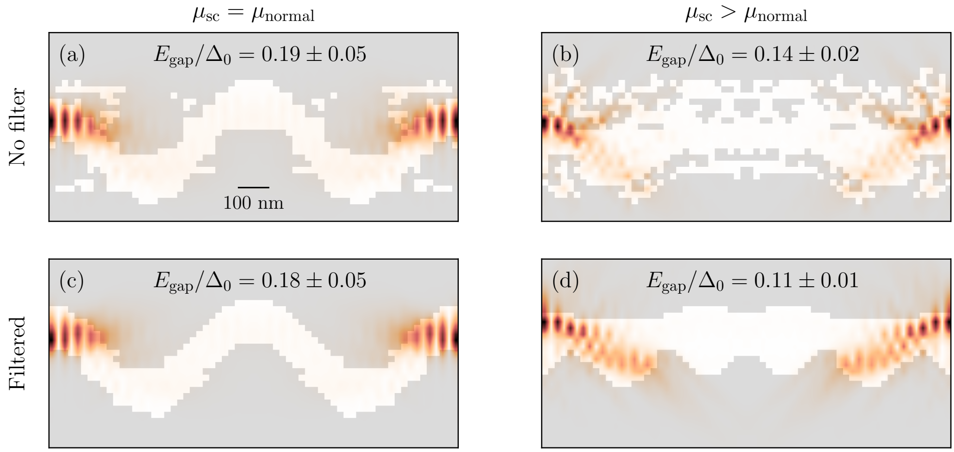

Figure 3.5: The effect of introducing median-filtering in the optimization algorithm. The top panels (a) and (b) show optimized geometries when starting from a straight junction with homogeneous and mismatched chemical potentials, respectively. The bottom panels (c) and (d) show the geometries obtained when a median filter is added. Each panel also shows the average gap over the range of μ and E_Z used in the optimization (see main text for exact parameters).

at each epoch in Fig. 3.4. Both runs result in geometries with significantly larger gaps than the straight junction. However, the optimizer with fixed parameters gets stuck in a local maximum with a gap of approximately $0.2\Delta_0$. In contrast, the parameter-shifting optimizer avoids this local maximum and continues exploring the geometry space until it converges to a shape with a gap of the order of $0.25\Delta_0$.

To study the robustness of our algorithm, we introduce several modifications in the optimization procedure and study how the results change in comparison with the reference geometry from Fig 3.3. In Fig. 3.6(a-b), we show results obtained with a different random seed and in Fig. 3.6(a-b) when the optimization starts from a zigzag geometry [15] (width and amplitude modulation of $W = z_y = 300$ nm). In both scenarios, the optimization converges to the reference up to 1–2 lattice sites. This suggests that the final result is independent of the details of the simulation parameters and that it is likely that the algorithm is converging to a global maximum in geometry space. Next, we allow the algorithm to add a single site per iteration, thereby removing the mirror symmetry constraint. To maintain consistency in the number of sites added per epoch we perform 10 iterations. Remarkably, although the optimizer starts by exploring highly mirror-asymmetric configurations, it eventually converges to the mirror-symmetric reference shape (Fig. 3.6(d-e)). Finally, we explore the effects of disorder in the junction Hamiltonian. We introduce an onsite potential $V_{\rm disorder}(x, y) = V_0(x, y)\tau_z$, where $V_0(x, y)$ is uniformly distributed in $[-W_0, W_0]$. We set the disorder strength at $W_0 = 1.7\,$meV, which corresponds to a mean free path of a unit cell length. To avoid overfitting to a specific disorder realization we sample a new set of $V_0(x, y)$ every epoch. Disorder effectively renormalizes Hamiltonian parameters and hence plays a similar role to parameter shifting. Therefore we opt for a smaller parameter window and set $\mu_1 = 9.5\,$meV, $\mu_2 = 10.5\,$meV, $E_{Z1} = 0.95\,$meV, $E_{Z2} = 1.05\,$meV. Once again

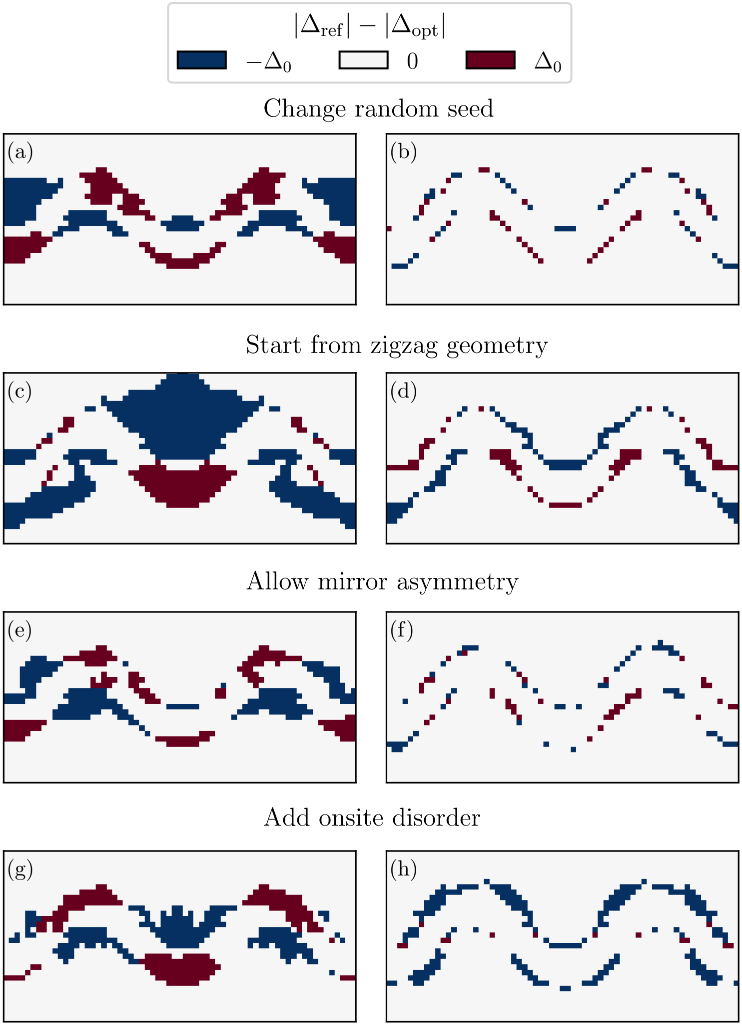

Figure 3.6: Comparison of optimized geometries with a reference geometry obtained by optimizing a straight junction with homogeneous chemical potential. In the panels we plot the difference of the magnitude of the superconducting gap of the reference geometries and the optimized geometries. The left panels show the geometry obtained after 50 epochs, and the right panels after convergence. Panels (a-b) correspond to geometries obtained with a different random seed, (c-d) starting the optimization from a zigzag shape, (e-f) allowing the optimizer to choose mirror-asymmetric perturbations, and (g-h) in the presence of onsite disorder.

the resulting shape differs from the reference by a few lattice sites (Fig. 3.6(g-h)).

All of the previous simulations converged to the same geometry, which raises the natural question of whether the optimizer generalizes well to other physical scenarios. To address this, we consider a modified version of the 2DEG junction with larger chemical potential in the proximized regions $\mu_{\mathrm{sc}} = 15\,\mathrm{meV}$, and a parameter range of

$\mu_{\text{normal},1} = 9.5\,\text{meV}, \mu_{\text{normal},2} = 10.5\,\text{meV}, E_{Z1} = 1.35\,\text{meV}, E_{Z2} = 1.65\,\text{meV}$. The higher chemical potential in the proximitized regions simulates the doping due to the work function difference [32, 33]. Figure 3.5(b) shows the geometry obtained with a run of 800 epochs without filtering. Interestingly, the optimizer converges to highly disordered superconductor shapes. This is in contrast with the previous simulations, where the unfiltered geometries remain approximately smooth. Applying the median filter at every epoch restores the smoothness of the final geometry 3.5(d)), but results in a significant reduction in the average topological gap. We attribute the overall lower gaps to the presence of normal scattering at the normal-superconductor interface caused by the Fermi velocity mismatch [34, 35]. This tends to reduce the induced superconducting gap and complicate the optimization problem. We have briefly explored optimization in another setup consisting of a straight junction with electrostatic gates next to the superconductors. Such a system would be less influenced by diamagnetic screening supercurrents that suppress the amplitude of Andreev reflection amplitude and hence the induced gap [36]. However, we did not obtain systematic results yet and thus we omit the discussion of these systems from the manuscript.

3.4. SUMMARY AND OUTLOOK

We have presented a greedy algorithm for finding Majorana junction geometries with large topological gaps. Our algorithm relies on parallelization and perturbation theory to sample geometry space efficiently and is compatible with minimum feature size and smoothness constraints. We validated our approach in different scenarios and showed that it is robust to variations in the starting point and the presence of disorder.

There are several possible improvements to the algorithm. A straightforward optimization would be to explore the hyperparameter space more systematically and find, for example, the optimal number of iterations per epoch and parameter window size. Additionally, the optimized geometries presented in the main text have periods shorter than our initial choice of L_x. This suggests that allowing the optimizer to dynamically adjust the period of the unit cell may increase performance. Another direction of further research would be to go beyond our greedy strategy and implement more sophisticated algorithms to explore the tree of perturbations such as Monte Carlo tree search [37].

While our results look promising, they are not yet experimentally relevant. The state-of-the-art experiments in 2DEG heterostructures do not offer sufficient insight into the material properties to enable predictive simulations. On the theoretical side, we have neglected several phenomena, namely electrostatics and magnetic field distribution, which will strongly influence the optimal geometry shape. Including these effects in the simulation requires significantly higher computational resources and is not justified without more knowledge about the platform.

We expect that our algorithm applies to other Majorana devices, such as Majorana Josephson junctions that only require phase gradients to break time-reversal symmetry [38, 39]. Geometry optimization can answer whether the previously reported small gaps in the high-density regime are an inherent problem of this platform. While our initial experiments indicate that the algorithm is directly suitable to gate shape optimization, more work is required to achieve a reliable conclusion.

Considering geometry optimization beyond Majorana Josephson junctions, we believe that the core ideas of our approach would apply to other inverse design problems in mesoscopic quantum physics [40]. The stochastic nature of our algorithm safeguards it from overfitting, but on the other hand makes it unsuitable to find sharp resonances or phenomena that are sensitive to microscopic device details. This, however, is a natural setting in many experiments where the control over the system is imprecise. The numerical efficiency of our approach largely relies on the locality of the perturbation used to estimate the gradient of the target function. Local control over microscopic Hamiltonians is far beyond current experimental reach. A practical adaptation of our algorithm to nonlocal perturbations would approximate those as local during most optimization steps and only recompute the precise observables at the beginning of an epoch.

ACKNOWLEDGEMENTS

We are grateful to Mert Bozkurt, Evert van Nieuwenburg and Andrew Saydjari for useful discussions.

Data availability The code used to generate the figures is available on Zenodo [41].

Author contributions A.A. defined the goal of the project, and A.A. and A.M. designed the approach. T.T. implemented an initial unreported version of the optimization under the supervision of A.M. and A.A. A.M. implemented the final version of the optimizer and performed the numerical experiments in the manuscript. A.M. and A.A. interpreted the results. A.M. wrote the manuscript with input from A.A.

Funding information This work was supported by the Netherlands Organization for Scientific Research (NWO/OCW), as part of the Frontiers of Nanoscience program and an NWO VIDI grant 016.Vidi.189.180.

REFERENCES

[1] A. Y. Kitaev, *Unpaired Majorana fermions in quantum wires,* Phys. Usp. **44**, 131 (2001).

[2] J. Alicea, *New directions in the pursuit of Majorana fermions in solid state systems,* Rep. Prog. Phys. **75**, 076501 (2012).

[3] C. Beenakker, *Search for Majorana fermions in superconductors,* Annu. Rev. Condens. Matter Phys. **4**, 113 (2013).

[4] M. Leijnse and K. Flensberg, *Introduction to topological superconductivity and Majorana fermions,* Semicond. Sci. Technol. **27**, 124003 (2012).

[5] Y. Oreg, G. Refael, and F. von Oppen, *Helical liquids and Majorana bound states in quantum wires,* Phys. Rev. Lett. **105**, 177002 (2010).

[6] R. M. Lutchyn, J. D. Sau, and S. Das Sarma, *Majorana fermions and a topological phase transition in semiconductor-superconductor heterostructures,* Phys. Rev. Lett. **105**, 077001 (2010).

[7] R. M. Lutchyn, E. P. A. M. Bakkers, L. P. Kouwenhoven, P. Krogstrup, C. M. Marcus, and Y. Oreg, *Majorana zero modes in superconductor–semiconductor heterostructures,* Nat. Rev. Mater. **3**, 52 (2018).

[8] H. Zhang, D. E. Liu, M. Wimmer, and L. P. Kouwenhoven, *Next steps of quantum transport in Majorana nanowire devices,* Nature Communications **10**, 5128 (2019).

[9] M. Hell, M. Leijnse, and K. Flensberg, *Two-Dimensional Platform for Networks of Majorana Bound States,* Phys. Rev. Lett. **118**, 107701 (2017).

[10] F. Pientka, A. Keselman, E. Berg, A. Yacoby, A. Stern, and B. I. Halperin, *Topological Superconductivity in a Planar Josephson Junction,* Phys. Rev. X **7**, 021032 (2017).

[11] H. Ren, F. Pientka, S. Hart, A. T. Pierce, M. Kosowsky, L. Lunczer, R. Schlereth, B. Scharf, E. M. Hankiewicz, L. W. Molenkamp, B. I. Halperin, and A. Yacoby, *Topological superconductivity in a phase-controlled Josephson junction,* Nature **569**, 93 (2019).

[12] A. Fornieri, A. M. Whiticar, F. Setiawan, E. Portolés, A. C. C. Drachmann, A. Keselman, S. Gronin, C. Thomas, T. Wang, R. Kallaher, G. C. Gardner, E. Berg, M. J. Manfra, A. Stern, C. M. Marcus, and F. Nichele, *Evidence of topological superconductivity in planar Josephson junctions,* Nature **569**, 89 (2019).

[13] C. T. Ke, C. M. Moehle, F. K. de Vries, C. Thomas, S. Metti, C. R. Guinn, R. Kallaher, M. Lodari, G. Scappucci, T. Wang, R. E. Diaz, G. C. Gardner, M. J. Manfra, and S. Goswami, *Ballistic superconductivity and tunable π–junctions in InSb quantum wells,* Nat. Commun. **10**, 1 (2019).

[14] P. de Gennes and D. Saint James, *Elementary excitations in the vicinity of a normal metal-superconducting metal contact,* Phys. Lett. **4**, 151 (1963).

[15] T. Laeven, B. Nijholt, M. Wimmer, and A. R. Akhmerov, *Enhanced Proximity Effect in Zigzag-Shaped Majorana Josephson Junctions,* Phys. Rev. Lett. **125**, 086802 (2020).

[16] B. D. Woods and T. D. Stanescu, *Enhanced topological protection in planar quasi-one-dimensional channels with periodically modulated width,* Phys. Rev. B **101**, 195435 (2020).

[17] P. P. Paudel, T. Cole, B. D. Woods, and T. D. Stanescu, *Enhanced topological superconductivity in spatially modulated planar Josephson junctions,* Phys. Rev. B **104**, 155428 (2021).

[18] O. Sigmund and J. Søndergaard Jensen, *Systematic design of phononic band–gap materials and structures by topology optimization,* Philosophical Transactions of the Royal Society of London. Series A: Mathematical, Physical and Engineering Sciences **361**, 1001 (2003).

[19] L. Shen, Z. Ye, and S. He, *Design of two-dimensional photonic crystals with large absolute band gaps using a genetic algorithm,* Phys. Rev. B **68**, 035109 (2003).

[20] Z.-f. Liu, B. Wu, and C.-f. He, *Band-gap optimization of two-dimensional phononic crystals based on genetic algorithm and FPWE,* Wave. Random Complex **24**, 286 (2014).

[21] H. Men, N. Nguyen, R. Freund, P. Parrilo, and J. Peraire, *Bandgap optimization of two-dimensional photonic crystals using semidefinite programming and subspace methods,* J. Comput. Phys. **229**, 3706 (2010).

[22] H. Men, K. Y. K. Lee, R. M. Freund, J. Peraire, and S. G. Johnson, *Robust topology optimization of three-dimensional photonic-crystal band-gap structures,* Opt. Express **22**, 22632 (2014).

[23] M. Wormser, F. Wein, M. Stingl, and C. Körner, *Design and Additive Manufacturing of 3D Phononic Band Gap Structures Based on Gradient Based Optimization,* Materials **10**, 1125 (2017).

[24] R. E. Christiansen, F. Wang, and O. Sigmund, *Topological Insulators by Topology Optimization,* Phys. Rev. Lett. **122**, 234502 (2019).

[25] V. Peano, F. Sapper, and F. Marquardt, *Rapid Exploration of Topological Band Structures Using Deep Learning,* Phys. Rev. X **11**, 021052 (2021).

[26] S. Boutin, J. Camirand Lemyre, and I. Garate, *Majorana bound state engineering via efficient real-space parameter optimization,* Phys. Rev. B **98**, 214512 (2018).

[27] S. Turcotte, S. Boutin, J. C. Lemyre, I. Garate, and M. Pioro Ladrière, *Optimized micromagnet geometries for Majorana zero modes in low g-factor materials,* Phys. Rev. B **102**, 125425 (2020).

[28] N. Khaneja, T. Reiss, C. Kehlet, T. Schulte Herbrüggen, and S. J. Glaser, *Optimal control of coupled spin dynamics: Design of NMR pulse sequences by gradient ascent algorithms,* J. Magn. Reson. **172**, 296 (2005).

[29] C. W. Groth, M. Wimmer, A. R. Akhmerov, and X. Waintal, *Kwant: A software package for quantum transport,* New J. Phys. **16**, 063065 (2014).

[30] Dask Development Team, *Dask: Library for dynamic task scheduling* (2016), `https://dask.org`.

[31] B. Nijholt and A. R. Akhmerov, *Orbital effect of magnetic field on the Majorana phase diagram,* Phys. Rev. B **93**, 235434 (2016).

[32] A. E. G. Mikkelsen, P. Kotetes, P. Krogstrup, and K. Flensberg, *Hybridization at Superconductor-Semiconductor Interfaces,* Phys. Rev. X **8**, 031040 (2018).

[33] A. E. Antipov, A. Bargerbos, G. W. Winkler, B. Bauer, E. Rossi, and R. M. Lutchyn, *Effects of Gate-Induced Electric Fields on Semiconductor Majorana Nanowires,* Phys. Rev. X **8**, 031041 (2018).

[34] G. E. Blonder and M. Tinkham, *Metallic to tunneling transition in Cu-Nb point contacts,* Phys. Rev. B **27**, 112 (1983).

[35] N. A. Mortensen, K. Flensberg, and A.-P. Jauho, *Angle dependence of Andreev scattering at semiconductor–superconductor interfaces,* Phys. Rev. B **59**, 10176 (1999).

[36] F. Rohlfing, G. Tkachov, F. Otto, K. Richter, D. Weiss, G. Borghs, and C. Strunk, *Doppler shift in Andreev reflection from a moving superconducting condensate in Nb/InAs Josephson junctions,* Phys. Rev. B **80**, 220507 (2009).

[37] C. B. Browne, E. Powley, D. Whitehouse, S. M. Lucas, P. I. Cowling, P. Rohlfshagen, S. Tavener, D. Perez, S. Samothrakis, and S. Colton, *A Survey of Monte Carlo Tree Search Methods,* IEEE T COMP INTEL AI **4**, 1 (2012).

[38] A. Melo, S. Rubbert, and A. Akhmerov, *Supercurrent-induced Majorana bound states in a planar geometry,* SciPost Physics **7**, 039 (2019).

[39] O. Lesser, A. Saydjari, M. Wesson, A. Yacoby, and Y. Oreg, *Phase-induced topological superconductivity in a planar heterostructure,* Proc. Natl. Acad. Sci. **118** (2021), 10.1073/pnas.2107377118.

[40] K. Ryczko, P. Darancet, and I. Tamblyn, *Inverse Design of a Graphene-Based Quantum Transducer via Neuroevolution,* The Journal of Physical Chemistry C **124**, 26117 (2020).

[41] A. Melo, T. Tanev, and A. R. Akhmerov, *Greedy optimization of the geometry of Majorana Josephson junctions,* (2022).

4

CONDUCTANCE ASYMMETRIES IN MESOSCOPIC SUPERCONDUCTING DEVICES DUE TO FINITE BIAS

This chapter has been previously published as André Melo, Chun-Xiao Liu, Piotr Rożek, Tómas Örn Rosdahl, Michael Wimmer, *Conductance asymmetries in mesoscopic superconducting devices due to finite bias*, SciPost Phys. 10, 037 (2021) .

4.1. INTRODUCTION

Hybrid nanostructures combining spin-orbit coupled semiconducting nanowires and conventional superconductivity are a promising candidate to host Majorana bound states (MBS) [1–16]. Much of the ongoing experimental work on these devices relies on two-terminal tunnel spectroscopy in which the nanowires are coupled to a normal reservoir through an electrostatic tunnel barrier. In the tunneling limit the conductance through the normal-superconductor (NS) junction is proportional to the local density of states at the edge of the nanowire. This allows to measure local signatures of MBS such as a resonant zero-bias conductance peak [17–27]. Additionally, a three-terminal setup allows to probe nonlocal conductances, which can provide information about the bulk topology and the BCS charge of bound states [28–30].

A common theoretical framework for calculating the conductance in NS junctions is the scattering matrix (S) method under the linear response approximation [31]. In the presence of particle-hole symmetry and unitarity of the S matrix, the linear response conductance G obeys several symmetry relations at voltages below the superconducting gap Δ. In two-terminal setups, for example, the conductance is symmetric about the zero bias voltage point, i.e., $G(V) = G(-V)$ for $|V| < \Delta/e$ [32, 33]. In three-terminal setups, it has recently been shown that the anti-symmetric components of the local and nonlocal conductance matrices are equal [30]. However, in experiments these symmetry relations are only observed approximately [34–39]. So far, possible mechanisms for the observed deviations that have been discussed in the literature always rely on coupling to a reservoir of quasiparticles, for example through dissipation due to a residual density of states in the parent superconductor or additional low-energy states [33, 40], or inelastic relaxation processes connecting subgap states to the above-gap continuum [41].

In this work we go beyond the linear response regime and study how finite-bias effects break conductance symmetry relations, without the need for quasiparticle poisoning. In particular, we consider the dependence of the tunnel barrier profile and transparency on the applied bias voltage in the normal lead [32, 42, 43]. In two-terminal setups, we find that a voltage-dependent tunnel barrier introduces asymmetry in both the width and height of subgap conductance peaks. Moreover, we study the conductance asymmetry as a function of system parameters, and show that it is enhanced by mirror asymmetric barrier shapes. We also identify general features that can be used to experimentally determine whether finite-bias effects are the main source of conductance asymmetry. Finally, we turn our attention to three-terminal setups and observe that finite-bias effects break conductance symmetries in accordance with recent experimental work [39].

4.2. FINITE-BIAS CONDUCTANCE IN A MESOSCOPIC SUPERCONDUCTING SYSTEM

The formalism for computing the nonlinear conductance in a mesoscopic superconducting device has been derived in [32]. We give a concise summary here to point out the important aspects for our study.

Consider a scattering region attached to a normal lead and a superconducting lead shown schematically in Fig. 4.1(a). Using the Landauer-Buttiker formalism [31, 44] we

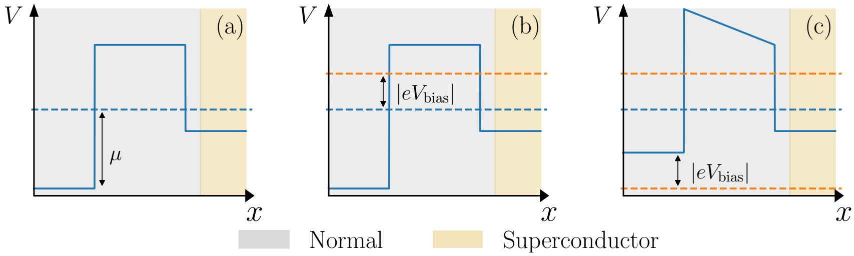

Figure 4.1: (a) Schematic band diagram of an NS tunnel junction at zero bias voltage. (b) Calculating conductance through the junction in the linear response limit. The voltage dependence of the scattering region is neglected and therefore the scattering matrix depends solely on the energy of incoming modes. (c) Finite-bias conductance includes changes in the electrostatic profile of the junction due to the applied voltage, e.g. a positive shift of the chemical potential near the normal lead, along with a linear voltage drop across the tunnel barrier. As a result the scattering matrix depends on both the energy of the incoming modes and the applied bias voltage.

write the current in the normal lead as a sum of three contributions

$$I^{(\mathrm{e})} = -\frac{e}{h}\int dE\, f(E+eV_\text{bias})[N(E,V_\text{bias})-R_{ee}(E,V_\text{bias})], \tag{4.1}$$

$$\begin{aligned} I^{(\mathrm{h})} &= \frac{e}{h}\int dE\, f(E-eV_\text{bias})R_{eh}(E,V_\text{bias}) \\ &= \frac{e}{h}\int dE[1-f(E+eV_\text{bias})]R_{he}(E,V_\text{bias}), \end{aligned} \tag{4.2}$$

$$I^{(\mathrm{sc})} = \frac{e}{h}\int dE\, f(E)T_{es}(E,V_\text{bias}), \tag{4.3}$$

where $e=|e|$ and we have set the chemical potential of the superconductor to zero. $I^{(\mathrm{e})}$ ($I^{(\mathrm{h})}$) is the current carried by electrons (holes), $I^{(\mathrm{sc})}$ the current originating from quasiparticles in the superconducting lead, and

$$f(E) = \frac{1}{1+\exp\left(\frac{E-\mu}{k_B T}\right)} \tag{4.4}$$

is the Fermi-Dirac distribution. N is the number of electron modes in the normal lead, R_{ee} the total electron reflection amplitude, R_{eh} the total Andreev reflection amplitude and T_{es} the transmission amplitude from the superconductor above-gap modes. In contrast with the conductance obtained in the linear response approximation, the finite-bias conductance takes into account changes in the profile of the tunnel barrier due to the applied bias voltage V_bias (Fig. 4.1(c)). Therefore R_{ee}, R_{eh} and T_{es} depend not only on the energy of incoming particles E, but also on V_bias. Unitarity of the scattering matrix implies that

$$N(E,V_\text{bias}) = R_{ee}(E,V_\text{bias}) + R_{eh}(E,V_\text{bias}) + T_{es}(E,V_\text{bias}). \tag{4.5}$$

Hence

$$\begin{aligned} I^{(\mathrm{sc})} &= \frac{e}{h}\int dE\, f(E)[N(E,V_{\mathrm{bias}}) - R_{ee}(E,V_{\mathrm{bias}}) - R_{eh}(E,V_{\mathrm{bias}})] \\ &= \frac{e}{h}\int dE\, f(E)[N(E,V_{\mathrm{bias}}) - R_{ee}(E,V_{\mathrm{bias}})] - \frac{e}{h}\int dE[1-f(E)]R_{he}(E,V_{\mathrm{bias}}) \\ &= \frac{e}{h}\int dE\, f(E)[N(E,V_{\mathrm{bias}}) - R_{ee}(E,V_{\mathrm{bias}}) + R_{he}(E,V_{\mathrm{bias}})] \\ &\qquad - \frac{e}{h}\int dE\, R_{he}(E,V_{\mathrm{bias}}). \end{aligned} \tag{4.6}$$

The total current is then given by

$$I = \frac{e}{h}\int dE[f(E) - f(E+eV_{\mathrm{bias}})][N(E,V_{\mathrm{bias}}) - R_{ee}(E,V_{\mathrm{bias}}) + R_{he}(E,V_{\mathrm{bias}})]. \tag{4.7}$$

In the zero-temperature limit the conductance reduces to [32]

$$\begin{aligned} G = \frac{dI}{dV_{\mathrm{bias}}} &= \frac{e^2}{h}\left(N(-eV_{\mathrm{bias}},V_{\mathrm{bias}}) - R_{ee}(-eV_{\mathrm{bias}},V_{\mathrm{bias}}) + R_{he}(-eV_{\mathrm{bias}},V_{\mathrm{bias}})\right) \\ &\quad - \frac{e}{h}\int_0^{-eV_{\mathrm{bias}}} dE\left[\frac{\partial R_{he}(E,V_{\mathrm{bias}})}{\partial V} - \frac{\partial R_{ee}(E,V_{\mathrm{bias}})}{\partial V}\right]. \end{aligned} \tag{4.8}$$

Equation (4.8) is the most general form of finite-bias conductance. It does not assume any specific electrostatic profile of the junction and is also valid for multi-terminal setups. When the dependence of the NS junction on the applied bias voltage is ignored (Fig. 4.1(b)), that is $R_{ij}(E,V_{\mathrm{bias}}) \to R_{ij}(E,0)$, Eq. (4.8) reduces to the well-known expression for NS conductance in the linear response limit

$$G_{\mathrm{lin}}(V_{\mathrm{bias}}) = \frac{2e^2}{h}\left(N - R_{ee}(-eV_{\mathrm{bias}}) + R_{he}(-eV_{\mathrm{bias}})\right), \tag{4.9}$$

which satisfies the symmetry relation $G(V_{\mathrm{bias}}) = G(-V_{\mathrm{bias}})$ at voltages below the superconducting gap [32, 33].

4.3. FINITE-BIAS LOCAL CONDUCTANCE INTO A SINGLE ANDREEV BOUND STATE

To obtain a qualitative understanding of the influence of finite-bias effects, we first consider a toy model of an NS junction where the nanowire hosts a single Andreev bound state:

$$H = E_0\begin{pmatrix} 1 & 0 \\ 0 & -1 \end{pmatrix}. \tag{4.10}$$

Below the superconducting gap, Eq. (4.8) reduces to

$$\frac{G}{2G_0} = R_{he}(-eV_{\mathrm{bias}},V_{\mathrm{bias}}) - \frac{1}{e}\int_0^{-eV_{\mathrm{bias}}} dE\,\frac{\partial R_{he}(E,V_{\mathrm{bias}})}{\partial V}, \tag{4.11}$$

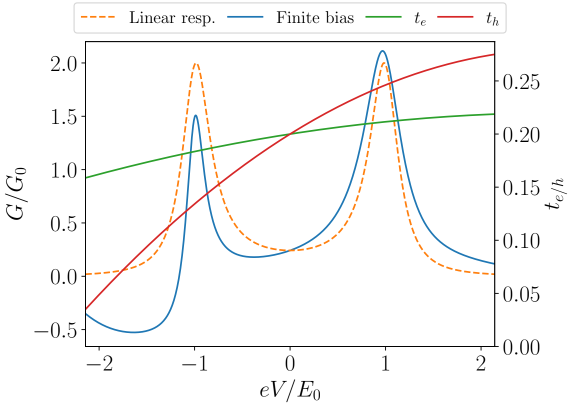

Figure 4.2: Two-terminal NS conductance into a single Andreev bound state with a scattering region sensitive to the applied bias voltage. In the linear response approximation the voltage dependence of the scattering region is neglected, resulting in particle-hole symmetric conductance profiles (orange dashed lines). When a voltage dependence is included in the electron/hole tunneling amplitude $t_{e/h}$ (red/green solid lines), the corresponding conductance profiles (blue solid lines) show different heights and widths at positive and negative bias voltage.

where $G_0 = \frac{e^2}{h}$ is the conductance quantum. $R_{he}(E, V)$ can be obtained by taking the trace over the appropriate block of the scattering matrix, which we compute through the Mahaux-Weidenmüller formula

$$S = \mathbb{1} - 2\pi W^\dagger (E - H + \pi W W^\dagger)^{-1} W, \tag{4.12}$$

where

$$W = \begin{pmatrix} u t_e(E,V) & v^* t_h(E,V)^* \\ v t_e(E,V) & -u^* t_h(E,V)^* \end{pmatrix} \tag{4.13}$$

parameterizes the coupling of the bound states to the lead modes. For notational convenience we drop the E and V dependencies of $t_{e/h}$ below, but their presence should be kept in mind.

We start by computing the first term in Eq. (4.11). The Andreev reflection amplitude is given by

$$\begin{aligned} 16\pi^2 E_0^2 |u v t_e t_h|^2 \cdot \{ &(E^2 - E_0^2)^2 + \pi^2 [2 E E_0 (|u|^2 - |v|^2)(|t_e|^4 - |t_h|^4) \\ &- 4E_0^2 |uv|^2 (|t_e|^2 - |t_h|^2)^2 + (E^2 + E_0^2)(|t_e|^4 + |t_h|^4)] \}^{-1} \end{aligned} \tag{4.14}$$

where we assume the junction is in the tunneling limit so that $t_{e/h} \ll E_0$ and we can safely discard terms of order higher than $\mathcal{O}(t_{e/h}^4)$. In the vicinity of $E = E_0$ we obtain the approximate expression

$$R_{he}(-eV_{\text{bias}}, V_{\text{bias}}) \approx \frac{4\pi^2 |t_e t_h u v|^2}{(-eV_{\text{bias}} - E_0)^2 + \pi^2 \left(|t_e u|^2 + |t_h v|^2 \right)^2}. \tag{4.15}$$

Hence, the first term in Eq. (4.11) gives a Lorentzian conductance profile with a resonance at $|V| = E_0/e$. The height and full-width half maximums of the resonances are given by

$$\frac{G_{\max}}{2G_0} = \frac{4|t_e t_h u v|^2}{\left(|t_e u|^2 + |t_h v|^2\right)^2}, \tag{4.16}$$

$$\mathrm{FWHM} = \frac{2\pi}{e}\left(|t_e u|^2 + |t_h v|^2\right). \tag{4.17}$$

The expressions for $V = -E_0/e$ can be readily obtained through the transformation $u \leftrightarrow v$. In the linear response regime we have $t_{e/h}(E, V_{\mathrm{bias}}) = t_{e/h}(E, 0)$. Particle-hole symmetry gives the constraint $t_e(E,0) = t_h(-E,0)$ and thus the subgap conductance is also particle-hole symmetric. However, when finite-bias effects are included, $t_{e/h}(\pm E_0, \pm E_0/e)$ are not constrained to be equal, resulting in particle-hole asymmetric conductance.

The contribution of the second term in Eq. (4.11) is (see App. 4.A for the full calculation)

$$-\frac{2e}{h}\int_0^{-eV_{\mathrm{bias}}} dE\,\frac{\partial R_{he}}{\partial V} = \left[A \arctan\left(\frac{2(E-E_0)}{\mathrm{FWHM}}\right) + B\frac{E-E_0}{\left(\frac{\mathrm{FWHM}}{2}\right)^2 + (E-E_0)^2}\right]_0^{-eV_{\mathrm{bias}}}, \tag{4.18}$$

where

$$A = -\frac{G_{\max}\cdot \mathrm{FWHM}}{2G_0|t_e t_h|}\frac{\partial |t_e t_h|}{\partial V}\bigg|_{\substack{E=E_0\\ V=-E_0/e}} + \frac{\pi^2 G_{\max}}{2G_0 e^2\cdot \mathrm{FWHM}}\frac{\partial\left(|u t_e|^2 + |v t_h|^2\right)^2}{\partial V}\bigg|_{\substack{E=E_0\\ V=-E_0/e}} \tag{4.19}$$

$$B = \frac{\pi^2 G_{\max}}{2G_0 e^2\cdot \mathrm{FWHM}}\frac{\partial\left(|u t_e|^2 + |v t_h|^2\right)^2}{\partial V}\bigg|_{\substack{E=E_0\\ V=-E_0/e}} \tag{4.20}$$

Both terms in Eq. (4.18) vary on the scale of FWHM and therefore do not change the width of the Lorentzian peaks in Eq. (4.15). However, they change the height of Eq. (4.16) by $\approx -\pi A/2 - B/E_0$.

To compute the conductance of the toy model, we choose $u = v = 1/\sqrt{2}$ and expand the tunnel rates about $E = V_{\mathrm{bias}} = 0$ up to second order:

$$t_{e/h}(-eV_{\mathrm{bias}}, V_{\mathrm{bias}}) \approx t_{e,h}(0,0) + a_{e/h}V_{\mathrm{bias}} + b_{e/h}V_{\mathrm{bias}}^2. \tag{4.21}$$

The remaining parameters can be found in the accompanying code for the manuscript [45]. We show the resulting finite-bias conductance profile along with the corresponding linear response conductance in Fig. 4.2. In accordance with the analytical results in Eqs. (4.16) and (4.17), the finite-bias conductance peaks exhibit height and width asymmetry. Moreover, we observe that the finite-bias conductance has a region with negative values, which is due to the presence of the integral term. In contrast, the linear response conductance must always be positive.

4.4. TIGHT BINDING SIMULATIONS

4.4.1. FINITE-BIAS LOCAL CONDUCTANCE IN A NORMAL/SUPERCONDUCTOR GEOMETRY

To investigate finite-bias effects at a more realistic level, we consider a one-dimensional semiconductor-superconductor nanowire coupled to a normal lead. The Bogoliubov-de

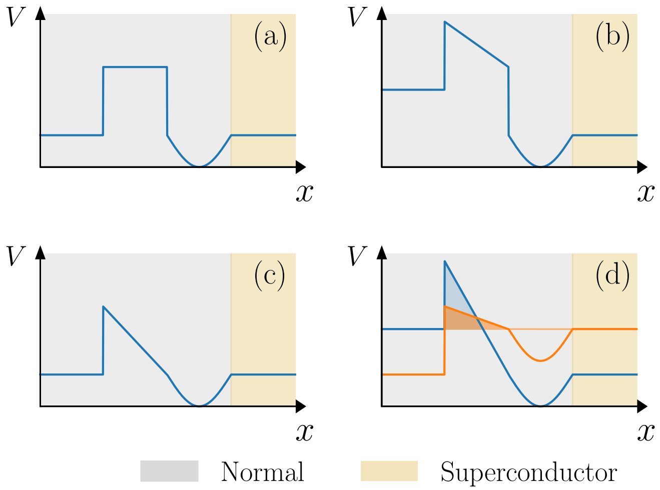

Figure 4.3: NS junctions with a bias-dependent tunnel barrier and a quantum dot potential. In the top figures we show a square barrier with at (a) zero bias voltage, and (b) negative bias voltage. In the bottom figures we show a triangular barrier at (c) zero bias voltage, and (d) at negative bias voltage (blue curve) and positive bias voltage (orange curve). The shaded regions indicate the effective barrier seen by an incoming electron at $E = -eV_{\text{bias}}$. When the barrier is triangular shaped, the effective barrier at positive voltage is smaller than at negative voltage, thus amplifying particle-hole asymmetry in conductance.

Gennes Hamiltonian for the NS junction can be written as

$$H = \left(\frac{p_x^2}{2m_{\text{eff}}} + \alpha p_x \sigma_y - \mu(x) + V(x, V_{\text{bias}})\right)\tau_z + V_Z\sigma_x + \Delta(x)\tau_x, \tag{4.22}$$

where σ_i and τ_i are Pauli matrices acting in spin and Nambu space, $p_x = -i\hbar d/dx$, m_{eff} the effective mass, μ the chemical potential, V the onsite electrostatic potential, α the strength of Rashba spin-orbit interaction, V_Z the Zeeman spin splitting, and Δ the superconducting gap. In particular, the chemical potential is a piecewise constant function of x as

$$\mu(x) = \begin{cases} \mu_{\text{lead}}, & x < 0 \\ \mu_{\text{wire}}, & x > 0, \end{cases} \tag{4.23}$$

and the superconducting gap $\Delta(x)$ is finite only inside the nanowire.

The onsite potential has two terms $V(x, V_{\text{bias}}) = V_{\text{barrier}}(x, V_{\text{bias}}) + V_{\text{dot}}(x)$ illustrated in Fig. 4.3 (a)-(b). The first term corresponds to the electrostatic potential induced by the tunnel gate, which we model as a square barrier at equilibrium. A detailed calculation of the transport properties at finite bias requires a non-equilibrium approach [46]. However, in the tunneling regime the system is well approximated by the following phenomenological model. When a bias is applied, the band bottom of the normal lead is shifted by

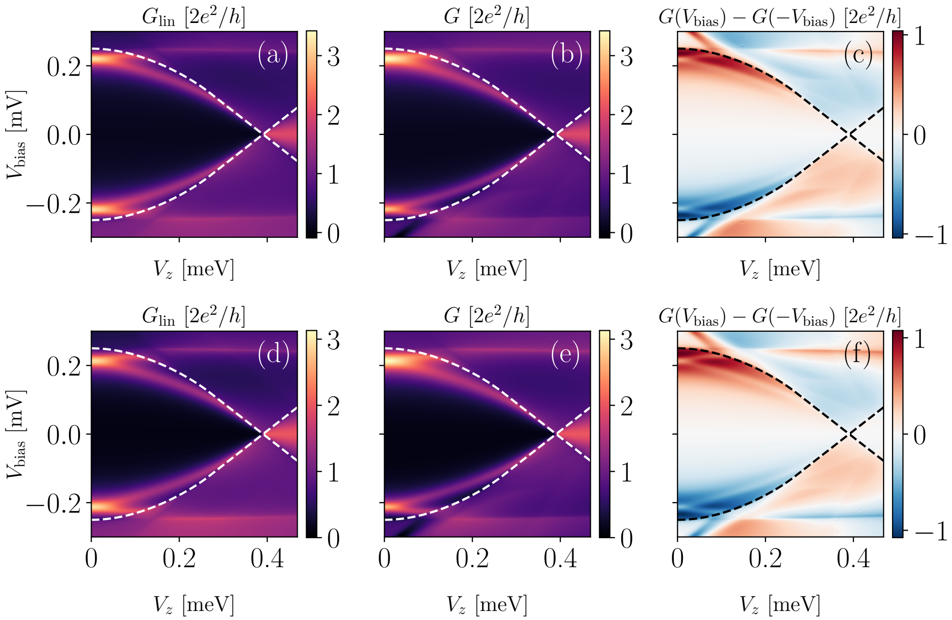

Figure 4.4: Two-terminal conductance as a function of Zeeman field and bias voltage in a proximitized nanowire with $\Delta = 0.25$ meV. The system in the top panels has a square barrier and in bottom panels a triangular barrier. The linear response conductance ((a) and (d)) is particle-hole symmetric below the induced gap (dashed lines). In contrast, the finite-bias conductance ((b) and (e)) shows significant particle-hole asymmetry below the gap which we plot explicitly in (c) and (f).

eV_{bias} and voltage drops linearly across the barrier [42, 47]:

$$V_{\mathrm{barrier}}(x) = \begin{cases} -eV_{\mathrm{bias}}, & x < 0 \\ eV_{\mathrm{barrier}} - eV_{\mathrm{bias}}(1 - \frac{x}{d}), & 0 \le x < d \\ 0, & x > d. \end{cases} \tag{4.24}$$

Because the chemical potential of the lead also shifts by $-eV_{\mathrm{bias}}$ when a voltage is applied, this potential keeps the charge density in the system constant. The second term is a smooth quantum dot potential [40]

$$V_{\mathrm{dot}}(x) = \begin{cases} V_{\mathrm{dot}} \cos\left(\frac{3(x-d)}{2L_{\mathrm{dot}}}\right), & d < x < d + L_{\mathrm{dot}} \\ 0, & \text{elsewhere}, \end{cases} \tag{4.25}$$

which induces a subgap Andreev bound state. In the following calculations and discussions we focus on how finite-bias effects cause particle-hole asymmetry for the Andreev bound state-induced resonance peaks at positive and negative bias voltages.

We apply the finite difference approximation to the continuum Hamiltonian (5.3) with a lattice constant of 1 nm, and numerically study the resulting tight-binding Hamiltonian using the Kwant software package [48]. Unless stated otherwise, the Hamiltonian parameters are $m_{\mathrm{eff}} = 0.02 m_e$, $\Delta = 0.25$ meV, $\alpha = 50$ meV nm, $V_{\mathrm{dot}} = 2.2$ meV, $\mu_{\mathrm{wire}} = 0.3$ meV,

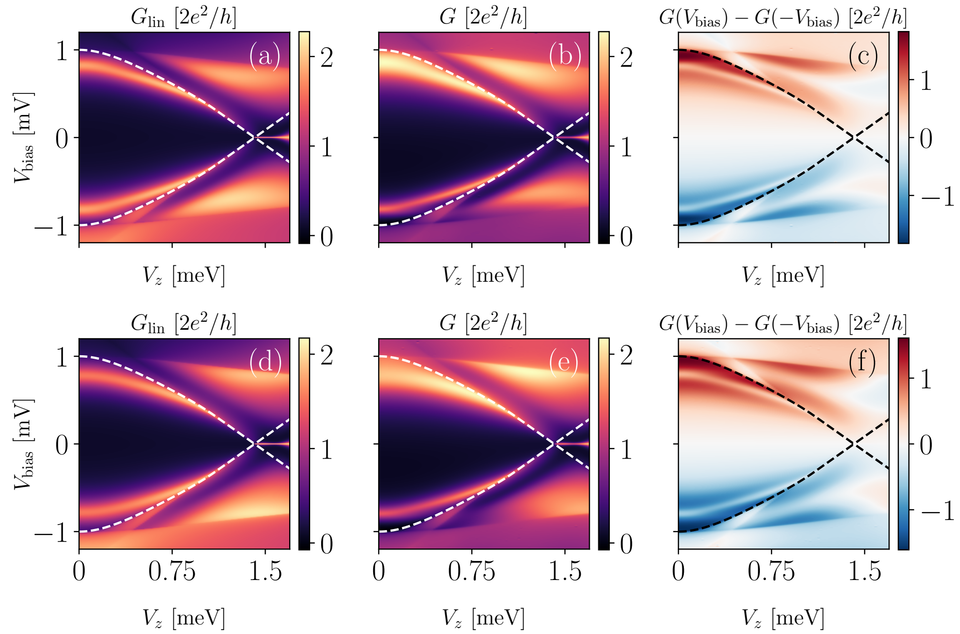

Figure 4.5: Two-terminal conductance as a function of Zeeman field and bias voltage in a proximitized nanowire with $\Delta = 1$ meV. The system in the top panels has a square barrier ($V_{\text{barrier}} = 0.8$ meV), and in bottom panels a triangular barrier ($V_{\text{barrier}} = 1.6$ meV). (a) and (d) show the linear response conductance, (b) and (e) the finite-bias conductance and (c) and (d) the asymmetry in finite-bias conductance.

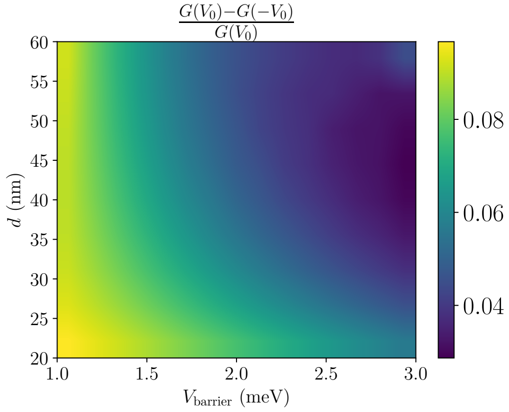

Figure 4.6: Normalized height asymmetry of conductance peaks in proximitized nanowire with $\Delta = 0.25$ meV and $V_Z = 0$ for varying barrier width d and height V_{barrier}. The asymmetry vanishes as either the system is tuned deeper into the tunneling regime.

$\mu_{\text{lead}} = 0.55$ meV and the geometry parameters are $d = 80$ nm, $L_{\text{dot}} = 180$ nm. The source

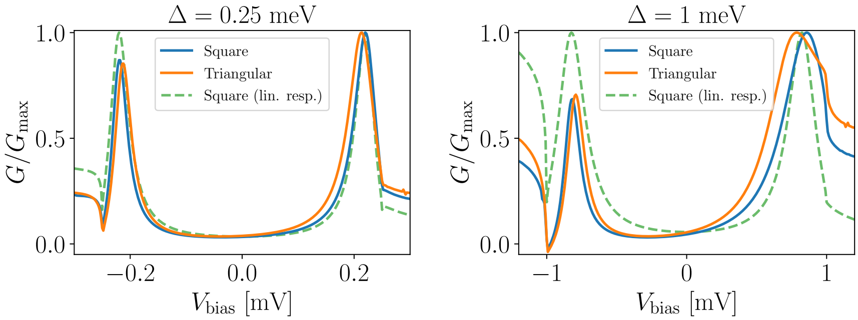

Figure 4.7: (a) Normalized finite-bias and linear-response conductances of systems with a square barrier and triangular barrier at $V_Z = 0$ and (a) $\Delta = 0.25$ meV and (b) $\Delta = 1$ meV (blue lines). Adding finite-bias effects breaks particle-hole symmetry of the linear response conductance (green dashed lines). A triangular tunnel barrier amplifies the width asymmetry of the peaks (though their height does not change significantly) because the effective barrier at positive voltages is smaller than at negative voltages.

code and data used to produce the figures in this work are available in [45].

In Fig. 4.4(a) and (b) we show the linear response and finite-bias conductances as a function of bias voltage and Zeeman field strength. The Andreev bound state induces a resonance peak below the superconducting gap (white dashed line). Additionally, we plot the conductance asymmetry in Fig. 4.4(c). The conductance peaks display significant asymmetry in both their width and height. Furthermore, the magnitude of the asymmetry decreases as the peaks get closer to zero energy. This is a general feature of bias-induced asymmetry: states at higher energy have more asymmetry due to the larger effect on the electrostatic environments from the applied bias voltage. As a result, we expect that finite-bias effects will become more prominent as experiments begin to probe materials with higher superconducting gaps [49]. To illustrate this we consider a second nanowire with $\Delta = \mu_{\text{wire}} = 1$ meV, $\mu_{\text{lead}} = 3$ meV, $V_{\text{dot}} = 2.2$ meV and $L_{\text{dot}} = 50$ nm. Now the energy of the Andreev bound state is about four times larger than the previous case. The corresponding two-terminal conductance in Fig. 4.5(a)-(c) shows significantly more asymmetry than in the system of Fig. 4.4.

Besides the energy of the Andreev bound states, the transparency of the tunnel barrier also influences the conductance asymmetry. In Fig. 4.6 we plot the peak height asymmetries as a function of the barrier width and height of a square barrier for a system with $\Delta = 0.25$ meV and $V_Z = 0$. As the barrier height and width are increased, the relative importance of the finite-bias modifications to the Hamiltonian decreases. Therefore the asymmetry decreases monotonically with both parameters, that is as the system is tuned deeper into the tunneling regime. This behaviour is independent of the details of the barrier and thus is useful in determining finite-bias effects are the source of conductance asymmetry.

While the conductance asymmetry displays the general trends outlined above, its precise magnitude depends on the microscopic details of the scattering region, in particular in the barrier transmission probabilities at $\pm V_{\text{bias}}$. Within the WKB approximation the normal-state transmission probability is given by

$$T(E, V_{\text{bias}}) \propto \exp\left[-\frac{2}{h}\int_{\text{barrier}} \sqrt{2m(E - V(x, V_{\text{bias}})}\right]. \tag{4.26}$$

The conductance through the barrier is therefore exponentially sensitive to the area of the barrier. In the case of a square barrier, these WKB areas are identical for $\pm V_{\text{bias}}$ due to the mirror symmetry of the barrier shape. However, if mirror symmetry in the barrier is broken, the effective WKB areas at negative and positive voltages become different, which further enhances the conductance asymmetry. As an example, we consider a system with a triangular barrier of height $V_{\text{barrier}} = 1.3$ meV, as illustrated in Fig. 4.3 (c)-(d)). In Fig. 4.4(c) we show the resulting conductance and see that it has larger particle-hole asymmetry than a system with a square barrier. This is more easily seen in Fig. 4.7(a)-(b) where we plot one-dimensional cuts of the conductance at $V_Z = 0$.

4.4.2. FINITE-BIAS NONLOCAL CONDUCTANCE IN A THREE-TERMINAL GEOMETRY

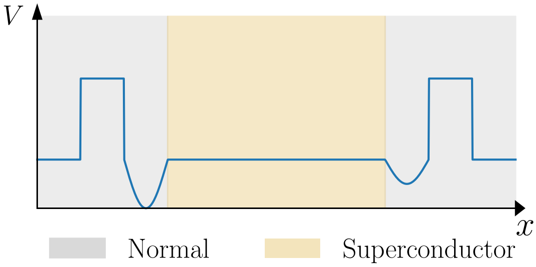

Figure 4.8: Schematic three-terminal superconducting device with bias dependent tunnel barriers and quantum dots.

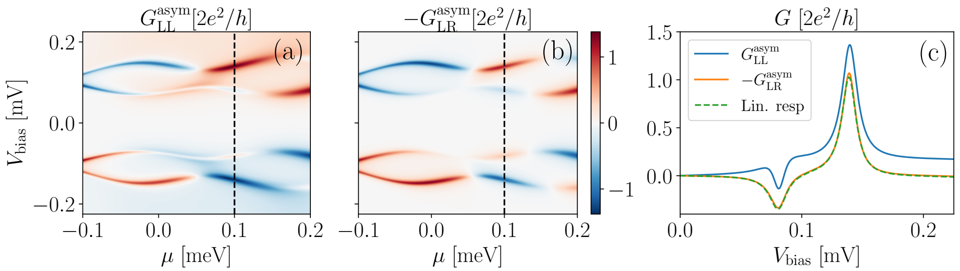

Figure 4.9: Anti-symmetric components of the (a) local conductance and (b) nonlocal conductance as a function of chemical potential and bias voltage. In panel (c) we show a one-dimensional cut of this data at fixed chemical potential (black dashed lines).

In three-terminal devices with two normal leads coupled to a grounded superconductor the conductance is given by

$$G = \begin{pmatrix} G_{\text{LL}} & G_{\text{LR}} \\ G_{\text{RL}} & G_{\text{RR}} \end{pmatrix} = \begin{pmatrix} \frac{\partial I_L}{\partial V_L} & \frac{\partial I_L}{\partial V_R} \\ \frac{\partial I_R}{\partial V_L} & \frac{\partial I_R}{\partial V_R} \end{pmatrix}. \tag{4.27}$$

Because electrons can tunnel across the normal leads, the reflection matrix is not unitary below the gap. Hence the local conductance G_{LL} is generally not particle-hole symmetric even in the linear response limit.

However, a recent theoretical work showed that the anti-symmetric components of local an nonlocal conductances are related by [30]

$$G_{LL}^{\text{asym}} = -G_{LR}^{\text{asym}}, \tag{4.28}$$

where

$$G_{\alpha\beta}^{\text{asym}} = G_{\alpha\beta}(V_{\text{bias}}) - G_{\alpha\beta}(-V_{\text{bias}}). \tag{4.29}$$

Follow-up experimental data observed excellent agreement with this symmetry relation at low-bias voltages, but only qualitative agreement at high bias voltages [39]. Additionally G_{LL}^{asym} and G_{LR}^{asym} exhibited different behaviours near crossings of subgap states: while the crossings are avoided in G_{LL}^{asym}, they are unavoided in G_{LR}^{asym}.

To investigate whether finite-bias effects can explain these discrepancies, we consider a finite-length semiconductor-superconductor nanowire with length $L_{\text{sc}} = 300$ nm. On the right side of the device, we add another dot potential with $L_{\text{dot}}^{\text{left}} = L_{\text{dot}}^{\text{right}} = 350$ nm, and attach a second normal lead, as shown schematically in Fig. 4.8. When a bias is applied on the left (right) side, we drop the voltage across the left (right) barrier as specified in Eq.(4.24). Both the left and right potential wells host subgap Andreev bound states whose energies oscillate with chemical potential and display avoided crossings. However, due to the oscillatory nature of the wavefunction there are points in the parameter space in which the energy splitting of the states vanishes, similar to Majorana oscillations [50]. To avoid this and obtain spectra that mimic those in [39] we break mirror symmetry and set $V_{\text{dot}}^{\text{left}} = 2 \cdot V_{\text{dot}}^{\text{right}} = 1$ meV. The remaining Hamiltonian parameters are the same as in Sec. 4.4.

In Fig. 4.9(a)-(b) we show the asymmetric components of the local and nonlocal conductances as a function of chemical potential and voltage, and in Fig. 4.9(c) we show a line cut at a fixed value of chemical potential. In accordance with the experimental results of [39], we observe G_{LL}^{asym} and G_{LR}^{asym} (orange and blue solid lines in Fig. 4.7(b)) show similar profiles qualitatively in general, but at the quantitative level, the deviation between them increases with the applied bias voltage, because the finite-bias effect is stronger at larger bias voltage as discussed in the previous sections. In contrast, the conductance components calculated under the linear response approximation are always equal to each other over the whole range of bias voltage (dashed line in Fig. 4.9(c)). However, our model does not capture the qualitative differences between G_{LL}^{asym} and G_{LR}^{asym} near avoided crossings. While this does not rule out finite-bias effects as the source of these discrepancies, it is also possible that they are caused by another physical mechanism.

4.5. SUMMARY AND DISCUSSION

In summary, we have shown that finite-bias effects in NS and NSN junctions can lead to significant deviations from linear response symmetries of the conductance matrix. In two-terminal NS junctions, the particle-hole symmetry between the conductance profiles at positive and negative voltages is broken, while for three-terminal NSN junctions, the equality between the asymmetric components of the local and nonlocal conductances no longer holds.

Although the exact values of the symmetry breaking depends on the details of the junction (e.g., the shape of the tunnel barrier and the magnitude of the superconducting gap), we find the asymmetry obeys two general qualitative trends. First, it decreases as the system is tuned deeper into the tunneling regime. Second, it grows with the applied bias voltage. As a result, finite-bias effects are more important in hybrid nanowires with a larger SC gap.

An important aspect about conductance asymmetries due to finite-bias effects is that they are not indicative of quasi-particle poisoning, unlike previously discussed mechanisms such as dissipation. Very recently, coupling of tunneling electrons to a phonon bath has also been predicted to give conductance asymmetries without quasiparticle poisoning [51]. Though originating from different physics, both mechanisms thus are not detrimental to Majorana qubits. Therefore, determining the source of conductance asymmetries is a helpful tool to predict qubit performance. The aforementioned trends allow to experimentally probe whether conductance asymmetries stem from finite-bias effects. As an example, if particle-hole symmetry of the conductance profiles in a two-terminal device is broken even when the bias voltage goes to zero [34, 36, 38], it is very likely that there are other mechanisms causing the symmetry breaking.

Finally, our treatment of the bias voltage dependence of the tunnel region is phenomenological. Future work could include computing finite-bias conductances with more realistic electrostatic potentials obtained by solving the self-consistent Schrödinger-Poisson equations [43, 52–54]. However, we expect that this will not change our qualitative findings.

4.A. CALCULATING THE INTEGRAL TERM OF THE CONDUCTANCE OF A SINGLE ANDREEV BOUND STATE

To compute the integral term we start from the approximate form of Eq. (4.15). The derivative of R_{he} with respect to V is

$$\frac{\partial R_{he}(E,V)}{\partial V} = R_{he}(E,V)\left\{\frac{2}{|t_e t_h|}\frac{\partial |t_e t_h|}{\partial V} - \frac{\pi^2 \frac{\partial}{\partial V}\left(|ut_e|^2 + |vt_h|^2\right)^2}{(E-E_0)^2 + \pi^2\left(|ut_e|^2 + |vt_h|^2\right)^2}\right\} \tag{4.30}$$

Because the integrand is sharply peaked at E_0 and we are interested in corrections near $eV_{\text{bias}} = E_0$ we approximate all derivatives of the tunneling rates as constant and evaluated

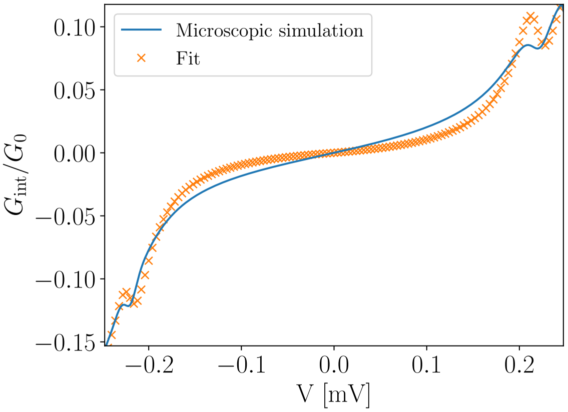

Figure 4.10: Blue line: integral term of the conductance for the system shown in Fig. 4.10(a) at $V_Z = 0$. Orange dots: fit to integral term expression obtained from two-level toy model.

at $E, eV_{\text{bias}} = E_0$. The contribution of the first term is then

$$\begin{aligned} &-\frac{2}{e|t_e t_h|}\frac{\partial|t_e t_h|}{\partial V}\bigg|_{\substack{E=E_0\\ V=-E_0/e}}\int_0^{-eV_{\text{bias}}} dE\,\frac{4\pi^2|uvt_e t_h|^2}{(E-E_0)^2+\pi^2\left(|ut_e|^2+|vt_h|^2\right)^2} = \\ &= -\frac{G_{\max}\cdot\text{FWHM}}{2G_0|t_e t_h|}\frac{\partial|t_e t_h|}{\partial V}\bigg|_{\substack{E=E_0\\ V=-E_0/e}}\left[\arctan\left(\frac{2(E-E_0)}{e\cdot\text{FWHM}}\right)\right]_0^{-eV_{\text{bias}}}, \end{aligned} \tag{4.31}$$

where we used the standard Lorentzian integral $\int dx\,\frac{a}{(x-x_0)^2+b^2} = \frac{a}{b}\arctan\left(\frac{x-x_0}{b}\right)$. The second term gives

$$\begin{aligned} &= \frac{\pi^2}{e}\frac{\partial}{\partial V}\left(|ut_e|^2+|vt_h|^2\right)^2\bigg|_{\substack{E=E_0\\ V=-E_0/e}}\int_0^{-eV_{\text{bias}}} dE\,\frac{4\pi^2|uvt_e t_h|^2}{\left((E-E_0)^2+\pi^2\left(|ut_e|^2+|vt_h|^2\right)^2\right)^2} = \\ &= \frac{2\pi|uvt_e t_h|^2}{e\left(|ut_e|^2+|vt_h|^2\right)^3}\frac{\partial\left(|ut_e|^2+|vt_h|^2\right)^2}{\partial V}\bigg|_{\substack{E=E_0\\ V=-E_0/e}} \\ &\times\left[\frac{\pi\left(|ut_e|^2+|vt_h|^2\right)(E-E_0)}{\left(\pi\left(|ut_e|^2+|vt_h|^2\right)\right)^2+(E-E_0)^2}+\arctan\left(\frac{2(E-E_0)}{e\cdot\text{FWHM}}\right)\right]_0^{-eV_{\text{bias}}} = \\ &= \frac{\pi^2 G_{\max}}{2G_0 e^2\cdot\text{FWHM}}\frac{\partial\left(|ut_e|^2+|vt_h|^2\right)^2}{\partial V}\bigg|_{\substack{E=E_0\\ V=-E_0/e}} \\ &\times\left[\frac{\frac{e\cdot\text{FWHM}}{2}(E-E_0)}{\left(\frac{e\cdot\text{FWHM}}{2}\right)^2+(E-E_0)^2}+\arctan\left(\frac{2(E-E_0)}{e\cdot\text{FWHM}}\right)\right]_0^{-eV_{\text{bias}}} \end{aligned} \tag{4.32}$$

Where we made use of the standard integral $\int dx\,\frac{a}{((x-x_0)^2+b^2)^2} = \frac{a}{2b^3}\left\{\frac{b(x-x_0)}{b^2+(x-x_0)^2}+\arctan\left(\frac{x-x_0}{b}\right)\right\}$. To test how well this expression works, we compute the integral term of the system shown in Fig. 4.4(a) at $V_Z = 0$ meV and fit it to

$$G_{\text{int}} = \begin{cases} \left[A \arctan\left(\frac{2(E-E_0)}{\text{FWHM}}\right) + B \frac{E-E_0}{\left(\frac{\text{FWHM}}{2}\right)^2 + (E-E_0)^2} \right]_0^{-eV_{\text{bias}}}, & V_{\text{bias}} < 0 \\ \left[C \arctan\left(\frac{2(E+E_0)}{\text{FWHM}}\right) + D \frac{E+E_0}{\left(\frac{\text{FWHM}}{2}\right)^2 + (E+E_0)^2} \right]_0^{-eV_{\text{bias}}}, & V_{\text{bias}} > 0 \end{cases}, \tag{4.33}$$

where A, B, C, D are free parameters and E_0 are FHWM are measured from the conductance profile. The resulting fit is shown in Fig. 4.10.

REFERENCES

[1] J. Alicea, *New directions in the pursuit of Majorana fermions in solid state systems,* Rep. Prog. Phys. **75**, 076501 (2012).

[2] M. Leijnse and K. Flensberg, *Introduction to topological superconductivity and Majorana fermions,* Semicond. Sci. Technol. **27**, 124003 (2012).

[3] C. Beenakker, *Search for Majorana fermions in superconductors,* Annu. Rev. Condens. Matter Phys. **4**, 113 (2013).

[4] T. D. Stanescu and S. Tewari, *Majorana fermions in semiconductor nanowires: fundamentals, modeling, and experiment,* J. Phys.: Condens. Matter **25**, 233201 (2013).

[5] J.-H. Jiang and S. Wu, *Non-Abelian topological superconductors from topological semimetals and related systems under the superconducting proximity effect,* J. Phys.: Condens. Matter **25**, 055701 (2013).

[6] S. R. Elliott and M. Franz, *Colloquium: Majorana fermions in nuclear, particle, and solid-state physics,* Rev. Mod. Phys. **87**, 137 (2015).

[7] M. Sato and S. Fujimoto, *Majorana fermions and topology in superconductors,* J. Phys. Soc. Jpn. **85**, 072001 (2016).

[8] M. Sato and Y. Ando, *Topological superconductors: a review,* Rep. Prog. Phys. **80**, 076501 (2017).

[9] R. Aguado, *Majorana quasiparticles in condensed matter,* Riv. Nuovo Cimento **40**, 523 (2017).

[10] R. M. Lutchyn, E. P. A. M. Bakkers, L. P. Kouwenhoven, P. Krogstrup, C. M. Marcus, and Y. Oreg, *Majorana zero modes in superconductor–semiconductor heterostructures,* Nat. Rev. Mater. **3**, 52 (2018).

[11] H. Zhang, D. E. Liu, M. Wimmer, and L. P. Kouwenhoven, *Next steps of quantum transport in Majorana nanowire devices,* Nature Communications **10**, 5128 (2019).

[12] S. Frolov, M. Manfra, and J. Sau, *Quest for topological superconductivity at superconductor-semiconductor interfaces,* arXiv:1912.11094 (2019).

[13] J. D. Sau, R. M. Lutchyn, S. Tewari, and S. Das Sarma, *Generic new platform for topological quantum computation using semiconductor heterostructures,* Phys. Rev. Lett. **104**, 040502 (2010).

[14] R. M. Lutchyn, J. D. Sau, and S. Das Sarma, *Majorana fermions and a topological phase transition in semiconductor-superconductor heterostructures,* Phys. Rev. Lett. **105**, 077001 (2010).

[15] Y. Oreg, G. Refael, and F. von Oppen, *Helical liquids and Majorana bound states in quantum wires,* Phys. Rev. Lett. **105**, 177002 (2010).

[16] J. D. Sau, S. Tewari, R. M. Lutchyn, T. D. Stanescu, and S. Das Sarma, *Non-Abelian quantum order in spin-orbit-coupled semiconductors: Search for topological Majorana particles in solid-state systems,* Phys. Rev. B **82**, 214509 (2010).

[17] V. Mourik, K. Zuo, S. M. Frolov, S. Plissard, E. P. A. M. Bakkers, and L. P. Kouwenhoven, *Signatures of Majorana fermions in hybrid superconductor-semiconductor nanowire devices,* Science **336**, 1003 (2012).

[18] A. Das, Y. Ronen, Y. Most, Y. Oreg, M. Heiblum, and H. Shtrikman, *Zero-bias peaks and splitting in an Al-InAs nanowire topological superconductor as a signature of Majorana fermions,* Nat. Phys. **8**, 887 (2012).

[19] M. T. Deng, C. L. Yu, G. Y. Huang, M. Larsson, P. Caroff, and H. Q. Xu, *Anomalous zero-bias conductance peak in a Nb-InSb nanowire-Nb hybrid device,* Nano Lett. **12**, 6414 (2012).

[20] H. O. H. Churchill, V. Fatemi, K. Grove-Rasmussen, M. T. Deng, P. Caroff, H. Q. Xu, and C. M. Marcus, *Superconductor-nanowire devices from tunneling to the multichannel regime: Zero-bias oscillations and magnetoconductance crossover,* Phys. Rev. B **87**, 241401(R) (2013).

[21] A. D. K. Finck, D. J. Van Harlingen, P. K. Mohseni, K. Jung, and X. Li, *Anomalous modulation of a zero-bias peak in a hybrid nanowire-superconductor device,* Phys. Rev. Lett. **110**, 126406 (2013).

[22] S. Albrecht, A. Higginbotham, M. Madsen, F. Kuemmeth, T. Jespersen, J. Nygård, P. Krogstrup, and C. Marcus, *Exponential protection of zero modes in Majorana islands,* Nature **531**, 206 (2016).

[23] J. Chen, P. Yu, J. Stenger, M. Hocevar, D. Car, S. R. Plissard, E. P. A. M. Bakkers, T. D. Stanescu, and S. M. Frolov, *Experimental phase diagram of zero-bias conductance peaks in superconductor/semiconductor nanowire devices,* Science Advances **3** (2017), 10.1126/sciadv.1701476.

[24] M. T. Deng, S. Vaitiekenas, E. B. Hansen, J. Danon, M. Leijnse, K. Flensberg, J. Nygård, P. Krogstrup, and C. M. Marcus, *Majorana bound state in a coupled quantum-dot hybrid-nanowire system,* Science **354**, 1557 (2016).

[25] H. Zhang, Ö. Gül, S. Conesa-Boj, M. Nowak, M. Wimmer, K. Zuo, V. Mourik, F. K. de Vries, J. van Veen, M. W. A. de Moor, J. D. S. Bommer, D. J. van Woerkom, D. Car, S. R. Plissard, E. P. A. M. Bakkers, M. Quintero-Pérez, M. C. Cassidy, S. Koelling, S. Goswami, K. Watanabe, T. Taniguchi, and L. P. Kouwenhoven, *Ballistic superconductivity in semiconductor nanowires,* Nature Communications **8**, 16025 EP (2017).

[26] Ö. Gül, H. Zhang, J. D. S. Bommer, M. W. A. de Moor, D. Car, S. R. Plissard, E. P. A. M. Bakkers, A. Geresdi, K. Watanabe, T. Taniguchi, and L. P. Kouwenhoven, *Ballistic Majorana nanowire devices,* Nat. Nanotechnol. **13**, 192 (2018).

[27] F. Nichele, A. C. C. Drachmann, A. M. Whiticar, E. C. T. O'Farrell, H. J. Suominen, A. Fornieri, T. Wang, G. C. Gardner, C. Thomas, A. T. Hatke, P. Krogstrup, M. J. Manfra, K. Flensberg, and C. M. Marcus, *Scaling of Majorana zero-bias conductance peaks,* Phys. Rev. Lett. **119**, 136803 (2017).

[28] T. O. Rosdahl, A. Vuik, M. Kjaergaard, and A. R. Akhmerov, *Andreev rectifier: A nonlocal conductance signature of topological phase transitions,* Phys. Rev. B **97** (2018), 10.1103/physrevb.97.045421.

[29] Y.-H. Lai, J. D. Sau, and S. D. Sarma, *Presence versus absence of end-to-end nonlocal conductance correlations in Majorana nanowires: Majorana bound states versus Andreev bound states,* Phys. Rev. B **100** (2019), 10.1103/physrevb.100.045302.

[30] J. Danon, A. B. Hellenes, E. B. Hansen, L. Casparis, A. P. Higginbotham, and K. Flensberg, *Nonlocal Conductance Spectroscopy of Andreev Bound States: Symmetry Relations and BCS Charges,* Phys. Rev. Lett. **124** (2020), 10.1103/physrevlett.124.036801.

[31] S. Datta, *Electronic transport in mesoscopic systems* (Cambridge university press, 1997).

[32] G. B. Lesovik, A. L. Fauchère, and G. Blatter, *Nonlinearity in normal-metal–superconductor transport: Scattering-matrix approach,* Phys. Rev. B **55**, 3146 (1997).

[33] I. Martin and D. Mozyrsky, *Nonequilibrium theory of tunneling into a localized state in a superconductor,* Phys. Rev. B **90** (2014), 10.1103/physrevb.90.100508.

[34] F. Nichele, A. C. Drachmann, A. M. Whiticar, E. C. O'Farrell, H. J. Suominen, A. Fornieri, T. Wang, G. C. Gardner, C. Thomas, A. T. Hatke, P. Krogstrup, M. J. Manfra, K. Flensberg, and C. M. Marcus, *Scaling of Majorana Zero-Bias Conductance Peaks,* Phys. Rev. Lett. **119** (2017), 10.1103/physrevlett.119.136803.

[35] Önder Gül, H. Zhang, J. D. S. Bommer, M. W. A. de Moor, D. Car, S. R. Plissard, E. P. A. M. Bakkers, A. Geresdi, K. Watanabe, T. Taniguchi, and L. P. Kouwenhoven, *Ballistic Majorana nanowire devices,* Nature Nanotechnology **13**, 192 (2018).

[36] M.-T. Deng, S. Vaitiekėnas, E. Prada, P. San-Jose, J. Nygård, P. Krogstrup, R. Aguado, and C. M. Marcus, *Nonlocality of Majorana modes in hybrid nanowires,* Phys. Rev. B **98** (2018), 10.1103/physrevb.98.085125.

[37] J. D. Bommer, H. Zhang, Önder Gül, B. Nijholt, M. Wimmer, F. N. Rybakov, J. Garaud, D. Rodic, E. Babaev, M. Troyer, D. Car, S. R. Plissard, E. P. Bakkers, K. Watanabe, T. Taniguchi, and L. P. Kouwenhoven, *Spin-Orbit Protection of Induced Superconductivity in Majorana Nanowires,* Phys. Rev. Lett. **122** (2019), 10.1103/physrevlett.122.187702.

[38] J. Chen, B. Woods, P. Yu, M. Hocevar, D. Car, S. Plissard, E. Bakkers, T. Stanescu, and S. Frolov, *Ubiquitous Non-Majorana Zero-Bias Conductance Peaks in Nanowire Devices,* Phys. Rev. Lett. **123** (2019), 10.1103/physrevlett.123.107703.

[39] G. Ménard, G. Anselmetti, E. Martinez, D. Puglia, F. Malinowski, J. Lee, S. Choi, M. Pendharkar, C. Palmstrøm, K. Flensberg, C. Marcus, L. Casparis, and A. Higginbotham, *Conductance-Matrix Symmetries of a Three-Terminal Hybrid Device,* Phys. Rev. Lett. **124** (2020), 10.1103/physrevlett.124.036802.

[40] C.-X. Liu, J. D. Sau, T. D. Stanescu, and S. D. Sarma, *Andreev bound states versus Majorana bound states in quantum dot-nanowire-superconductor hybrid structures: Trivial versus topological zero-bias conductance peaks,* Phys. Rev. B **96** (2017), 10.1103/physrevb.96.075161.

[41] M. Ruby, F. Pientka, Y. Peng, F. von Oppen, B. W. Heinrich, and K. J. Franke, *Tunneling processes into localized subgap states in superconductors,* Phys. Rev. Lett. **115**, 087001 (2015).

[42] L. I. Glazman and A. V. Khaetskii, *Nonlinear Quantum Conductance of a Lateral Microconstraint in a Heterostructure,* Europhysics Letters (EPL) **9**, 263 (1989).

[43] T. Christen and M. Büttiker, *Gauge-invariant nonlinear electric transport in mesoscopic conductors,* Europhysics Letters (EPL) **35**, 523 (1996).

[44] M. Büttiker, *Four-Terminal Phase-Coherent Conductance,* Phys. Rev. Lett. **57**, 1761 (1986).

[45] A. Melo, C.-X. Liu, P. Rożek, T. O. Rosdahl, and M. Wimmer, *Conductance asymmetries in mesoscopic superconducting devices due to finite bias,* (2020).

[46] N. S. Wingreen, A.-P. Jauho, and Y. Meir, *Time-dependent transport through a mesoscopic structure,* Phys. Rev. B **48**, 8487 (1993).

[47] N. K. Patel, J. T. Nicholls, L. Martn-Moreno, M. Pepper, J. E. F. Frost, D. A. Ritchie, and G. A. C. Jones, *Evolution of half plateaus as a function of electric field in a ballistic quasi-one-dimensional constriction,* Phys. Rev. B **44**, 13549 (1991).

[48] C. W. Groth, M. Wimmer, A. R. Akhmerov, and X. Waintal, *Kwant: a software package for quantum transport,* New Journal of Physics **16**, 063065 (2014).

[49] T. Kanne, M. Marnauza, D. Olsteins, D. J. Carrad, J. E. Sestoft, J. de Bruijckere, L. Zeng, E. Johnson, E. Olsson, K. Grove-Rasmussen, and J. Nygård, *Epitaxial Pb on InAs nanowires,* (2020).

[50] S. D. Sarma, J. D. Sau, and T. D. Stanescu, *Splitting of the zero-bias conductance peak as smoking gun evidence for the existence of the Majorana mode in a superconductor-semiconductor nanowire,* Phys. Rev. B **86** (2012), 10.1103/physrevb.86.220506.

[51] F. Setiawan and J. D. Sau, *Particle-hole asymmetry of subgap conductances in superconductors without quasiparticle poisoning,* (2020), arXiv:2007.15648 .

[52] E. Forsberg and J.-O. J. Wesström, *Self-consistent simulations of mesoscopic devices operating under a finite bias,* Solid-State Electronics **48**, 1147 (2004).

[53] A. Vuik, D. Eeltink, A. R. Akhmerov, and M. Wimmer, *Effects of the electrostatic environment on the Majorana nanowire devices,* New Journal of Physics **18**, 033013 (2016).

[54] P. Armagnat, A. Lacerda-Santos, B. Rossignol, C. Groth, and X. Waintal, *The self-consistent quantum-electrostatic problem in strongly non-linear regime,* SciPost Physics **7** (2019), 10.21468/scipostphys.7.3.031.

5

MULTIPLET SUPERCURRENT IN JOSEPHSON TUNNELING CIRCUITS

This chapter has been previously published as André Melo, Valla Fatemi, Anton R. Akhmerov, *Multiplet supercurrent in Josephson tunneling circuits*, SciPost Phys. 12, 017 (2022) .

The DC Josephson effect allows coherent transport of Cooper pairs across two-terminal superconducting junctions at zero voltage [1]. At finite DC voltages the phase difference across the junction advances linearly in time, resulting in a pure AC supercurrent. A dissipative DC current may also arise due to multiple Andreev reflections [2]. However, charge transfers across terminals of a voltage-biased junction cost energy and thus no DC supercurrent can flow.

Junctions with additional terminals biased at commensurate voltages support energy-conserving processes that transfer charge between multiple electrodes. The simplest setup where this can occur is a three-terminal junction, where two voltage-biased terminals each transfer n_1 and n_2 Cooper pairs to a grounded terminal. At commensurate voltages $2en_1V_1 = -2en_2V_2$ this is a coherent and energy-conserving process that allows DC supercurrent. Several experimental works reported increased conductance at commensurate voltages as a signature of multiplet supercurrent in Josephson elements with weak links made of diffusive normal metals [3], InAs nanowires [4], and graphene [5].

So far, theoretical interpretations of these experiments rely on Andreev physics associated with highly transparent superconductor-normal-superconductor (SNS) junctions. In particular, the normal region must host nonlocal Andreev states that extend to multiple terminals and mediate transport of charge through nonlocal Andreev processes [6–9] (see Fig. 5.1(a)). This mechanism is nontrivial because it is not guaranteed that a single state propagates to all three junctions, which may imply that multiplet supercurrent is a fragile phenomenon requiring fine tuning of microscopic aspects of the normal scattering region.

One may ask if this delicate microscopic process is the only mechanism that admits multiplet supercurrent. We draw inspiration from a problem in a similar context: multi-terminal SNS Josephson junctions were proposed as a platform for non-trivial band topology, where the superconducting phases play the role of crystal momenta [10]. Recent works showed that tunnel Josephson junction circuits are capable of encoding the same physics in collective electronic modes, rather than the fermionic degrees of freedom in the multi-terminal weak link [11, 12].

In this work, we show that voltage-biased circuits of Josephson tunnel junctions also generate multiplet supercurrent, and we elucidate two types of contributions: an adiabatic component and a quantum geometric component. In contrast with its SNS counterpart, these circuits mediate the transport of multiplets through the collective behavior of the superconducting circuit, rather than microscopic multi-terminal Andreev processes. Furthermore, our proposal is experimentally tractable because tunnel junctions are standard building blocks of experimental superconducting devices.

We begin by analyzing the minimal tunneling circuit in Fig. 5.1(b) in the zero charging energy limit, $E_C = 0$, which may be referred to as the classical limit of the circuit. We assume that damping in the circuit allows treating the evolution of φ adiabatically. The circuit energy as a function of the superconducting phases is $E(\varphi, \phi_1, \phi_2) = -E_{J,0}\cos(\varphi) - E_{J,1}\cos(\phi_1 - \varphi) - E_{J,2}\cos(\phi_1 - \varphi)$, where the phases of the voltage-biased terminals evolve as $\dot{\phi}_i = V_i/\Phi_0$, where $\Phi_0 = \hbar/2e$ is the reduced magnetic flux quantum. Minimizing the circuit energy E with respect to φ for fixed (ϕ_1, ϕ_2) gives the condition

$$\tan(\varphi) = \frac{E_{J,1}\sin(\phi_1) + E_{J,2}\sin(\phi_2)}{E_{J,0} + E_{J,1}\cos(\phi_1) + E_{J,2}\cos(\phi_2)} \tag{5.1}$$

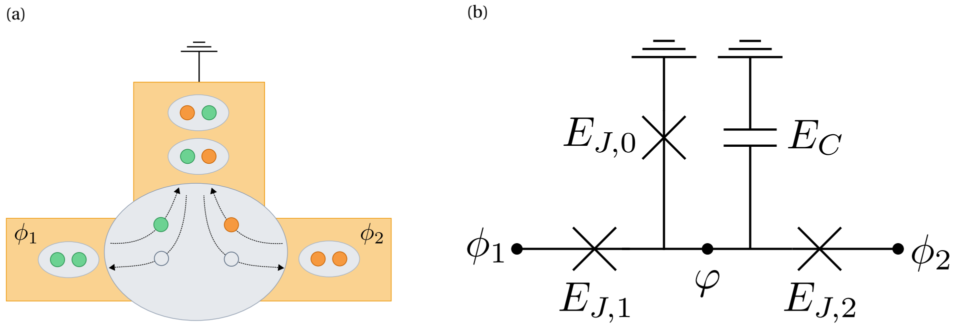

Figure 5.1: Superconducting devices that carry multiplet supercurrent at commensurate DC voltages. (a) A high transparency three-terminal Josephson junction supports multiplet supercurrent through non-local Andreev processes. When voltages applied to terminals 1 and 2 satisfy $V_1 = -V_2$, each biased terminal may transfer one Cooper pair to the grounded terminal through crossed Andreev reflections, resulting in quartet supercurrent. (b) A Josephson tunneling circuit also supports multiplet supercurrents. Even when the central island has a large charging energy, multiplet supercurrent still flows despite being carried only by single Cooper pair transfers.

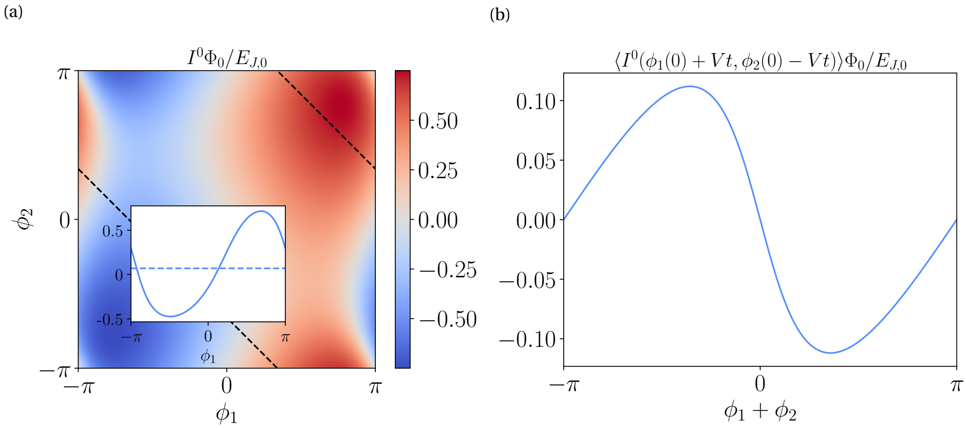

Figure 5.2: Currents across the $E_{J,0}$ junction in the circuit of Fig. 5.1 with $E_{J,1} = E_{J,0}/2, E_{J,2} = E_{J,0}/4, E_C = 0$. (a) Instantaneous current at fixed ϕ_1, ϕ_2. The inset shows the current along the quartet line $\phi_1 + \phi_2 = -1$ (black dashed line). Since the average (blue dashed line) is finite there is a quartet DC supercurrent. (b) Average current along quartet trajectories with different phase offsets.

We then obtain the supercurrent flowing to ground using the Josephson relation $I^0(\phi_1, \phi_2) = E_{J,0} \sin(\varphi)/\Phi_0$. In Fig. 5.2(a) we plot $I^0(\phi_1, \phi_2)$ for a circuit with $E_{J,1} = E_{J,0}/2$ and $E_{J,2} = E_{J,0}/4$. Because the supercurrent is a periodic function of both ϕ_1 and ϕ_2 it admits a Fourier expansion

$$I^0(\phi_1, \phi_2) = \sum_{n,m} I^0_{nm} \sin(n\phi_1 + m\phi_2). \tag{5.2}$$

The n, m harmonic in Eq. (5.2) is associated with transferring n (m) Cooper pairs from terminal 1 (2) and $n+m$ to the reference terminal [8]. If terminals 1 and 2 are biased with commensurate DC voltages $nV_1 + mV_2 = 0$, then harmonics with the ratio n/m become resonant. Thus, a net DC current is produced if any of those Fourier components are nonzero, $I^0_{nm} \neq 0$. In the following we focus on the quartet supercurrent appearing when $V_1 + V_2 = 0$, i.e. when $n = m = 1$; however, calculations for higher harmonics are analogous. To check whether the circuit supports quartet supercurrent we plot the average current $\langle I^0(\phi_1(0) + Vt, \phi_2(0) - Vt)\rangle$ as a function of the phase offset in Fig. 5.2(b). We observe that the average is finite as long as the phase offset $\phi_1 + \phi_2 \pmod{2\pi} \not\in \{0, \pi\}$, confirming that the circuit carries quartet supercurrent proportional to the critical current of the junction array.

We now investigate the role of quantum fluctuations in the circuit by including the charging energy of the superconducting island. The circuit Hamiltonian then reads

$$H = E_C(\hat{n} - n_g)^2 - E_{J,0}\cos(\hat{\varphi}) - E_{J,1}\cos(\hat{\varphi} - \phi_1) - E_{J,2}\cos(\hat{\varphi} - \phi_2), \tag{5.3}$$

where $\hat{n}$ is the number of Cooper pairs in the island, n_g is the island offset charge, and $\hat{\varphi}$ is now promoted to a Hermitian operator conjugate to $\hat{n}$. In the adiabatic approximation in which the bias voltages are small enough to prevent Landau-Zener transition [13], the current flowing to ground equals

$$I^0_{\text{adiab.}} = \frac{1}{\Phi_0}\left(\frac{\partial E}{\partial \phi_1} + \frac{\partial E}{\partial \phi_2}\right), \tag{5.4}$$

where E is the energy of the ground state. In Fig. 5.3(a) we show the resulting current in a circuit with $E_C = 30E_{J,0}$ and $n_g = 0$. We observe a similar functional dependence to that of the classical supercurrent in Fig. 5.1(a), indicating that the quartet supercurrent persists in the presence of large charge fluctuations. At the same time, the magnitude of the supercurrent is significantly smaller than in the classical limit. In order to more systematically determine the effect of a large charging energy on the magnitude of supercurrent, we analytically compute $I^0(\phi_1, \phi_2)$ in the high charging energy limit. Near the charge degeneracy point $n_g = 0.5$ the system's dynamics are restricted to the two lowest charge states $|0\rangle$ and $|1\rangle$. The low-lying spectrum is then well approximated by the effective two-level Hamiltonian

$$H = \begin{bmatrix} 0 & \frac{1}{2}\left(E_{J,0} + E_{J,1}e^{i\phi_1} + E_{J,2}e^{i\phi_2}\right) \\ \frac{1}{2}\left(E_{J,0} + E_{J,1}e^{-i\phi_1} + E_{J,2}e^{-i\phi_2}\right) & E_1 \end{bmatrix}, \tag{5.5}$$

where we set the energy of $|0\rangle$ to zero and $E_1 = E_C(1 - 2n_g)$ is the energy of $|1\rangle$. The ground state energy reads

$$E = \frac{1}{2}\left(E_1 - \sqrt{E_1^2 + |E_{J,0} + E_{J,1}e^{i\phi_1} + E_{J,2}e^{i\phi_2}|^2}\right). \tag{5.6}$$

Using Eq. (5.4) we obtain the supercurrent flowing to ground:

$$I^0 = \frac{E_{J,0}(E_{J,1}\sin\phi_1 + E_{J,2}\sin\phi_2)}{2\sqrt{E_1^2 + |E_{J,0} + E_{J,1}e^{i\phi_1} + E_{J,2}e^{i\phi_2}|^2}}. \tag{5.7}$$

When $n_g \neq 0.5$, the charge degeneracy is broken ($E_1 \neq 0$). This suppresses charge transfers to the island and thus the supercurrent vanishes as $E_C \to \infty$ (blue line in Fig. 5.3(b)). However, at the charge degeneracy point $E_1 = 0$ the supercurrent $I^0(\phi_1, \phi_2)$ becomes

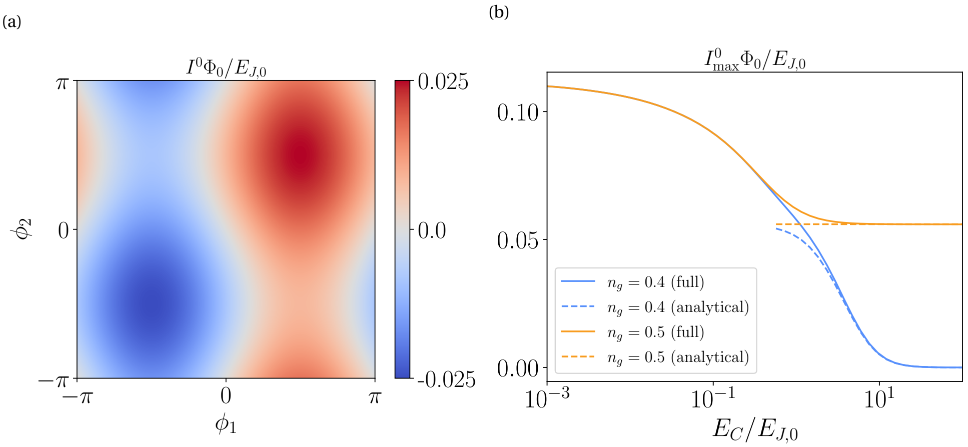

Figure 5.3: (a) Instantaneous current across the $E_{J,0}$ junction in the circuit of Fig. 5.1(a) with $E_{J,1} = E_{J,0}/2, E_{J,2} = E_{J,0}/4, E_C = 30E_{J,0}, n_g = 0$. (b) critical quartet supercurrent: the current I_0 maximized over the average phase of the electrodes $\max_{\phi_1+\phi_2}\langle I^0(\phi_1(0)+Vt, \phi_2(0)-Vt)\rangle$. When $n_g = 1/2$ charge states $|0\rangle$ and $|1\rangle$ are degenerate, allowing quartet supercurrent to flow with single Cooper pair transfers. The solid lines are obtained by numerically diagonalizing the full Hamiltonian (5.3), while the dashed lines are given by the approximate analytical expression (5.7), valid in the high E_C limit.

independent of E_C (orange line in Fig. 5.3(b)). Remarkably, this implies that the quartet supercurrent is carried only by sequential Cooper pair transfers.

When the bias voltages are commensurate, the closed trajectory in the ϕ_1, ϕ_2 parameter space results in the accumulation of a Berry phase with each cycle. While ϕ_1, ϕ_2 vary with time, the instantaneous geometric contribution to the current is [10, 14, 15]

$$I^0_{\text{Berry}} = -2e\left(\Omega_{12}\dot{\phi}_1 + \Omega_{21}\dot{\phi}_2\right), \tag{5.8}$$

where the Berry curvature of the ground state $|\psi\rangle$ is given by

$$\Omega_{\alpha\beta} = -2\text{Im}\left\langle \frac{\partial\psi}{\partial\phi_\alpha}\middle|\frac{\partial\psi}{\partial\phi_\beta}\right\rangle. \tag{5.9}$$

The quartet supercurrent then arises from the average of I^0_{Berry} along a trajectory in phase space satisfying $\dot{\phi}_1 = -\dot{\phi}_2 = V/\Phi_0$, for which we simplify the instantaneous geometric current to

$$I^0_{\text{Berry}} = -\frac{(4e)^2}{h}\pi\Omega_{12}V \tag{5.10}$$

where we used the relation $\Omega_{12} = -\Omega_{21}$. In contrast with the adiabatic term of Eq. (5.4), this current scales proportionally with the applied voltage. This allows the possibility of separately identifying the adiabatic and geometric parts.

The geometric quartet supercurrent requires additional conditions on the circuit's parameters. At charge-inversion invariant points $n_g \in \{0, 1/2\}$, the Hamiltonian (5.3) is both time-reversal and charge-inversion symmetric [11] and hence the Berry curvature vanishes. Away from these points the Berry curvature becomes finite; however, if $E_{J,1} =$

$E_{J,2}$ it is antisymmetric along the quartet trajectories, i.e. $\Omega(\phi_1,\phi_2) = -\Omega(\phi_2,\phi_1)$. As a result, the average Berry curvature along a quartet trajectory $(\phi_1(0)+Vt, \phi_2(0)-Vt)$ vanishes regardless of the offset phase $\phi_1+\phi_2$. When the Josephson energies differ (i.e. $E_{J,1} \neq E_{J,2}$), the Berry curvature landscape 'shears', resulting in a finite average on a quartet trajectory. As an example, in Fig. 5.4 we show the Berry curvature of a circuit with $E_C = E_{J_0}$ and $n_g = 0.7$. We observe that the average $\langle \Omega_{12}(\phi_1(0)+Vt, \phi_2(0)-Vt)\rangle$ is finite provided that $\phi_1+\phi_2 \pmod{2\pi} \notin \{0,\pi\}$, resulting in the quantum geometric contribution to the quartet supercurrent.

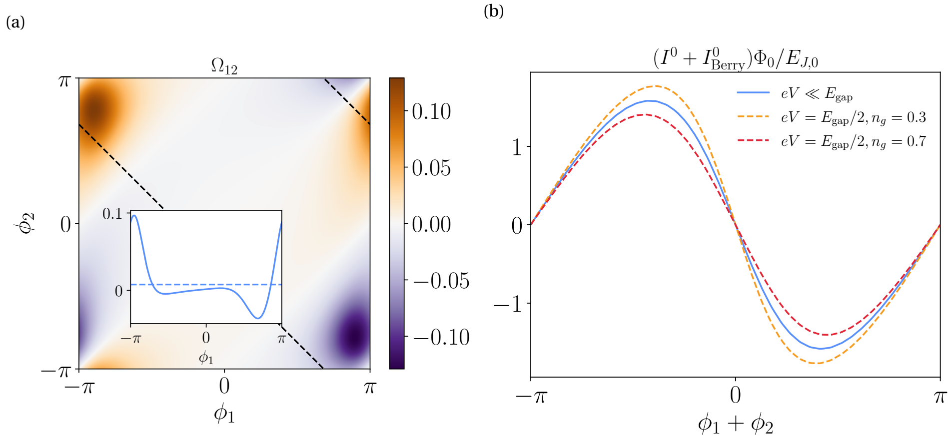

Figure 5.4: (a) Berry curvature of the ground state of the circuit in Fig. 5.1(b) with $E_{J,1} = E_{J,0}/2, E_{J,2} = E_{J,0}/4, E_C = E_{J,0}$ and $n_g = 0.7$. The inset shows a cut along $\phi_1+\phi_2 = -1$ (black dashed line). Because the average (blue dashed line) is finite, the quartet supercurrent has a geometric contribution. (b) Quartet current-phase relation of the circuit in (a) with geometric corrections. The scale of the voltage is set by the minimum spectral gap E_{gap} over the Brillouin zone. Reflecting n_g about 0.5 flips the sign of the Berry curvature and hence of the geometric component of the supercurrent.

Our proposal to produce multiplet supercurrent has two main advantages over its existing SNS counterpart. First, SNS devices require tuning wave functions of Andreev bound states that depend strongly on the microscopic details of the junction. Additionally, fabricating multi-terminal junctions is nontrivial [16]. In contrast, fabricating tunneling circuits with designed parameters (charging and Josephson energies) is a relatively routine procedure. Finally, SNS junctions have significantly larger dissipation due to the low resistance of the normal region [17].

Turning to existing experimental work [3–5, 16], we note that the most qualitative signatures of SNS-based multiplet supercurrents are, to the best of our knowledge, indistinguishable from those of tunnel-based junctions. Furthermore, it is known that the conventional Cooper pair transistor in the deep charging regime ($E_C \gg E_J$) has the same Hamiltonian as a single-level quantum dot with weak coupling strengths $\Gamma \ll \Delta$ to a pair of superconducting reservoirs [18]. In this analogy between the SNS and SIS devices, Γ relates to E_J, and a level offset energy relates to offset charge. The same analogy extends to the multi-terminal case [19]. Such dots would exhibit the same kind of multiplet supercurrent described in our work. On the other hand, multiplet processes that entangle

Cooper pairs from different leads require intermediate states with broken Cooper pairs, and thus they would be suppressed by factors of Γ/Δ. Many of the Andreev levels of experimental multiterminal and multichannel SNS devices may be weakly coupled to the superconducting reservoirs, and those levels would predominantly contribute the kind of multiplet supercurrent described here. Thus, our results suggest that the multiplet supercurrent observed in SNS devices may have an alternative contribution arising from local Cooper pair transfers.

Moving forward, a question relevant for experimental implementation is how this device performs in a realistic environment including load circuit and environmental noise [20]. Another interesting avenue of further investigation would be to design tunneling circuits that allow coherent control of the collective motion of quartets. Such a device could serve as a building block for parity-protected $\cos 2\varphi$ electromagnetic qubits [21–23].

ACKNOWLEDGEMENTS

The authors acknowledge useful discussions with Radoica Draškić, and V.F. acknowledges useful discussions with Nicholas Frattini and Pavel D. Kurilovich.

Data availability The code used to generate the figures is available on Zenodo [24].

REFERENCES

[1] B. Josephson, *Supercurrents through barriers,* Advances in Physics **14**, 419 (1965).

[2] T. Klapwijk, G. Blonder, and M. Tinkham, *Explanation of subharmonic energy gap structure in superconducting contacts,* Physica B+C **109-110**, 1657 (1982).

[3] A. H. Pfeffer, J. E. Duvauchelle, H. Courtois, R. Mélin, D. Feinberg, and F. Lefloch, *Subgap structure in the conductance of a three-terminal Josephson junction,* Physical Review B **90** (2014), 10.1103/physrevb.90.075401.

[4] Y. Cohen, Y. Ronen, J.-H. Kang, M. Heiblum, D. Feinberg, R. Mélin, and H. Shtrikman, *Nonlocal supercurrent of quartets in a three-terminal Josephson junction,* Proceedings of the National Academy of Sciences **115**, 6991 (2018).

[5] K.-F. Huang, Y. Ronen, R. Mélin, D. Feinberg, K. Watanabe, T. Taniguchi, and P. Kim, *Interference of Cooper quartet Andreev bound states in a multi-terminal graphene-based Josephson junction,* arXiv preprint arXiv:2008.03419 (2020), arXiv:2008.03419.

[6] J. C. Cuevas and H. Pothier, *Voltage-induced Shapiro steps in a superconducting multiterminal structure,* Physical Review B **75** (2007), 10.1103/physrevb.75.174513.

[7] A. Freyn, B. Douçot, D. Feinberg, and R. Mélin, *Production of Nonlocal Quartets and Phase-Sensitive Entanglement in a Superconducting Beam Splitter,* Physical Review Letters **106** (2011), 10.1103/physrevlett.106.257005.

[8] R. Mélin, D. Feinberg, H. Courtois, C. Padurariu, A. Pfeffer, J. E. Duvauchelle, F. Lefloch, T. Jonckheere, J. Rech, T. Martin, and B. Doucot, *D.C. Josephson transport*

by quartets and other Andreev resonances in superconducting bijunctions, Journal of Physics: Conference Series **568**, 052006 (2014).

[9] J.-D. Pillet, V. Benzoni, J. Griesmar, J.-L. Smirr, and Ç. O. Girit, *Nonlocal Josephson Effect in Andreev Molecules,* Nano Letters **19**, 7138 (2019).

[10] R.-P. Riwar, M. Houzet, J. S. Meyer, and Y. V. Nazarov, *Multi-terminal Josephson junctions as topological matter,* Nature Communications **7** (2016), 10.1038/ncomms11167.

[11] V. Fatemi, A. R. Akhmerov, and L. Bretheau, *Weyl josephson circuits,* Physical Review Research **3** (2021), 10.1103/physrevresearch.3.013288.

[12] T. Herrig and R.-P. Riwar, *A "minimal" topological quantum circuit,* arXiv preprint arXiv:2012.10655 (2020), arXiv:2012.10655.

[13] C. Zener, *Non-adiabatic crossing of energy levels,* Proceedings of the Royal Society of London. Series A, Containing Papers of a Mathematical and Physical Character **137**, 696 (1932).

[14] M. Aunola and J. J. Toppari, *Connecting Berry's phase and the pumped charge in a Cooper pair pump,* Physical Review B **68** (2003), 10.1103/physrevb.68.020502.

[15] R. Leone and L. Lévy, *Topological quantization by controlled paths: Application to Cooper pairs pumps,* Physical Review B **77** (2008), 10.1103/physrevb.77.064524.

[16] N. Pankratova, H. Lee, R. Kuzmin, K. Wickramasinghe, W. Mayer, J. Yuan, M. G. Vavilov, J. Shabani, and V. E. Manucharyan, *Multiterminal Josephson Effect,* Physical Review X **10** (2020), 10.1103/physrevx.10.031051.

[17] D. Averin and A. Bardas, *ac Josephson Effect in a Single Quantum Channel,* Physical Review Letters **75**, 1831 (1995).

[18] G. Wendin and V. S. Shumeiko, *Josephson transport in complex mesoscopic structures,* Superlattices and microstructures **20**, 569 (1996).

[19] R. L. Klees, G. Rastelli, J. C. Cuevas, and W. Belzig, *Microwave spectroscopy reveals the quantum geometric tensor of topological josephson matter,* Physical Review Letters **124**, 197002 (2020).

[20] X. You, J. A. Sauls, and J. Koch, *Circuit quantization in the presence of time-dependent external flux,* Physical Review B **99** (2019), 10.1103/physrevb.99.174512.

[21] M. T. Bell, J. Paramanandam, L. B. Ioffe, and M. E. Gershenson, *Protected Josephson Rhombus Chains,* Physical Review Letters **112** (2014), 10.1103/physrevlett.112.167001.

[22] W. C. Smith, A. Kou, X. Xiao, U. Vool, and M. H. Devoret, *Superconducting circuit protected by two-Cooper-pair tunneling,* npj Quantum Information **6** (2020), 10.1038/s41534-019-0231-2.

[23] T. Larsen, M. Gershenson, L. Casparis, A. Kringhøj, N. Pearson, R. McNeil, F. Kuemmeth, P. Krogstrup, K. Petersson, and C. Marcus, *Parity-Protected Superconductor-Semiconductor Qubit,* Physical Review Letters **125** (2020), 10.1103/physrevlett.125.056801.

[24] A. Melo, V. Fatemi, and A. Akhmerov, *Multiplet supercurrent in Josephson tunneling circuits,* (2021).

ACKNOWLEDGMENTS

The work contained in this thesis would not have been possible without the support of the amazing people I worked with. **Anton and Michael**, I am deeply grateful that you took me on as your PhD student, for your wonderful supervision and for always caring about my well-being. Your commitment to open science, along with your constant strive to adopt new practices for the group, are admirable. I can sincerely say that I could not have asked for a better place to do my PhD. **Anton**, working closely with you has been a privilege. Seeing how you approach physics, coding, and writing has had an immeasurable influence on how I approach problems. PhDs inevitably have low points; in those periods, your endless curiosity and enthusiasm always restored my joy for doing physics. To the other **members of Quantum Tinkerer**, thank you for being such a welcoming and supportive bunch, for all the whiteboard brainstorms, bouldering sessions and beer runs. A special thanks to **Rik** for reviewing the Dutch version of the thesis summary. **Alex, Kim, and Tómas**, thank you for always taking time off of your day to chat whenever I dropped by your office with random questions. When I started my PhD, I was completely new to quantum transport and Majorana physics, and I benefited immensely from our discussions. **Valla**, it's been great to collaborate and learn from you. I'm continually impressed by how you manage to juggle experimental and theoretical physics, and I'm excited to see your new lab grow. **Hristo**, thank you for dropping by the office and making me go outside for much-needed and healthy coffee breaks. I hope Switzerland is treating you well. **Tanko** and **Carlos**, your work was instrumental in the projects you took on during your master's thesis. I'm very happy that you're now both pursuing PhDs, and I look forward to seeing your scientific career unfold. **Francesco** and **Nate**, thank you for your supervision during my internship at IBM and our insightful weekly discussions.

For the members of Mastermind, a few special words are in order. You're all amazing guys and I'm proud to call you friends. **Cal**, your endless support, words of wisdom, and friendship made grey Dutch days seem filled with color. Thank you for everything, and let's go for those million years. **Capinha**, no matter where we are, talking to you always makes me feel at home. Thank you for your kindness, listening ear, infinite times hosting me in Lisbon, and all the jam sessions. **Jaques**, your tenacity and drive are inspirational, and I've learned so much from you over the years. Traveling with you and working on endless side projects/hackathons together are some of my most cherished memories.

Damianos and **Guan**, can you believe it's been more than 7 years since we started our journey in the Netherlands together? It's been wonderful to see you develop from struggling with Statistical Mechanics homework to becoming accomplished physicists. Above all, I treasure our friendship and I hope to go out for many more dinners together. **Mario**, thank you for being a great housemate, for all the late-night discussions, and for protecting our democracy. **Liceunation, Manel, Tomás, and Rodrigo**, getting to see you all is one of the things I always look forward to whenever I'm back home. I'm thankful that, no matter how far our paths diverge, we always manage to make them intersect again. **Anthony**, your endless curiosity and drive to understand things deeply are contagious. Thank you for all the discussions, joint book readings, the voice notes with a lofi background, and, above all, your unwavering friendship. I'm so happy that you are coming to see the defense. **Genya**, I still find it funny that we went from deskmates to housemates on the other side of the world. It was a joy to have you around! Thank you for all the lovely moments we shared, for introducing me to Fawkes, and for all the delicious food. I hope I get to visit you in Berlin very soon. **Michael**, thank you for teaching me about superconducting qubits and becoming a wonderful friend along the way. Hosting you in Brussels was so much fun!

To my parents and **Eva**, I cannot begin to list all the ways in which I'm grateful to you. Thank you for always being there. I owe you everything.

CURRICULUM VITÆ

André Alexandre DE ALMEIDA NASCIMENTO E MELO

10-05-1994	Born in Castelo Branco, Portugal.

EDUCATION

2012–2015	B.Sc. in Engineering Physics Instituto Superior Técnico, University of Lisbon, Lisbon, Portugal
2015–2017	M.Sc. in Applied Physics (cum laude) Delft University of Technology, Delft, Netherlands *Thesis:* Numerical study of a superconducting qubit for the realization of quantum Ising chains using matrix product state techniques *Promotor:* Prof. dr. Jos Thijssen
2018–2021	PhD in Condensed Matter Physics Delft University of Technology, Delft, Netherlands *Thesis:* Majorana bound states in topological Josephson junctions *Promotor:* Dr. Anton R. Akhmerov *Copromotor:* Dr. Michael T. Wimmer

WORK EXPERIENCE

2020–2021	Quantum Research Intern IBM Quantum, Yorktown Heights, New York, United States of America
2017–2018	Quantum Engineer Rigetti Computing, Berkeley, California, United States of America

LIST OF PUBLICATIONS

1. **André Melo**, Nathan Earnest-Noble, Francesco Tacchino, *Pulse-efficient quantum machine learning* , arXiv:2211.01383.
2. **André Melo**, Tanko Tanev, Anton R. Akhmerov, *Greedy optimization of the geometry of Majorana Josephson junctions* , arXiv:2205.05689.
3. João P. Moutinho, **André Melo**, Bruno Coutinho, István A. Kovács, Yasser Omar, *Quantum Link Prediction in Complex Networks*, arXiv:2112.04768.
4. **André Melo**, Valla Fatemi, Anton R. Akhmerov *Multiplet supercurrent in Josephson tunneling circuits* , SciPost Phys. 12, 017 (2022) .
5. **André Melo**, Chun-Xiao Liu, Piotr Rożek, Tómas Örn Rosdahl, Michael Wimmer, *Conductance asymmetries in mesoscopic superconducting devices due to finite bias* , SciPost Phys. 10, 037 (2021).
6. **André Melo**, Sebastian Rubbert, Anton R. Akhmerov, *Supercurrent-induced Majorana bound states in a planar geometry*, SciPost Phys. **7**, 039 (2019).